Chapter 3

Results and Discussion (Part I)

The outcome of this part:

1. Published in RSC Journal of Materials Chemistry B: '*Organ Targeting Drug Delivery Systems (OTDDS) of poly[(N-acryloyl glycine)-co-(N-acryloyl-L-phenylalanine methyl ester)] Copolymer Library and Effective treatment of Triple Negative Breast Cancer, 2025,**13**, 3876-3894* **'**

2. Filled an Indian Patent: '*A polymeric nanocapsule and a method of synthesis thereof*". Patent Application No.: 202511034476, April 08, 2025'

Chapter 3: Part-I

Organ Targeting Drug Delivery Systems (OTDDS) of poly[(N-acryloylglycine)-co-(N-acryloyl-L-phenylalanine methyl ester)] Copolymer Library and Effective treatment of Triple Negative Breast Cancer

3.1.1. Abstract: Organ specific drug delivery systems (OTDDS) are essential for the effective treatment of complicated diseases. Triple-negative breast cancer (TNBC) is such an aggressive cancer with high mortality and demands targeted therapeutics. This work is aimed to design a library of polymeric OTDDS with *N*-acryloyl-glycine (NAG) and *N*-acryloyl-*L*-phenylalanine methyl ester (NAPA) [p(NAG-*co*-NAPA)$_{(x:y)}$], and screened for their *in vivo* organ targeting specificity. From this library, the best p(NAG-*co*-NAPA)$_{(x:y)}$ NPs with x:y of 1:4 and size 160-210nm that target breasts with high extent relative to other organs has been optimized for the TNBC treatment. Network pharmacology study was used to revealed the responsible 14 genes for TNBC, and a combination of drugs DHA (target 6 genes) and piperine (target 8 genes) were used by optimizing a formulation and achieve maximum therapeutic efficiency against TNBC with IC_{50} 350µg/mL. The designed organ specific polymeric nanoparticles (NPs) library, finding target genes and proteins responsible for TNBC, and optimized formulation for effective combination therapy established an effective therapeutic option for TNBC. Findings of this work further direct that the polymeric library NPs hold an exciting therapeutic potential not only for treating TNBC, however it has opened exciting treatment options for critical diseases of liver, heart, lungs and kidney.

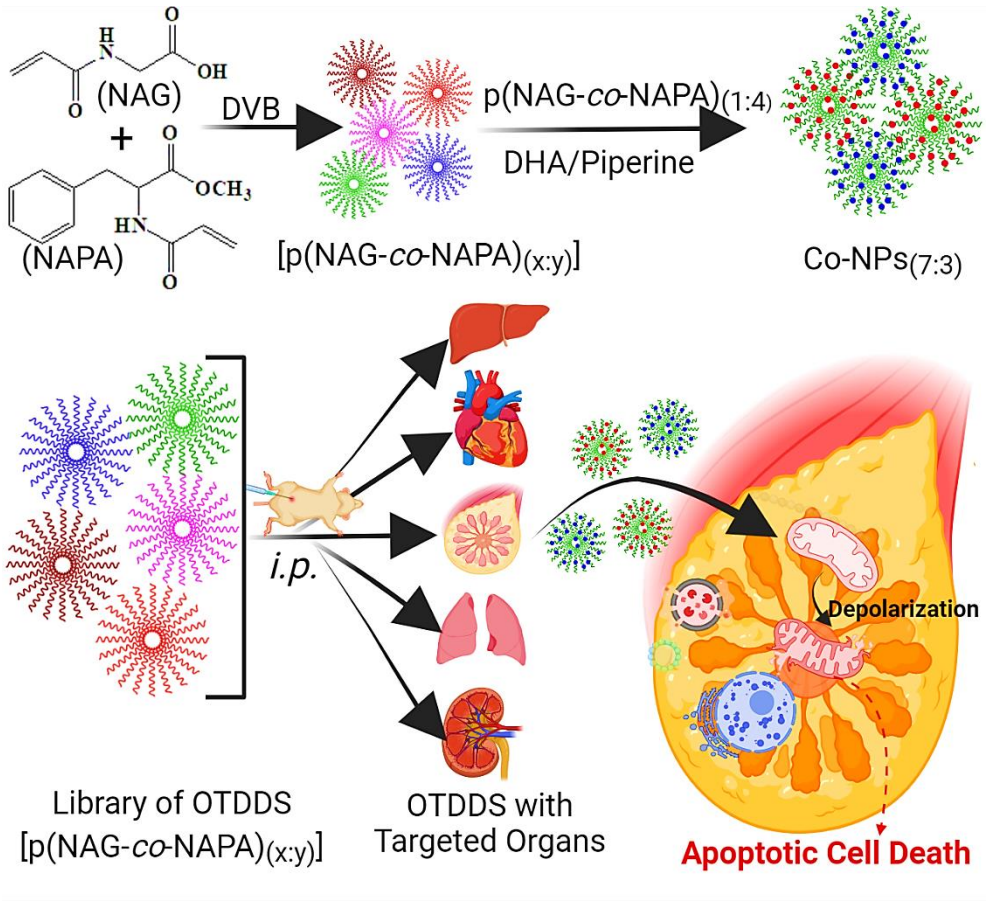

Table of content (Text): *OTDDN library of porous amphiphilic copolymer of [p(NAG-co-NAPA)$_{(x:y)}$] is effective with drug combination for the target specific treatment of triple negative breast cancer (TNBC). This NPs library further has opened the exciting treatment options for the organ specific critical diseases of liver, heart, lungs and kidney. The ToC is generated with the help of BioRender software.*

3.1.2. Introduction

Precise organ-specific delivery of therapeutic biomolecules require interdisciplinary research among the scientists of chemistry and biology, engineers, and clinicians for successful outcome of the treatment, since the surface chemistry of organ is very complicated.[1] Developing an effective organ-targeted drug delivery system (OTDDS) necessitates a clear understanding of how the physical and chemical properties of OTDDS influence the biological processes at molecular, cellular and organ levels. OTDDS can deliver precise dose of drug for

desired therapeutic outcomes rather than delivering an arbitrary amount of free drug at the targeted site.[2] For effective treatment, OTDDS must overcome the hallmark challenges such as poor biodistribution and biological fates.[1] Generally, three targeting mechanisms passive, active, and endogenous are considered to engineer OTDDS.[3-5] The passive and active targeting mechanism have been widely studied till date. The endogenous targeting is emerging as a promising approach based on how the NP's chemical versatilities lead to bind with distinct plasma protein subsets of target organs, by directing NPs to the specified organs and enhancing cellular uptake.[6, 7] However, for specific cellular uptake, controlled chemical modification of the NPs is necessary. For instance, 7C1, an oligomer derived from lipidated PEI600, was used for gene silencing in lung epithelial cells compared to kidney and heart endothelial cells. However, standardization in the lipidation process is necessary for improved silencing across different organs.[8, 9] IDD-3, a terpolymer formulated with lipid components, enables lung-selective mRNA delivery. Interestingly, compounds sharing the same polymerization degree as IDD-3 failed to target the lungs while the amino-alcohol building block was altered.[10] Furthermore, PEI modified with Vitamin A was reported with enhanced retinol binding protein 4 in the protein corona and targets hepatic stellate cells for liver fibrosis treatment.[11] Similarly, phospholipidation of cationic polymers can facilitate mRNA delivery to the spleen and lymph nodes.[12] Identifying NPs that can target inaccessible tissues such as muscles, heart, central nervous system, and gastrointestinal tract is challenging.[1] Although the chemical modification can enhance the target specificity of the delivery vehicles, however they can increase the toxicity and side effects in the long run. These insights have motivated us to synthesize copolymer NPs with varying ratio (x:y) of the biologically safe monomers (amino acid based) without using any endogenous or exogenous ligands for enhanced organ-specificity.

Several OTDDS have been approved by FDA for clinical uses including viral vectors, molecular conjugates, antibody-drug conjugates, and chemically modified polymer NPs.

Among these, polymer NPs are particularly more useful due to their ability to load various drugs separately or in combination with minimal immunogenicity, enhanced capacity of endosomal escape,[12] cell and tissue tropism[10] and easily modulated their properties through controlled chemical synthesis.[1] Amphiphilic copolymer-based nanocarriers are gaining attention for hydrophobic drug delivery in cancer treatment because of their synthetic versatility, favourable size, biocompatibility, and stability.[13-15] Compared to free drugs, nano-scaled polymeric carriers could enhance its accumulation in solid tumor cells via the enhanced permeability and retention (EPR) effect.[16] Furthermore, OTDDS can improve the drug delivery to metastatic cancer cells and potentially bypass permeability barriers. However, despite the development of numerous polymeric nanovehicles for targeted or receptor-mediated (exogenous ligands) drug delivery,[17] achieving the expected anticancer efficacy remains a challenge due to off-target effects.[18] The key feature of the polymeric OTDDS is organ-targeted delivery that could be engineered through varying the ratios of the selected monomers, which is the main focus of this work. By varying the x:y ratio, a library of copolymer NPs i.e.; organ targeted drug delivery nanoparticle (OTDDN) could be generated and subsequently the selection of a particular OTDDN could be president for the treatment of invasive cancer such as triple-negative breast cancer (TNBC).

Considering different organ based diseases, TNBC is the most prevalent malignancy and the leading cause of cancer-related mortality (lifetime is 18 months from detection) among women worldwide, accounting 15-20% of breast cancer cases.[19-21] It has the worst prognosis regarding tumor relapse and patient survival, making it a clinically aggressive cancer with limited therapeutic options.[22, 23] This highlights the urgent need for developing combinatorial therapies for TNBC using a suitable copolymer based drug delivery system OTDDN to eliminate the chemoresistance issues.[24-26] To address this, a combination delivery of DHA and piperine could be used for better efficacy. Dihydroartemisinin (DHA), a

hydrophobic metabolite of artemisinin, shows significant potential in treating TNBC.[27, 28] and piperine, a hydrophobic alkaloid from black pepper (Piper nigrum), has demonstrated anticancer effects.[29-31] Thus treatment with combining of DHA with piperine could be an effective strategy for TNBC through targeted drug delivery systems (TDDS) from the designed copolymeric NPs library. This option potentially can delay the TNBC adaptation while minimizing severe side effects associated with the free drug combinations.[32-39] Development of biocompatible acrylate-amino acid-based polymers by the authors of the present work are also reported elsewhere for various therapeutic applications.[14, 40-44] Authors have reported that poly(*N*-acryloyl-*L*-phenylalanine methyl ester) [p(NAPA)] NPs exhibit adjuvant properties on the innate immune system[14] and porous poly(*N*-acryloyl-glycine) [p(NAG)] NPs serve as an excellent drug delivery carrier with enhanced anti-inflammatory effects.[40, 43] Presently, authors' idea of designing a library of copolymers based OTDDN without depending on organ targeting mechanisms could further be a game changer option for the treatment of TNBC.

In the above line, this work reports on OTDDN library of porous amphiphilic copolymer NPs, specifically [p(NAG-*co*-NAPA)$_{(x:y)}$], using *N*-acryloyl glycine and *N*-acryloyl-*L*-phenylalanine methyl ester as monomers in varying molar ratios (x:y) have been synthesized. Physicochemical properties have been studied to confirm the structural and chemical functionality of OTDDNs and further evaluate their efficiency to target different organs. The targeting efficiency of these copolymer NPs are assessed based on in vivo organ-based biodistribution studies. The [p(NAG-*co*-NAPA)$_{(1:4)}$] NPs demonstrated a maximum targeting efficiency to the breast tissue, that facilitated the loading of DHA and piperine individually or in combination, and exhibited pH-based drug release behavior. *In silico* studies, including network pharmacology and molecular docking have been performed to predict gene targets for TNBC. Additionally, in vitro IC_{50} values of nanoformulations (NFs) on MDA-MB-231 cell

lines is analyzed to assess TNBC inhibition efficiency and mechanisms through quantitative estimation of the reactive oxygen species (ROS), mitochondrial membrane potential assay, cell cycle arrest, and apoptosis via flow cytometry. Finally, a future direction has been made for the uses of various OTDDNs in library which could be effective for a number of organ targeted therapies.

3.1.3. Experimental

3.1.3.1. Materials

The chemicals and cell lines used for this work has been listed in Chapter 2 (Page No. 52-52, Section 2.2).

3.1.3.2. Synthesis and Characterization of NAG, NAPA, p(NAG), p(NAPA), and library of OTDDNs

3.1.3.2.1. Synthesis and characterization of NAG and NAPA monomers

The synthesis procedure of NAG and NAPA monomers and their characterization details are given in the Methodologies section of Chapter 2 (Page No. 53-55, Section 2.3.1.1. and 2.3.1.2.).

3.1.3.2.2. Synthesis of p(NAG), p(NAPA) and p(NAG-*co*-NAPA)$_{(x:y)}$ NPs

The detailed synthesis procedure of homopolymers and library of OTDDS p(NAG-*co*-NAPA)$_{(x:y)}$ NPs is described in the Methodologies section of Chapter 2 (Page No. 55, Section 2.3.1.3.). The different ratios of monomers used in this library NPs are mentioned in below attached **Table 3.1.1**.

Table 3.1.1. Homopolymers and library of OTDDS [p(NAG-*co*-NAPA)$_{(x:y)}$] with different monomer ratios.

Polymer code	Composition	Monomer's ratio (x:y)
p(NAG)	NAG	NA
p(NAPA)	NAPA	NA
P1	p(NAG-*co*-NAPA)	1:1
P2	p(NAG-*co*-NAPA)	1:2
P3	p(NAG-*co*-NAPA)	1:3
P4	p(NAG-*co*-NAPA)	1:4
P5	p(NAG-*co*-NAPA)	1:5

3.1.3.2.3. Physicochemical Characterizations of p(NAG), p(NAPA), and [p(NAG-*co*-NAPA)$_{(x:y)}$] NPs

The characterization details, colloidal stability and morphology study details are described in the Methodologies section of Chapter 2 (Page No. 57-59, Section 2.3.2. and 2.3.3.).

3.1.3.3. Cell viability study of p(NAG), p(NAPA), and library of OTDDNs [p(NAG-*co*-NAPA)$_{(x:y)}$] NPs

A detailed procedure for the cell viability study of homopolymers and OTDDN NPs is described in the Methodologies section of Chapter 2 (Page No. 67, Section 2.3.7.1.). This study is performed using one healthy cell (L929) and two cancer cell lines such as A549 and MDA-MB-231 with a concentration range of 1 to 500 μg/mL and 7.8125 to 1000 μg/mL.

3.1.3.4. Hemocompatibility of p(NAG), p(NAPA), and library of OTDDNs [p(NAG-*co*-NAPA)$_{(x:y)}$ NPs

A detailed procedure for the hemocompatibility study of homopolymers and OTDDN NPs is described in the Methodologies section of Chapter 2 (Page No. 68, Section 2.3.7.3). The selected concentration range for this study is 7.8125 to 500 μg/mL.

3.1.3.5. *In vivo* biodistribution of p(NAG), p(NAPA), and library of OTDDNs [p(NAG-*co*-NAPA)$_{(x:y)}$] NPs

The procedure for the *in vivo* biodistribution study of homopolymers and OTDDN NPs is described in the Methodologies section of Chapter 2 (Page No. 74-75, Section 2.3.9.2).

3.1.3.6. Biodegradation of p(NAG-*co*-NAPA)$_{(1:4)}$ (P4) NPs

A detailed procedure for the biodegradation study of P4 NPs is described in the Methodologies section of Chapter 2 (Page No. 59 and Section 2.3.4). The biodegradation study only for P4 NPs was conducted since P4 NPs was finally used for the TNBC treatment.

3.1.3.7. Network Pharmacology and Molecular docking assessment for finding targets of DHA and piperine

3.1.3.7.1. Network Pharmacology

A detailed procedure for the *in silico* network pharmacology study of DHA and Piperine against TNBC is described in the Methodologies section of Chapter 2 (Page No. 59-60, Section 2.3.5.1.).

3.1.3.7.2. Molecular Docking assessment

The complete *in silico* molecular docking procedure of DHA and Piperine with selected genes related to TNBC is described in the Methodologies section of Chapter 2 (Page No. 60, Section 2.3.5.2).

3.1.3.8. Preparation of DHA or Piperine loaded p(NAG-*co*-NAPA)$_{(1:4)}$ NPs (DP4 and PP4)

The preparation method of DP4 and PP4 NFs, i.e., the loading of DHA and Piperine in p(NAG-*co*-NAPA)$_{(1:4)}$ NPs is briefly described in the Methodologies section of the Chapter 2 (Page No. 65-66, Section 2.3.6.1.).

3.1.3.9. *In vitro* drug release study of DP4 and PP4 NFs

The procedure followed for the in vitro drug release study from PP4 and DP4 NFs is briefly described in the Methodologies section of the Chapter 2 (Page No. 66, Section 2.3.6.2.).

3.1.3.10. Evaluation of IC_{50} and combination index (CI) for DP4, PP4 and DP4:PP4 (Co-NPs)

The complete procedure for the evaluation of IC_{50} values for developed NFs is described in the Methodologies section of the Chapter 2 (Page No. 67-68, Section 2.3.7.2.).

3.1.3.11. *In vitro* inhibition of MDA-MB-231 cells migration

The complete procedure for the *in vitro* inhibition of MDA-MB-231 cell migration study is described in the Methodologies section of Chapter 2 (Page No. 68, Section 2.3.7.4.). For this experiment P4, DP4, PP4 and Co-NPs were used at a concentration of 350μg/mL.

3.1.3.12. Apoptosis study by Annexin-V/ Propidium iodide

The complete procedure for the apoptosis study in MDA-MB-231 cell is described in the Methodologies section of Chapter 2 (Page No. 69, Section 2.3.7.6.). For this experiment P4, DP4, PP4 and Co-NPs were used at a fixed concentration of 350 μg/mL.

3.1.3.13. Cell cycle analysis

The complete procedure for the cell cycle analysis in MDA-MB-231 cell is described in the Methodologies section of Chapter 2 (Page No. 69, Section 2.3.7.5.). For this experiment P4, DP4, PP4 and Co-NPs were used at a fixed concentration of 350 μg/mL.

3.1.3.14. Quantification of intracellular ROS generation and mitochondrial membrane potential (MMP)

The complete procedure for the quantification of intracellular ROS generation and mitochondrial membrane potential (MMP) in MDA-MB-231 cell is described in the Methodologies section of Chapter 2 (Page No. 69-70, Section 2.3.7.7.). For this experiment P4, DP4, PP4 and Co-NPs were used at a fixed concentration of 350 μg/mL.

3.1.3.15. Animal ethical approval

All information regarding animal ethical approval is given in the Methodologies section of Chapter 2 (Page No. 74, Section 2.3.9.1.).

3.1.3.16. Statistical Significance

Statistics applied on this work is described in the Methodologies section of Chapter 2 (Page No. 78, Section 2.4.).

3.1.4. Results and Discussion

3.1.4.1. Synthesis and Physicochemical characterization of monomers, homopolymers and library of OTDDNs

To develop a library of OTDDNs of amino acid based amphiphilic copolymers, *N*-acryloyl glycine (NAG) and *N*-acryloyl-*L*-phenylalanine methyl ester (NAPA) monomers were used.

The monomers were synthesized (yield 60-65%) and confirmed through ^{1}H (**Figure S3.1.2(a)** and **S3.1.3(a)**), ^{13}C NMR **Figure S3.1.2(b)** and **S3.1.3(b)**) and FTIR (**Figure S3.1.4**). The monomer synthesis process was followed as Schotten-Baumann reaction reaction approach, where amine group of monomers reacts with acryloyl chloride in the basic medium to form an amide bond. In the final stage of washing or extraction, ethyl acetate was used as an organic phase to improve the yield percentage of monomers. Further, free radical mini-emulsion

polymerization method (**Figure S3.1.1**) was used to synthesize a library of [p(NAG-*co*-NAPA)$_{(x:y)}$] copolymers. The p(NAG) and p(NAPA) homopolymers were synthesized and used as reference. Here, hexadecane (HD) was used as a co-stabilizer of the droplets formed during the emulsion process, which prevents the quiescent and grain growth. Initially, monomers were dispersed in the oil phase (toluene) and formed monomer droplets. AIBN, a radical initiator was used to initiate the polymerization reaction at ~70-75°C. The oily core surrounded by a thin polymeric membrane was stabilized by crosslinking the monomer droplets with DVB which helps to generate pores and provide mechanical strength to the NPs. To generate a library of copolymers, the NAG to NAPA wt% ratio were varied (**Table 3.1.1**) and a series of reactions were performed. Additionally, SDS was used as a surfactant to avoid the aggregation during the emulsion process. AIBN initiates the polymerization process by interacting with the terminal sp^2 hybridized carbon of NAPA, NAG, and DVB, and form the radicals. This leads to chain propagation and crosslinking, resulting in the amphiphilic copolymer [p(NAG-*co*-NAPA)$_{(x:y)}$] NPs. The carboxylic acid groups of NAG monomer form a hydrophilic shell while phenyl rings create a hydrophobic core, and potentially allowing to form dense-core NPs with pores.

The chemical functionalities of [p(NAG-*co*-NAPA)$_{(x:y)}$] NPs were confirmed through ^{1}H NMR, ^{13}C NMR, FTIR, and UV-Vis spectroscopic analysis. It can be clearly noted that, for simplicity and better understanding, the data points mentioned in this section are particularly

for P1 copolymer which was already published in another report. All other copolymers present in library (P2-P5) are quite similar to the P1 with variation in considerable range and spectra are shown in their respective images for reference. The number of protons with probable position are determined using ^{1}H NMR spectroscopy (**Figure 3.1.1(a)**). The distinct bands identified for p(NAG) and p(NAPA) for ^{13}C NMR are given in supplementary (**Figure S3.1.4**). As mentioned in author's earlier works, δ (^{1}H NMR) for P1 copolymer are as follows: 8.32 (1H, d, secondary amine of glycine monomer), 8.21 (1H, d, secondary amine of phenylalanine monomer), 7.16 (5H, m, aromatic protons), 4.34 (3H, t, alkoxide), 6.41 (-C(=O) N) cis, 5.62 (-C(=O) N) trans, 3.94-2.37 (1H, m, -CH_2 adjacent to amide of glycine monomer), 3.25-2.36 (1H, m, -CH_2 adjacent to amide of phenylalanine monomer), and 2.52 (1H, dd, J= 11.3, 9.5). In ^{13}C NMR, δ corresponding to monomers are disappeared and a single band in the range of 40.27 to 39.18 is appeared, indicating the presence of a splitting of 2° alkanes (**Figure S3.1.4**). Further, for FTIR spectra, the distinct bands observed for p(NAG) and p(NAPA) homopolymers are shown in **Figure 3.1.1(b)** and coincide well with the library of copolymers (**Figure 3.1.1(b)**). The major characteristic bands present in copolymers are (ν in cm^{-1}): 3413 (secondary -NH, s), 1739 (ester C=O, s) and 1659 (-NH-C=O, s) etc. Similarly, UV-Vis spectra of copolymers confirms the formation of p(NAG-*co*-NAPA) NPs by showing two distinct bands at 213nm and 265nm corresponding to π-π* transition and phenyl rings (**Figure 3.1.1(c)**). Furthermore, based on the XRD results (**Figure 3.1.1(d)**), it is clearly noticed that OTDDNs are amorphous in nature. Comparing to homopolymers, copolymers exhibited higher thermal stability (**Figure 3.1.1(e)**). P1 to P5 NPs showed three steps of degradation, where the first step is observed due to the loss of surface moisture followed by polymer chain degradation (**Figure 3.1.1(e)**). From DSC (exo up and endo down), it is revealed that other than homopolymers, all five copolymers are showing phase transition at ~70-75°C with an endothermic peak (**Figure 3.1.1(f)**). MALDI-ToF spectra for all the samples are recorded

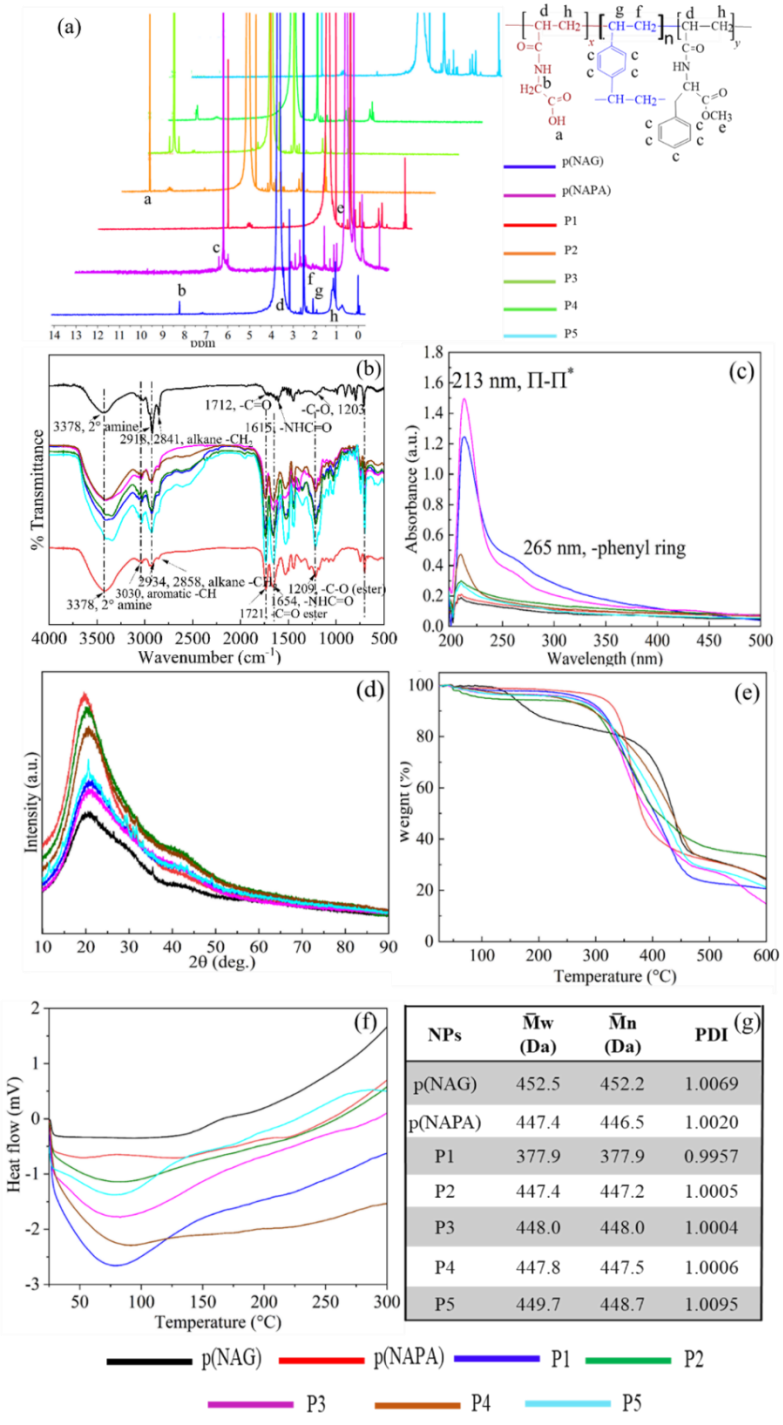

NPs	M̄w (Da)	M̄n (Da)	PDI
p(NAG)	452.5	452.2	1.0069
p(NAPA)	447.4	446.5	1.0020
P1	377.9	377.9	0.9957
P2	447.4	447.2	1.0005
P3	448.0	448.0	1.0004
P4	447.8	447.5	1.0006
P5	449.7	448.7	1.0095

(g)

Figure 3.1.1. *Physicochemical properties of library NPs (P1 to P5) with p(NAG) and p(NAPA) as references. Fig. (a) Stack plots of 1H NMR spectra, (b) stacked FTIR spectra of copolymers (dashed lines are representing the overlapped peaks in between reference NPs and copolymers), (c) UV-Vis spectra, (d) XRD, (e) TGA, (f) DSC and (g) MALDI-ToF (weight average molecular weight (M̄w), number average molecular weight (M̄n), and polydispersity indexes (PDI) are summarized for copolymer NPs (P1-P5), respectively.*

weight of two monomers always kept fixed (500mg). Overall, the chemical functionality and (**Figure S3.1.6-S3.1.12**) and tabulated in **Figure 3.1.1(g)**. Results clearly showed the presence of heterogeneous fragments for copolymers which is an indication of formation of random copolymers. The linearity in the PDI index represents the uniformity of the chains. It has been observed that with increase in the monomer ratio, there is change in $\bar{M}_w$ and $\bar{M}_n$, however PDI for all calculated NPs to be ~1.0 (**table** in **Figure 3.1.1**). It is obtained may be due to the overall MALDI-ToF studies confirmed the successful formation of library NPs [p(NAG-*co*-NAPA)$_{(x:y)}$]. All the library NPs are checked for different organ target specificity and shown in the subsequent section.

The morphology and colloidal stability of the library of NPs were studied through HR-TEM, DLS, Zeta and CD spectroscopy. The HR-TEM images of p(NAG) and p(NAPA) NPs are shown in **Figure S3.1.13** with their respective SAED patterns. HRTEM image of p(NAG) suggested the formation of porous NPs with a size of ~130-190nm (**Figure S3.1.13(a1)** and (**a2)**), while p(NAPA) NPs are showing dense core with porous shell with c.a. ~100-120nm (**Figure S3.1.13(b1)** and **(b2)**). In series, it can be observed that from P1 to P5 a smooth change in porous spherical structure with change in size is observed (**Figure 3.1.2 (a1-e3)**). For P1, the particles of size ~130nm are agglomerated (**Figure 3.1.2(a1-a3)**), while for P2-P4, the particles are monodispersed in nature and mimicking the structure of p(NAPA) NPs as through the series NAPA concentration have been increased (**Figure 3.1.2(b1-d3)**). Whereas in case of P5, the spherical co-connected NPs more likely to a chain type of structure has been observed (**Figure 3.1.2(e1-e3)**). This chain-like structure formed as the concentration of NAPA increased, i.e., with higher content of phenyl rings, it tends to form a linearly arranged structure with less steric hindrance. Further, hydrodynamic size and ζ of the NPs have been studied and shown in **Figure 3.1.2(f)**. It is clearly noticed that with increase in NAPA concentration, hydrodynamic size and obtained ζ have been increased. The higher hydrodynamic size of

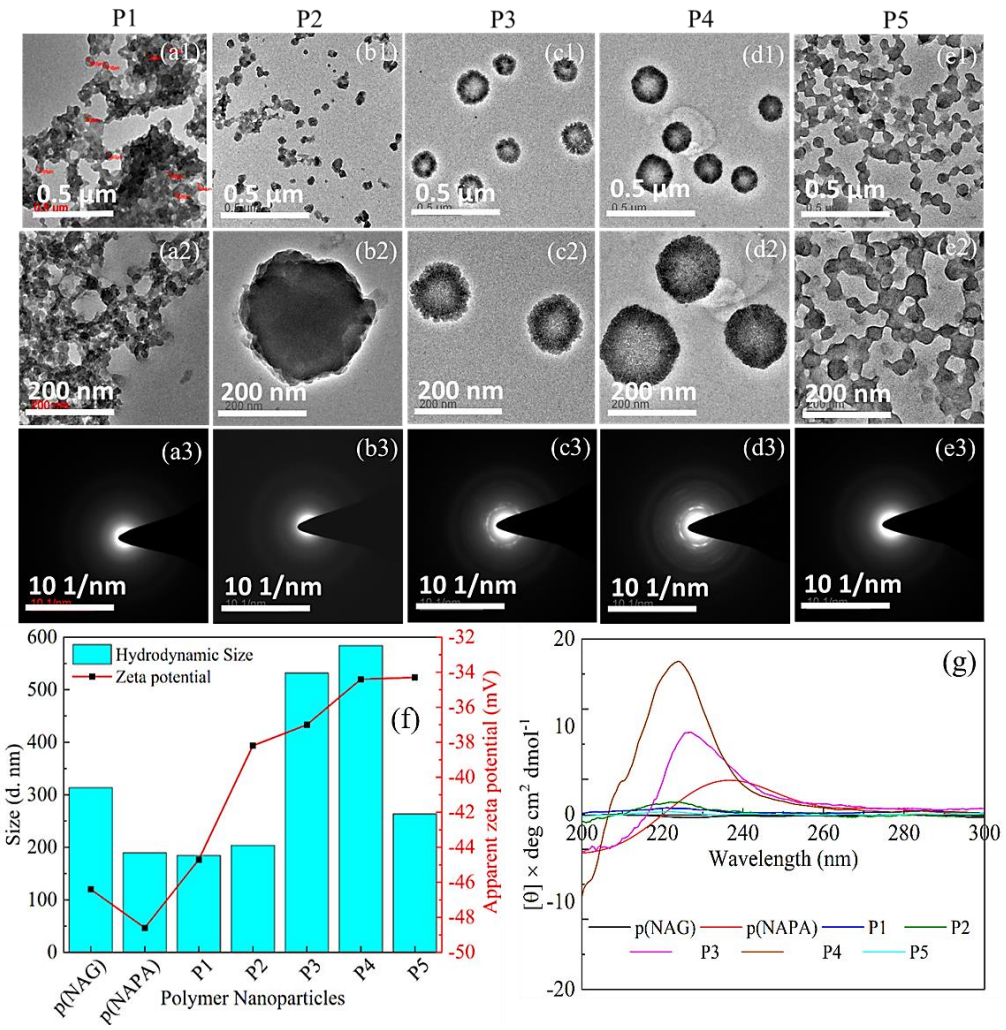

Figure 3.1.2. *Morphology and colloidal stability studies of copolymer NPs. Fig. (a1-a3), (b1-b3), (c1-c3), (d1-d3) and (e1-e3) HR-TEM images of P1-P5 NPs at 0.5 µm and 200 nm magnification with their SAED patterns, respectively, (f) DLS and Zeta potential, and (g) CD spectra of P1-P5 NPs with p(NAG) and p(NAPA) as references, measured with 250 µg/mL concentration in MilliQ at 25°C.*

p(NAG) is due to the spongy porous structure of NPs as observed from HRTEM (**Figure S3.1.13(a1)** and **(a2)**). Furthermore, CD spectroscopy is performed to study the chiral and optical properties of the NPs. It is noticed that due to the presence of phenyl ring in the copolymer system, for P1-P4, the intensity of the CD band has been increased and sifted towards left. This shifting can be attributed due to the increase in the number of phenyl rings in the system.[45] In case of P5, no 2° arrangement has been observed. The absence of folding in P5 due to the formation of chains at that ratio rather than dispersed NPs (**Figure 3.1.2(e1-e2)**).

The corresponding α-helix, β-sheet, turns and random coil % are provided in supplementary (**Table S3.1.2**). These porous structures, spherical shaped morphology, and negative zeta potential with chiro-optical properties of the OTDDNs offered valuable insights for the designing of specific drug or vaccine, with more stability and shelf-life in biological medium.

3.1.4.2. Biocompatibility, hemocompatibility and biodistribution of library OTDDNs

For therapeutic applications of the OTDDNs, they should be biocompatible, hemocompatible and target specific in nature. At first the cell viability of designed OTDDNs were checked against L929, i.e., mouse fibroblast cells. **Figure S3.1.14(a)** and **(d)** and **Figure 3.1.3(a-d)** represent the cell viability results of p(NAG), p(NAPA), P1 NPs and P2-P5 NPs, respectively for the concentrations 1 to 500μg/mL against L929. It is observed that for p(NAG) NPs the cell viability is ~100% at 500μg/mL, while at lower concentration starting from 50 to 1μg/mL cell viability % varies from 110% to 101%. Whereas, for p(NAPA) NPs, cell viability decreased from 74% (100μg/mL) to 69% (500μg/mL). For P1 NPs, at higher concentration cell viability is observed to be 78% and 89% for 500 μg/mL and 250 μg/mL respectively. Whereas, for 100 to 25μg/mL cell viability varies from114 to 102%. The cell viability % observed for P2 is ~85 to 75% from the lower to higher concentrations. Whereas for P4, the viability achieved better with respect to P3 and P5 for all the concentrations range used here. For P5, at 500μg/mL it exhibited toxicity (viability ~60%) due to the higher content of NAPA monomer. Furthermore, the cytotoxicity of the OTDDNs have been tested against two cancer cell lines such as A549 and MDA-MB-231 (**Figure S3.1.14(b, c and e)** and **Figure 3.1.3(e-h)** varying concentrations from 7.8125 to 1000μg/mL. The p(NAG) NPs was incubated with both the cancer cells and the viability observed to be from 100 % to 80 % from lower to higher concentration, respectively (**Figure S3.1.14(b)** and **(c)**). For p(NAPA), the cell viability % against A549 is obtained to be ~ 100 % for all concentrations, whereas MDA-MB-231

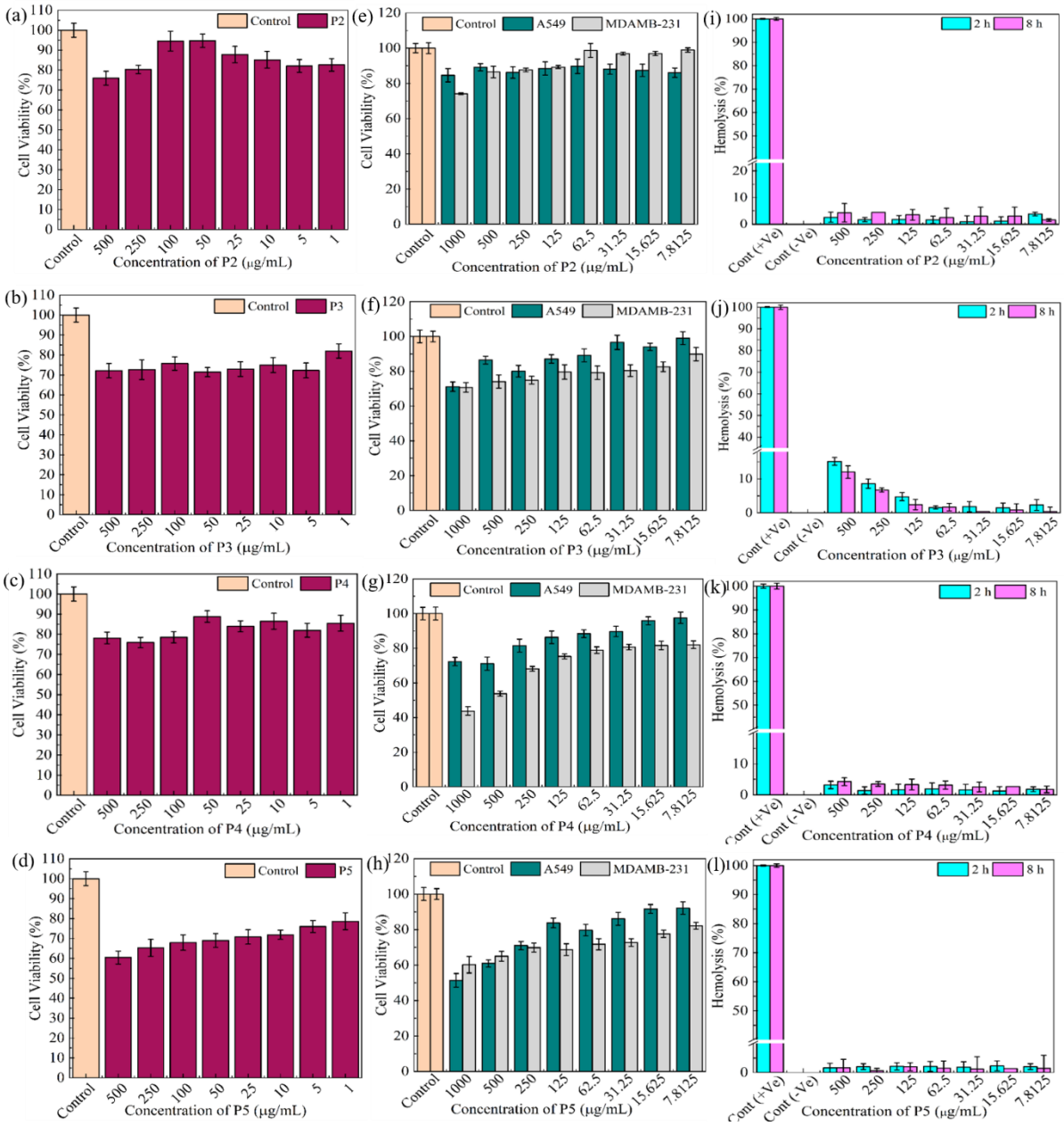

Figure 3.1.3. *Cytocompatibility and hemocompatibility of OTDDNs. Fig. (a-d) Cytocompatibility against L929, (e-h) A549 and MDA-MB-231 cell lines and (i-l) hemocompatibility of P2, P3, P4 and P5 NPs, respectively at different concentrations. For all the figures3.1.3(a-l) statistical significance values are provided in supplementary (**Table S3.1.3.-S3.1.6**).*

exhibited ~80% viability at 1000µg/mL. Further, P1 NPs were also incubated with A549 and MDA-MB-231 cell lines and cell viability % were observed to be 85 % and 67 % for 1000µg/mL, respectively. Considering P2 to P5, other than P2 in all three OTDDNs, a similar trend of cell viability % i.e.; with increase in concentration the smooth decrease in cell viability

% have been observed. For P2, all tested concentrations, cell viability against A549 is obtained to be ~ 90%, while against MDA-MB-231, at lower concentration it exhibited ~ 100% viability. Among P3, P4 and P5, P4 is showing the lowest % cell viability at 1000 μg/mL (~45%). Thus, it can be concluded that all the NPs in the library are quite toxic against MDA-MB-231 cells with respect to A549.

Hemocompatibilty evaluation for biomaterials is crucial for any therapeutic purposes as they enter systemic circulation and can cause harmful effects by limiting therapeutic benefits. A material considered to be an effective biomaterial if its hemolysis value is below 5%. Therefore, hemolytic activity of all the samples were studied in both dose and time dependent manner over a range of 7.8125 to 500 μg/mL (**Figure 3.1.3(i-l)**). A varied degree of hemolysis % is observed for selected concentrations at 2h and 8h. It is seen that for p(NAG), p(NAPA) and P1, hemolysis % is below 5% upto 8h (**Figure S3.1.15**). For P3, at higher concentrations (500 and 250μg/mL) the hemolysis % obtained to be 15% and 8%, respectively, whereas for all other samples the hemolysis results obtained to be in the considerable range. The images of the hemolytic tubes are attached in supplementary (**Figure S3.1.15**). Therefore, OTDDNs are suitable Therefore, OTDDNs are suitable biomaterials and can be used for different therapeutic uses. To find out the organ selectivity of OTDDNs, *in vivo* biodistribution studies have been conducted following the process as mentioned in the experimental section (**Figure 3.1.4(a)**). Five major organs (Lungs, Heart, Liver, Kidney, and Breast) are considered to quantify the target efficiency of OTDDNs by measuring the fluorescence intensity and are compared with the control p(NAG) and p(NAPA) NPs. From *in vivo* biodistribution study, a diversified properties of library NPs are observed. From the intensity, it is obvious that the p(NAG), P3, and P5 are target specific to the lungs (**Figure 3.1.4.(b)**). Control sample p(NAG) is targeting to the lungs and heart, whereas p(NAPA) is targeted to the heart and liver. P1 is target specific

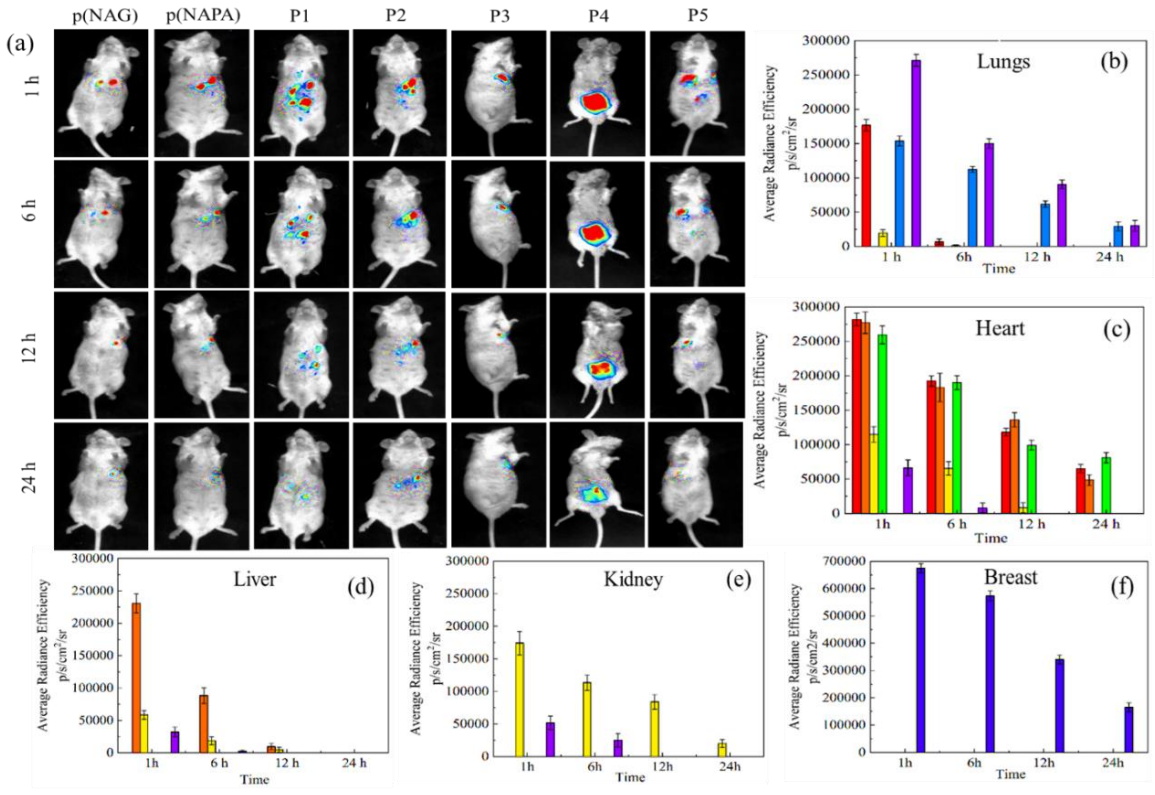

OTDDNs	Lungs	Heart	Kidney	Liver	Breast
p(NAG)	+	+	-	-	-
p(NAPA)	-	+	-	+	-
P1	-	+	+	+	-
P2	-	+	-	-	-
P3	+	-	-	-	-
P4	-	-	-	-	++
P5	+	+	+	+	-

Figure 3.1.4. *In vivo biodistribution of OTDDNs. (a) IVIS imaging of NPs at 1, 6, 12 and 24 h, (b-e) average radiance at concerned time period in different body organs such as Lungs, Heart, Liver, Kidney and Breast, respectively and (g) table with indications of organ specificity ('+': targeted, '+++': highly target specific and '-': non targeted).*

to the heart, kidney and liver efficiently. P2 is only target specific to the heart. P3 is preferably targeting to the lungs. Interestingly, it is exciting to report that P4 is very much target specific to the breast (700000p/s/cm^2 /sr^1). However, P5 is target specific to the lungs, heart, liver and kidney. The detailed target specificity has been mentioned in **Table** (**Figure 3.1.4(g)**). Therefore, the obtained results of cell viability, hemolysis and *in vivo* biodistribution are clear

evidence that P4 could be a suitable OTDDS for the targeted delivery of drugs for the treatment of TNBC. Further to use the P4 NPs for TNBC treatment, the biodegradation study was performed in simulated body fluid (SBF) (pH 7.4) as discussed in the method section. The morphology of the degraded P4 NPs was scrutinized through the HRTEM after 7 days of post-incubation with SBF (**Figure S3.1.16**). Results exhibited that P4 NPs (of size 180 to 200nm) were degraded into small fragments (10 to 20nm) as shown in the supporting HRTEM images (**Figure S3.1.16(a1)** and **(b1)**). Therefore, it can be concluded that the P4 NPs are degradable.

3.1.4.3. *In silico* assessment of DHA and Piperine as targeted drugs for TNBC

The *in silico* assessment on selected anticancer drugs, i.e.; DHA and piperine, is conducted using network pharmacology and molecular docking which can predict gene targets and binding affinity of selected ligands with them respectively. The results exhibited that both the drugs are effective as anticancer agents. SwissTarget prediction tool was used to determine the targeted enzymes of TNBC (seven for piperine and two for DHA). These enzymes were run through DisGeNet and targeted proteins were listed and further analysed as a PPI network using Cytoscape. A network of common genes and target compounds with enzymes is constructed (**Figure 3.1.5(a-b)**. Additionally, more gene targets were found from GEPIA2 and used to construct a Venn diagram (**Figure 3.1.5(c)**), which represents that 860 genes are responsible for TNBC. Piperine and DHA can target 94 and 92 genes, respectively. Out of 860 genes responsible for TNBC, piperine and DHA can target 6 and 8 genes, respectively. However, no such common genes of TNBC have been reported which could be targeted by both piperine and DHA. Further, more gene targets were collected from NCBI and recent literature on TNBC[46-49] and screened top 40 genes with highest connectivity. A network-like structure has been constructed with different colour gradients which represents the degree of relatedness of genes with TNBC (**Figure 3.1.5(d)**). The identified genes were further

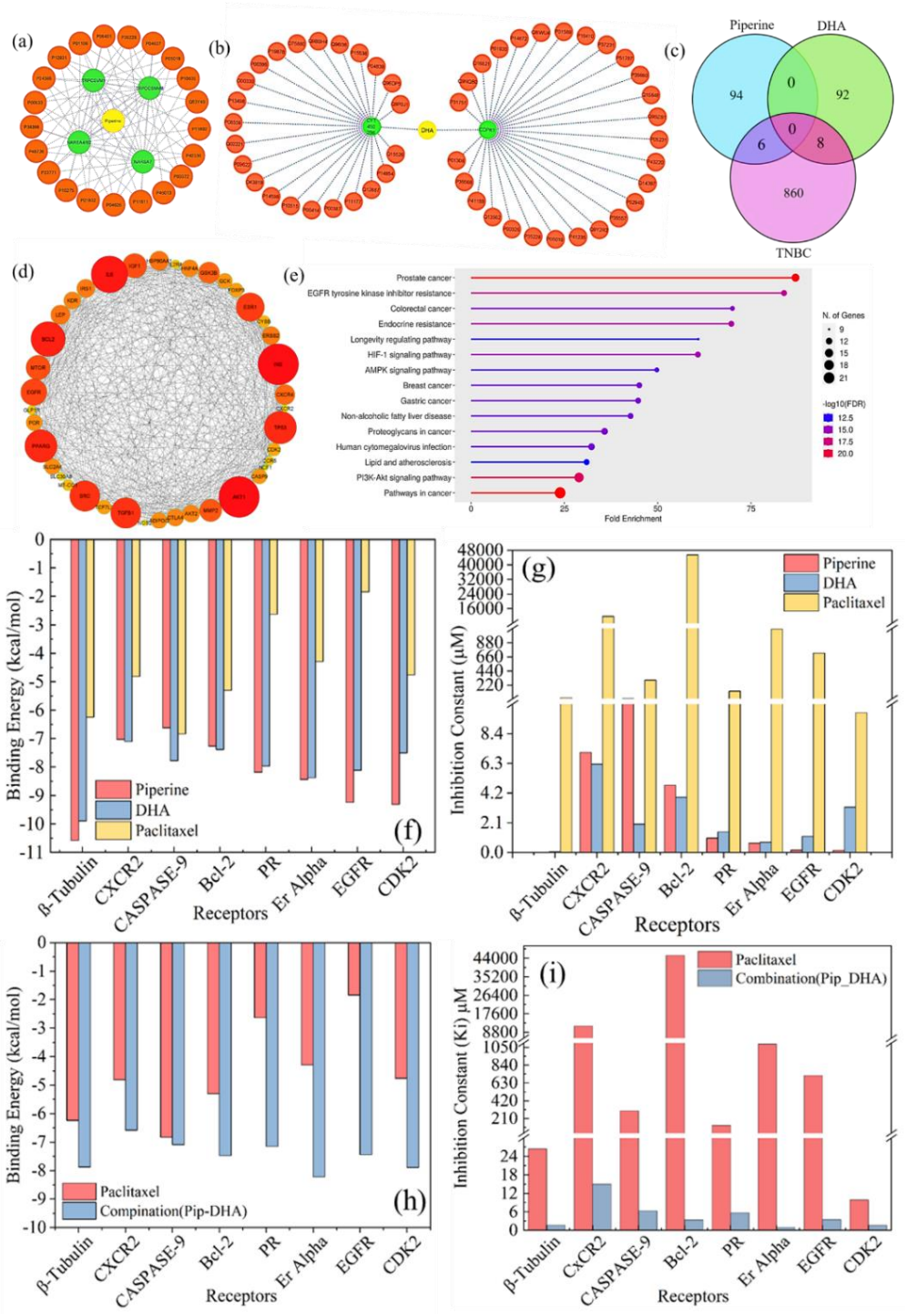

Figure 3.1.5. *Network pharmacology and molecular docking results of piperine and DHA against TNBC. Fig. (a) and (b) show target protein network for piperine and DHA, respectively, (c) Venn diagram shows the common gene targets by piperine and DHA responsible for TNBC, (d) Interrelated network map of top 40 genes target of piperine and DHA and (e) gene expression responsible for TNBC pathways, (f) binding energy, and (g) Ki for target proteins of piperine and DHA. (g) Binding energy, and (i) Ki for the combination of piperine and DHA with paclitaxel. The colors in Figure 3.1.5.(e) shows the p-values for each term, with lower p-values having darker colours. The dot size demonstrates the number of genes associated with each pathway.*

explored to understand their pathways relatedness to the targeted genes responsible for TNBC (**Figure 3.1.5(e)**). A lollipop plot has been drawn to represent the top 15 pathways. It is clearly observed that, among various other cancers, breast cancer GO enrichment is ~50 folds, these targeted genes can be highly expressed in breast cancer following various pathways. From network pharmacology study, 24 receptor proteins responsible for TNBC have been selected for molecular docking with paclitaxel as an FDA approved anti-TNBC drug. Then single docking has been performed for 24 receptor proteins with piperine and DHA separately. Their obtained binding energy, inhibition constant (K_i) values and amino acid residues are listed in **Table S3.1.7**. It is clearly evident that piperine and DHA are interacting differently with different amino acid residues. Further, out of these 24 proteins, seven proteins (CXCR2, Caspase 9, BCL-2, PR, ER α, EGFR and CDK2) dominantly responsible for TNBC as per the highest negative binding energy with lowest Ki are selected. Their binding energy and inhibition constant values are compared with paclitaxel (**Figure 3.1.5(f)** and **(g)**). Here β-tubulin is also considered as a potential target, as paclitaxel inhibits the growth of TNBC by binding with β-subunit of tubulin.[50-52] **Figure 3.1.5(f)** and **(g)**, reveal that comparing to paclitaxel, both piperine and DHA are showing more binding affinity with less K_i. Since, one of the important objectives of this work is to find out the synergistic anti-TNBC effects of piperine and DHA, the combination docking has been performed to find out the binding pockets with selected 8 receptor proteins in two steps, (i) piperine followed by DHA and (ii) DHA followed by piperine. The binding energy and K_i values are shown in **Figure 3.1.5(c)** and **(d)**. The docking scores are shown in **Table S3.1.8** and **S3.1.9**, which clearly show that for combination study, the binding energy is highly negative, and K_i is very low with respect to paclitaxel. Therefore, a combination of piperine and DHA can be used for TNBC treatment with better efficacy. The detailed binding energy, K_i values and amino acid residues are enlisted in **Table (S3.1.8 and S3.1.9)** for β-tubulin, CXCR2, Caspase 9, BCL-2, PR, ER α, EGFR and

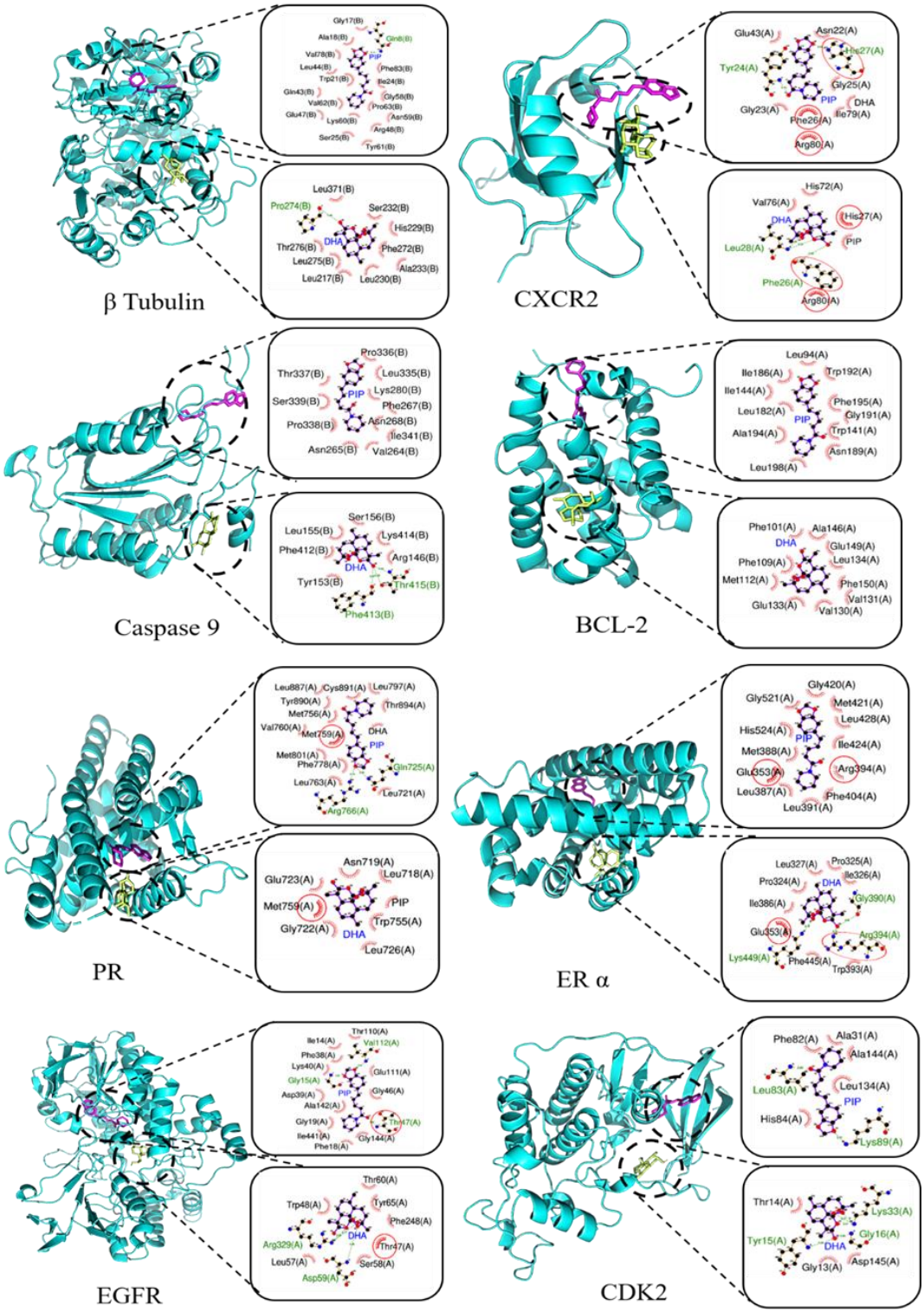

Figure 3.1.6. *Sequential Docking for 3D complex structure of β tubulin, CXCR2, Caspase 9, BCL-2, PR, ER α, EGFR, CDK2, with piperine and DHA in combination. In ligplots, green colour lines represent the H-bonds between ligands and amino acid residues and red circles represent the common polar and nonpolar hydrophobic interactions between the ligands.*

CDK2. Further, their 3D structures and corresponding 2D lig plots have been extracted (**Figure 3.1.6**) as mentioned in the method section, which clearly represents both polar (H-bonds) and nonpolar interactions with specific amino acid residues. From the figures and tables, it is clearly visible that piperine and DHA are showing H-bonds at Gln98 and Pro274 for β-tubulin, at Try24, His27 and Leu28, Phe26 for CXCR2 whereas for caspase 9, DHA is forming only H-bonds at Phe413 and Thr415. For piperine, PR is showing H-bonds with Arg766 and Gln725 residues. In case of ER α, DHA is forming strong H-bonding with three amino acid residues (Lys449, Gly390 and Arg394). For EGFR, piperine is establishing three polar interactions

(Val112, Gly15 and Thr47) and DHA is showing two polar interactions (Arg329 and Asp59) with amino acid residues. Similarly, in CDK2, the DHA is forming three hydrogen bonds (Lys33, Try15 and Gly16), whereas it is limited to two polar interactions for piperine (Leu83 and Lys89). The presence of these common interacting amino acid residues suggests that piperine and DHA can inhibit TNBC more efficiently by targeting these 4 proteins (CXCR2, PR, ER α and EGFR) out of the selected 8 proteins. The network pharmacology and molecular docking results further revealed that, a number of protein targets are existing for piperine and DHA to inhibit TNBC and among them the major potential targets can be selected for *in vitro* and *in vivo* TNBC studies.

3.1.4.4. Preparation, characterization, *in vitro* cytotoxicity and migratory effect of piperine or DHA loaded P4 NPs (PP4 and DP4)

P4 has been selected to load piperine or DHA for targeting TNBC as per the method discussed in the experimental section. The amphiphilic nature of copolymers enhances the loading of hydrophobic piperine and DHA in the core and shell of the P4 NPs. Piperine and DHA are loaded separately in P4 NPs and designated as PP4 and DP4, respectively. The LE% and EE% have been calculated for both the drugs (**Table 3.1.2.**) and it is observed that the

encapsulation efficiencies are very good for both piperine (48.60%) and DHA (93.85%). Due to the difference in phobicity, different extent of loading is observed. It can be noted that the increased EE% in DHA is high due to the more hydrophobic complex ring structure with respect to piperine.

The thermal stability of all the samples have been studied from 25°C to 600°C and observed that they are quite stable upto 50°C. Minor weight loss (2-3%) upto 100°C is observed due to the surface moisture. Beyond 160°C the weight loss of the polymer particle occurred due to the breaking of the polymer bonds. After loading drugs, PP4 and DP4 show more thermal stability as compared to P4 (**Figure S3.1.17**). This increase in stability of drug loaded polymer NPs is due to the strong drug-polymer interaction, improved structural packing, and barrier to water diffusion by hydrophobic drugs. The *in vitro* drug release behavior of PP4 and DP4 have been studied by dialysis bag approach in 1×PBS buffer (pH 7.4) acidic medium (pH 6.8) upto

Table 3.1.2. Physicochemical properties of P4, PP4 and DP4.

Nanoparticles	Size (d. nm)	Zeta Potential (mV)	PDI	EE%	LE%
P4	538.8	-34.40	0.730	-	-
PP4	429.7	-31.36	0.722	48.60	32.69
DP4	492.6	-37.50	0.736	93.85	48.09

30 days and the results have been shown in **Figure 3.1.7(a)**. It is observed that in case of neutral medium, ~5% and ~15% release have been observed at 24 h for PP4 and DP4, respectively. It is clearly observed that the release occurs stepwise as stimuli responsive in nature[53] for all the samples in all pH. However, it is interesting to mentioned that DP4 at pH 6.8 releases DHA very fast with respect to the other samples. It can also be mentioned that upto 30days DP4 release maximum ~40% DHA as in this case pH is acting as a stimuli and there is a possibility

of breaking of network of copolymer chains periodically which influence for the stepwise release of piperine/DHA.[53] In contrast, PP4 at pH 6.8 as well as DP4 at both pH 7.4 and 6.8 exhibit comparably higher and similar rates of cumulative release since the acidic pH (6.8), may increase ionization, promote swelling, or partially destabilize the PP4 matrix, thereby facilitating faster drug release. To assess the effects of NFs against TNBC, MTT assay was performed (**Figure 3.1.7(b-d)**) with varying the doses of PP4 and DP4 from 25 to 2500µg/mL. From **Figure 3.1.7(b-d)**, it is clearly evident that the effective treatment of TNBC is dose dependent. The IC_{50} values for PP4 and DP4 have been calculated and the results obtained to

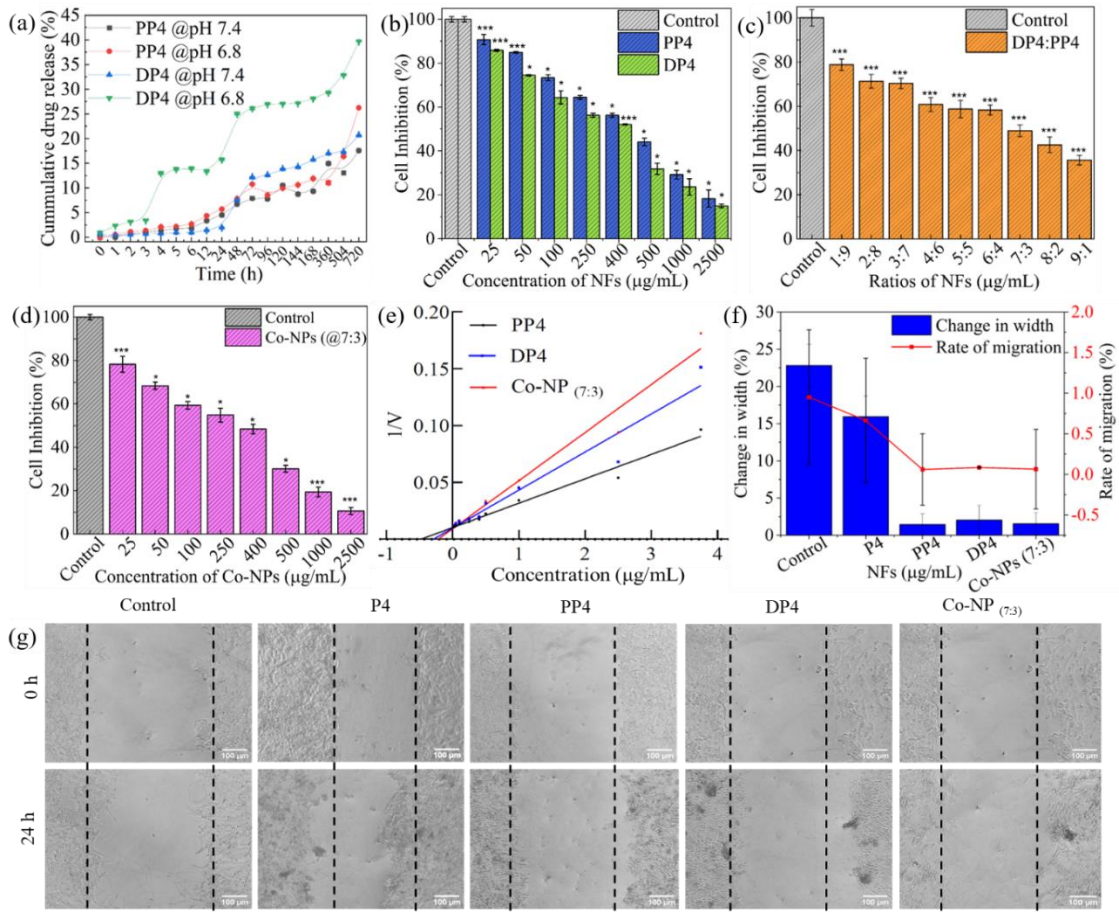

Figure 3.1.7. *In vitro cytotoxycity and migratory effect of NFs in MDA-MB-231 cells. Fig. (a) in vitro drug release % of NFs at different pH, (b-d) in vitro treatment efficiency of NFs studied against TNBC (MDA-MB-231) with different concentrations, (e) Dixon plot shows the 1/V vs concentration: for calculating enzymatic inhibition constant (Ki), (f) represent the change in width (%) and rate of migration (%) calculated from the microscopic images and (g) by Fiji imageJ software, and (g) microscopic images of wound scratch assay (scale: 100µm).*

be 450µg/mL and 409.5µg/mL, respectively. Interestingly, with varying the ratio of DP4:PP4 for combination therapy, a synergetic TNBC inhibition is observed (**Figure 3.1.7(c)** and **S3.1.18**). For combination therapy (DP4+PP4), the IC_{50} obtained for 7:3 ratio (**Figure 3.1.7(c)**) is promising. Further, different concentrations of mixed DP4:PP4 at 7:3 were taken to study the TNBC inhibition and the IC_{50} is found to be 350µg/mL. However, from this study it can be concluded that for each and every ratio of composition, different IC_{50} values are obtained. By selecting the IC_{50}, based on the severity of the patient dose dependent treatment for TNBC can be programmed. Furthermore, IC_{50} values for PP4 and DP4 were used to calculate CI (eqn. 3.1.5) and it is observed that the CI value is less than '1', which implies the synergetic inhibition effect of DHA and piperine against TNBC. K_i values for each NFs were determined by using Dixon plot[54] (**Figure 3.1.7(e)**), the K_i values are obtained by extrapolating the cytotoxicity results and found to be 0.941µg/mL, 0.571µg/mL and 0.45µg/mL for PP4, DP4 and Co-$NPs_{(7:3)}$, respectively. Thus the order of effectiveness of the designed NFs is as follows: Co-$NPs_{(7:3)}$ > DP4> PP4. All the designed NFs are showing competitive inhibition which is matching well with the earlier mentioned docking results.

To effectively prevent metastasis caused by tumor cells, it is crucial to study the behavior of MDA-MB-231 cells migration in the presence of designed NFs. *In vitro* wound scratch assay is performed to study the proliferation and migratory properties of cells in presence of P4, PP4, DP4 and Co-$NPs_{(7:3)}$ for 24 h (**Figure 3.1.7(f)**). The change in width (%) results reaveled that, as compared to control (22.82%), for P4 NPs (15.94%) a minor change is observed. Whereas, compared to P4 or control with NFs (for PP4, DP4 and Co-NPs), the change in width (%) values are below 5% which is very negligible (**Figure 3.1.7(f)**). Similarly, from the rate of cell migration results, it is found that although for rate of migration for control and P4 are 0.95% and 0.66%, respectively, however for PP4, DP4 and Co-$NPs_{(7:3)}$ the values obtained are 0.06%, 0.08% and 0.06%, respectively (**Figure 3.1.7(f)**). The rate of migration by NFs has decreased

by 90 % of the control. Thus, by considering the above results, further studies have been conducted with 350μg/mL for all the NFs including P4 NPs as control.

3.1.4.5. Effect of PP4, DP4, and Co-NPs(7:3) on programmed cell death, cell cycle and TNBC inhibition mechanism

The IC_{50} values obtained from the MTT assays for individual and Co-$NPs_{(7:3)}$ for MDA-MB-231 cells, however to confirm whether NFs are inducing apoptotic or necrotic pathway, flow cytometric assays have been performed (**Figure 3.1.8(a)**). Herein, Annexin-V/PI were used to deduce the various stages of apoptosis.[55] P4, PP4 and DP4 along with Co-$NPs_{(7:3)}$ are treated with MDA-MB-231 cells at 350μg/mL and their cell death pathway has been studied. As earlier it has been observed that, P4 is inducing cytotoxicity to the cells (**Figure 3.1.3(g)**). In flow cytometry, results revealed that P4 is inducing necrotic cell death (51.26%). Comparing PP4 and DP4, PP4 is inducing more necrotic cell death (extent of live cell: 13.68%, late apoptotic: 1.14% and necrotic cell: 85.12%). Whereas, DP4 is promoting late apoptotic cell death (live cell: 41.63%, late apoptotic: 28.48% and necrotic cells: 29.24%) which further justify the considered target ratio of DP4:PP4, i.e., 7:3 for TNBC treatment. The use of DHA has surged the late apoptotic stage from 1.14% to 28.48%, which is highly remarkable. Furthermore, Co-$NPs_{(7:3)}$ demonstrates a decrease in the necrotic cells (9.21%), significant increase in live cells (56.44%), early apoptotic (13.31%), and slight decrease in the late apoptotic cells (21.04%). This study further revealed that, instead of P4, PP4 and DP4, Co-$NPs_{(7:3)}$ can be potentially used as a TNBC target as it is showing a programmed cell death (apoptosis) at IC_{50} concentration (350μg/mL).

One of the key steps in developing potential anticancer NF is controlling the cell cycle.[56] Based on the cell cycle study (**Figure 3.1.8(b)**), the developed NFs possessed potential to initiate apoptosis in MDA-MB-231 cells. In case of P4, the activation of G0-G1 phase (65.72%) is the reason for reduction in cell viability %. Whereas, in case of PP4 and DP4, the G0-G1

phase percentage is quite similar in range, however drastic differences are observed for S and G2-M phases, e.g., the S phase decreases from 20.80% to 13.52%, while G2-M phase increases from 11.73% to 22.74%. That means, the G2-M phase is dominating for DP4 and the value becomes almost doubled as compared to the PP4. For Co-NPs$_{(7:3),}$ the extent of S phase is decreased, whereas the G2-M phase is increased as compared to the P4, PP4 and DP4 NPs. It can be stated that Co-NPs$_{(7:3)}$ is inhibiting the cell growth by arresting the cell cycle at G2-M phase. Subsequently, the TNBC inhibition mechanism has been established by quantifying the reactive oxygen species (ROS) and mitochondrial membrane potential (MMP) (**Figure 3.1.8(c)**and **(d)**). ROSs are strong oxidants, that can trigger the cells by increasing the intracellular reactive oxygen species and further cause DNA, protein or lipid degradation and diminish their activities. Here, DCFDA is a green fluorescent dye used to quantify the ROS generated by treatment conditions. The fluorescent intensity is directly proportional to the amount of ROS present in the sample. Similarly, apoptosis is related to change in mitochondrial membrane potential and mitochondrial damage. The mitochondrial potential is the determinant for cell death. Rhodamine-123 (Rh-123) was used to estimate MMP. It enters into the mitochondria when the membrane potential is intact. However, when the mitochondria lose their potential, the excess Rh-123 leaks out, resulting in a detectable reduction in fluorescence. This decrease in fluorescence is directly related to the loss of mitochondrial potential. In case of ROS, although all NFs including Co-NPs$_{(7:3)}$ exhibit ROS based cell inhibition more as compared to the control, however the inhibition efficiency follows as: DP4>P4>PP4> Co-NPs$_{(7:3)}$. This trend is based on nanoparticle and nanoformulation composition and structure, surface chemistry, charge, drug release behaviour, cellular uptake efficiency, and the resulting amount of ROS generated. DP4 increases ROS production inside TNBC cells by improving

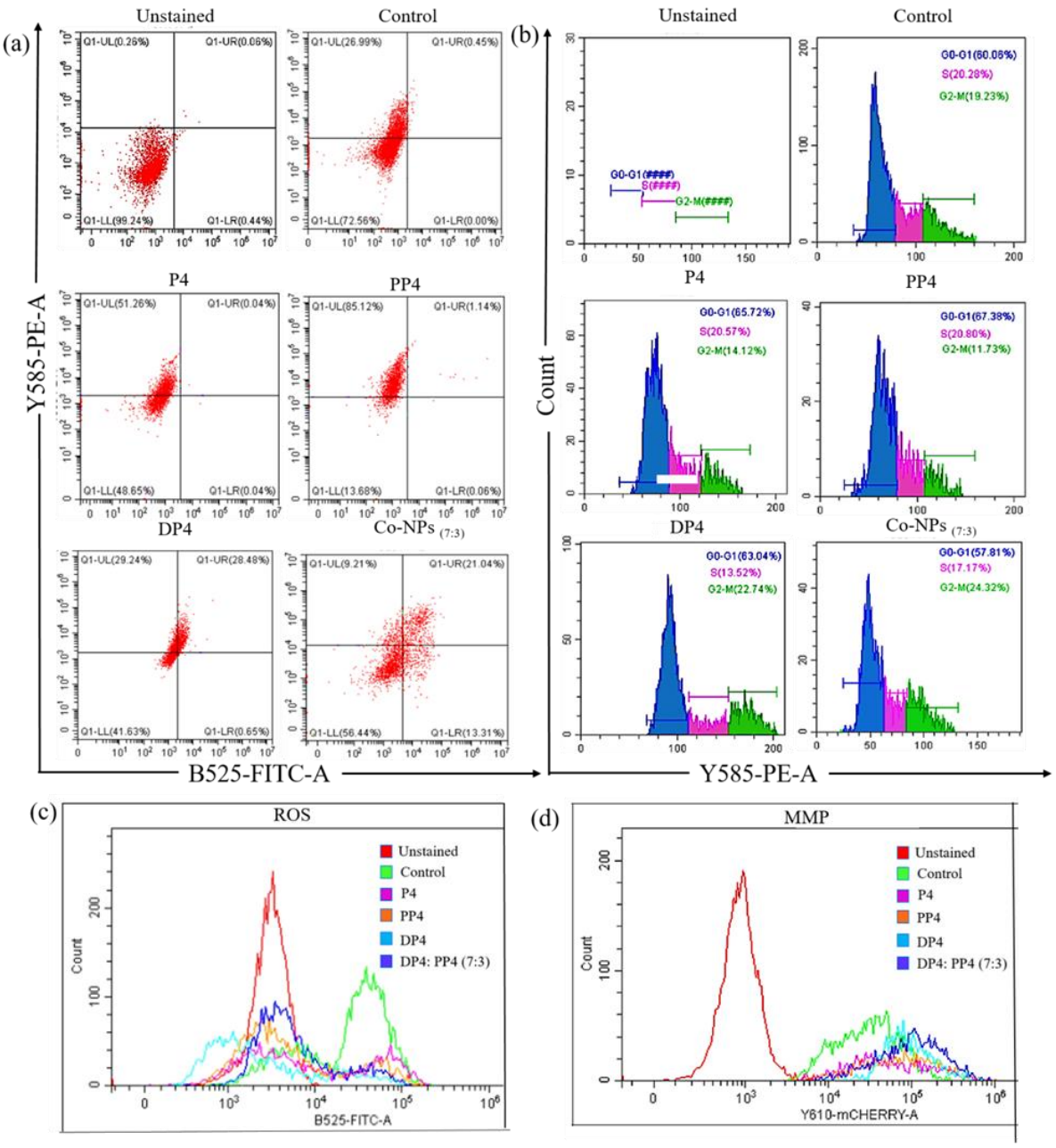

Figure 3.1.8. *Flow cytometry study of the NPs and Co-NPs$_{(7:3)}$. Fig. (a) Annexin V/ PI flow cytometry study, (b) cell cycle analysis, (c) ROS quantification and (d) mitochondrial membrane potential study of P4, PP4, DP4 and Co-NPs$_{(7:3)}$ at 350µg/mL with unstained (only cells) and control (only dye).*

cellular uptake, release kinetics, and/or surface chemistry, whereas P4 produces moderate amount of ROS, resulting in less cell inhibition than DP4 but more than PP4. As the release percentage (%) is further lower for PP4 compared to DP4, and PP4 generates less ROS, providing less TNBC inhibition. In the case of Co-NFs, the synergistic mechanism works in

such a way that it results in even lower ROS generation, which is evident from the shifting of fluorescence spectrum towards the right on the plot. For Co-NPs$_{(7:3)}$ the maximum fluorescent intensity value is approaching upto ~10^5 order. Further, in between ROS and MMP, MMP is dominated more over the ROS as compared to the control, P4, PP4, and DP4 that shifted more towards the right side of the fluorescence intensity plot with a range of 106 order (**Figure 3.1.8(c)**). Further, Co-NPs(7:3) is shifted more showing a broad spectrum with increase in the cell count, which depicts that the cell killing mechanism occurred by Co-NPs(7:3) is majorly due to the change in membrane potential of the TNBC (**Figure 3.1.8(d)**). Therefore, it can be stated that Co-NPs(7:3) is exhibiting late apoptotic cell death by inducing MMP based TNBC killing. Therefore, all the above results corroborate that Co-NPs(7:3) could be a potential agent for the treatment of TNBC. It can also be noted that all the combinations of PP4 and DP4 can be used as per the severity of cancer.

3.1.5. Summary and Conclusions for this part

The current challenges in targeted therapy are that, none of the reported nanocapsules are hundred percent target specific, rather most of the cases existing drug delivery devices missed the target and led to the side effects. In this light, the present work focused on constructing a library of organ targeted amino acid based amphiphilic copolymer i.e., p(NAG-*co*-NAPA)$_{(x:y)}$ for therapy. The physicochemical characterization of the synthesized p(NAG-*co*-NAPA)$_{(x:y)}$ NPs are conducted to ensure the synthesis and subsequently screened for their potential to act as a drug delivery vehicle to the different organs. *In vivo* organ based biodistribution is studied to reveal the best OTDDNs targeting breast, i.e., p(NAG-*co*-NAPA)$_{(1:4)}$ NPs (P4). In addition to this, *in silico* study is also performed to justify the selection of piperine and DHA, since they target 14 genes that are responsible for TNBC. The prepared piperine (PP4) and DHA (DP4) loaded NFs possess excellent drug loading and pH dependent drug release that enhanced the targeted delivery in TNBC site by minimizing the systemic side effects. The low IC_{50} values in

combination treatment, i.e. with Co-NPs$_{(7:3)}$ revealed the synergetic treatment efficiency of TNBC rather than antagonism behaviour. The flow cytometry results revealed that the inhibition of TNBC by Co-NPs$_{(7:3)}$ formulation is accomplished due to the mitochondrial membrane potential mediated apoptosis by arresting the G2-M phase in the cell cycle. It can be noted that block-co-polymers with varying mers have different extent of target efficiency to the various organs, which has never been reported. This finding resemble that based on the treatment of interest, any of the library nanocapsules can be selected for the optimum delivery of drugs as well as to achieve maximum therapeutic efficiency, which may not be restricted to the major organs such as liver, heart, lungs or kidney, rather it can be used to treat the other organs too. It further can be noted that the used polymeric NPs subsequently can be degraded and can go out from the body. However, to comprehend the efficacies of the NFs and to progress towards future clinical trials, *in vivo* studies have been taken under consideration and the results will be reported as a continuation of this work.

3.1.6. References

1. Dilliard, S.A. and D.J. Siegwart, *Passive, active and endogenous organ-targeted lipid and polymer nanoparticles for delivery of genetic drugs.* Nature Reviews Materials, 2023. **8**(4): p. 282-300.
2. Bertrand, N. and J.-C. Leroux, *The journey of a drug-carrier in the body: An anatomo-physiological perspective.* Journal of Controlled Release, 2012. **161**(2): p. 152-163.
3. Sun, W., et al., *Leveraging Physiology for Precision Drug Delivery.* Physiological Reviews, 2017. **97**(1): p. 189-225.
4. Li, J. and K. Kataoka, *Chemo-physical Strategies to Advance the in Vivo Functionality of Targeted Nanomedicine: The Next Generation.* Journal of the American Chemical Society, 2021. **143**(2): p. 538-559.
5. Dilliard, S.A., Q. Cheng, and D.J. Siegwart, *On the mechanism of tissue-specific mRNA delivery by selective organ targeting nanoparticles.* Proceedings of the National Academy of Sciences, 2021. **118**(52): p. e2109256118.
6. Behzadi, S., et al., *Cellular uptake of nanoparticles: journey inside the cell.* Chemical Society Reviews, 2017. **46**(14): p. 4218-4244.
7. Peng, S., et al., *Enhanced cellular uptake and tumor penetration of nanoparticles by imprinting the "hidden" part of membrane receptors for targeted drug delivery.* Chemical Communications, 2017. **53**(81): p. 11114-11117.

8. Xue, W., et al., *Small RNA combination therapy for lung cancer.* Proceedings of the National Academy of Sciences, 2014. **111**(34): p. E3553-E3561.
9. Khan, O.F., et al., *Endothelial siRNA delivery in nonhuman primates using ionizable low–molecular weight polymeric nanoparticles.* Science Advances, 2018. **4**(6): p. eaar8409.
10. Kowalski, P.S., et al., *Ionizable Amino-Polyesters Synthesized via Ring Opening Polymerization of Tertiary Amino-Alcohols for Tissue Selective mRNA Delivery.* Advanced Materials, 2018. **30**(34): p. 1801151.
11. Zhang, Z., et al., *Corona-directed nucleic acid delivery into hepatic stellate cells for liver fibrosis therapy.* ACS nano, 2015. **9**(3): p. 2405-2419.
12. Liu, S., et al., *Zwitterionic Phospholipidation of Cationic Polymers Facilitates Systemic mRNA Delivery to Spleen and Lymph Nodes.* Journal of the American Chemical Society, 2021. **143**(50): p. 21321-21330.
13. Pandey, B., et al., *Amphiphilic Glycopolypeptide Star Copolymer-Based Cross-Linked Nanocarriers for Targeted and Dual-Stimuli-Responsive Drug Delivery.* Bioconjugate Chemistry, 2019. **30**(3): p. 633-646.
14. Yamala, A.K., et al., *Poly-N-acryloyl-(l-phenylalanine methyl ester) hollow core nanocapsules facilitate sustained delivery of immunomodulatory drugs and exhibit adjuvant properties.* Nanoscale, 2017. **9**(37): p. 14006-14014.
15. Kim, S., et al., *Overcoming the barriers in micellar drug delivery: loading efficiency, in vivo stability, and micelle–cell interaction.* Expert Opinion on Drug Delivery, 2010. **7**(1): p. 49-62.
16. Peer, D., et al., *Nanocarriers as an emerging platform for cancer therapy.* Nature Nanotechnology, 2007. **2**(12): p. 751-760.
17. Choi, H.Y. and J.-E. Chang, *Targeted Therapy for Cancers: From Ongoing Clinical Trials to FDA-Approved Drugs.* International Journal of Molecular Sciences, 2023. **24**(17): p. 13618.
18. Salari, N., et al., *Polymer-based drug delivery systems for anticancer drugs: A systematic review.* Cancer Treatment and Research Communications, 2022. **32**: p. 100605.
19. Sedeta, E.T., B. Jobre, and B. Avezbakiyev, *Breast cancer: Global patterns of incidence, mortality, and trends*. 2023, American Society of Clinical Oncology.
20. WHO, *Breast Cancer*. 2024, World Health Organization.
21. Li, X., et al., *Triple-negative breast cancer has worse overall survival and cause-specific survival than non-triple-negative breast cancer.* Breast Cancer Research and Treatment, 2017. **161**(2): p. 279-287.
22. Mamnoon, B., et al., *Targeted Polymeric Nanoparticles for Drug Delivery to Hypoxic, Triple-Negative Breast Tumors.* ACS Applied Bio Materials, 2021. **4**(2): p. 1450-1460.
23. Tripathy, S., et al., *ROS mediated Cu[Fe(CN)5NO] nanoparticles for triple negative breast cancer: A detailed study in preclinical mouse model.* Biomaterials Advances, 2024. **160**: p. 213832.
24. Bianchini, G., et al., *Treatment landscape of triple-negative breast cancer — expanded options, evolving needs.* Nature Reviews Clinical Oncology, 2022. **19**(2): p. 91-113.
25. Zhang, L., et al., *Nanoparticles carrying paclitaxel and anti-miR-221 for breast cancer therapy triggered by ultrasound.* Cell Death Discovery, 2023. **9**(1): p. 298.
26. Londhe, S., et al., *Silver nitroprusside nanoparticles for breast cancer therapy: in vitro and in vivo approach.* Nanoscale, 2023. **15**(23): p. 10017-10032.

27. Kongpatanakul, S., et al., *Comparative study of dihydroartemisinin and artesunate safety in healthy Thai volunteers.* International journal of clinical pharmacology and therapeutics, 2009. **47**(9): p. 579-586.
28. Lu, J.-J., et al., *Dihydroartemisinin induces apoptosis in HL-60 leukemia cells dependent of iron and p38 mitogen-activated protein kinase activation but independent of reactive oxygen species.* Cancer Biology & Therapy, 2008. **7**(7): p. 1017-1023.
29. Kumar, S., et al., *Role of piperine in chemoresistance*, in *Role of nutraceuticals in cancer chemosensitization*. 2018, Elsevier. p. 259-286.
30. Abdelhamed, S., et al., *Piperine Enhances the Efficacy of TRAIL-based Therapy for Triple-negative Breast Cancer Cells.* Anticancer Research, 2014. **34**(4): p. 1893.
31. Quijia, C.R. and M. Chorilli, *Piperine for treating breast cancer: A review of molecular mechanisms, combination with anticancer drugs, and nanosystems.* Phytotherapy Research, 2022. **36**(1): p. 147-163.
32. Chen, T., et al., *Cancer-cell-membrane-camouflaged supramolecular self-assembly of antisense oligonucleotide and chemodrug for targeted combination therapy.* Nanoscale, 2023. **15**(4): p. 1914-1924.
33. Lin, L., et al., *Formation of ssDNA nanotubes from spherical micelles and their use as a delivery vehicle for chemotherapeutics and senolytics to triple negative breast cancer cells.* Nanoscale, 2023. **15**(22): p. 9801-9812.
34. Liu, Y., et al., *Amplification of oxidative stress via intracellular ROS production and antioxidant consumption by two natural drug-encapsulated nanoagents for efficient anticancer therapy.* Nanoscale Advances, 2020. **2**(9): p. 3872-3881.
35. Rajora, A.K., et al., *Emergence and impact of theranostic-nanoformulation of triple therapeutics for combination cancer therapy.* Smart Medicine, 2024. **3**(1): p. e20230035.
36. Zhou, W., et al., *Co-delivery CPT and PTX prodrug with a photo/thermo-responsive nanoplatform for triple-negative breast cancer therapy.* Smart Medicine, 2022. **1**(1): p. e20220036.
37. Gong, Y., et al., *An Injectable Epigenetic Autophagic Modulatory Hydrogel for Boosting Umbilical Cord Blood NK Cell Therapy Prevents Postsurgical Relapse of Triple-Negative Breast Cancer.* Advanced Science, 2022. **9**(23): p. 2201271.
38. Nethi, S.K., et al., *Polyanhydride Copolymer-Based Niclosamide Nanoparticles for Inhibiting Triple-Negative Breast Cancer: Metabolic Responses and Synergism with Paclitaxel.* ACS Applied Materials & Interfaces, 2024. **16**(51): p. 70362-70377.
39. Zheng, S., et al., *Dual-targeted nanoparticulate drug delivery systems for enhancing triple-negative breast cancer treatment.* Journal of Controlled Release, 2024. **371**: p. 371-385.
40. Gupta, P.S., et al., *Nitric oxide releasing novel amino acid-derived polymeric nanotherapeutic with anti-inflammatory properties for rapid wound tissue regeneration.* Nanoscale, 2024. **16**(4): p. 1770-1791.
41. Wasnik, K., et al., *Neurogenic and angiogenic poly(N-acryloylglycine)-co-(acrylamide)-co-(N-acryloyl-glutamate) hydrogel: preconditioning effect under oxidative stress and use in neuroregeneration.* Journal of Materials Chemistry B, 2024. **12**(25): p. 6221-6241.
42. Wasnik, K., et al., *Poly(N-acryloylglycine-acrylamide) Hydrogel Mimics the Cellular Microenvironment and Promotes Neurite Growth with Protection from Oxidative Stress.* ACS Applied Bio Materials, 2023. **6**(12): p. 5644-5661.

43. Gupta, P.S., et al., *In vivo potential of polymeric N-acryloyl-glycine nanoparticles with anti-inflammatory activities for wound healing.* Materials Advances, 2023. **4**(20): p. 4718-4731.
44. Yamala, A.K., et al., *P-LME polymer nanocapsules stimulate naïve macrophages and protect them from oxidative damage during controlled drug release.* Journal of Applied Polymer Science, 2020. **137**(6): p. 48363.
45. Werber, L., et al., *Isothermal Titration Calorimetry of Chiral Polymeric Nanoparticles.* Chirality, 2015. **27**(9): p. 613-618.
46. Wang, H., *Network pharmacology- and molecular docking-based approaches to unveil the pharmacological mechanisms of dihydroartemisinin against esophageal carcinoma.* Frontiers in Genetics, 2022. **13**.
47. Paarakh, P.M., et al., *In vitro cytotoxic and in silico activity of piperine isolated from Piper nigrum fruits Linn.* In Silico Pharmacology, 2015. **3**(1): p. 9.
48. El-Shehawy, A.A., et al., *Thymoquinone, piperine, and sorafenib combinations attenuate liver and breast cancers progression: epigenetic and molecular docking approaches.* BMC Complementary Medicine and Therapies, 2023. **23**(1): p. 69.
49. Dai, X., et al., *Dihydroartemisinin: A Potential Natural Anticancer Drug.* International Journal of Biological Sciences, 2021. **17**(2): p. 603-622.
50. Nawara, H.M., et al. *Paclitaxel-Based Chemotherapy Targeting Cancer Stem Cells from Mono- to Combination Therapy*. Biomedicines, 2021. **9**, DOI: 10.3390/biomedicines9050500.
51. Wattanathamsan, O., et al., *Tubulin acetylation enhances lung cancer resistance to paclitaxel-induced cell death through Mcl-1 stabilization.* Cell Death Discovery, 2021. **7**(1): p. 67.
52. Wang, X., et al., *Microtubule-targeting agents for cancer treatment: Seven binding sites and three strategies.* MedComm – Oncology, 2023. **2**(3): p. e46.
53. Zhang, P., et al., *A programmable polymer library that enables the construction of stimuli-responsive nanocarriers containing logic gates.* Nature Chemistry, 2020. **12**(4): p. 381-390.
54. Ruggeri, C., et al., *Identification and Validation of a Potent Dual Inhibitor of the P. falciparum M1 and M17 Aminopeptidases Using Virtual Screening.* PLOS ONE, 2015. **10**(9): p. e0138957.
55. Porter, A.G. and R.U. Jänicke, *Emerging roles of caspase-3 in apoptosis.* Cell Death & Differentiation, 1999. **6**(2): p. 99-104.
56. Boroumand Moghaddam, A., et al. *Eco-Friendly Formulated Zinc Oxide Nanoparticles: Induction of Cell Cycle Arrest and Apoptosis in the MCF-7 Cancer Cell Line*. Genes, 2017. **8**, DOI: 10.3390/genes8100281.

Chapter 3

Results and Discussion (Part II)

The outcome of this part:

1. To be Communicated in RSC Journal of Materials Chemistry B: '*Co-delivery of Dihydroartemisinin and Piperine by Folate decorated poly[(N-acryloyl glycine)$_1$-co-(N-acryloyl-L-phenylalanine methyl ester)$_4$] copolymer for Triple Negative Breast Cancer Treatment***'**

2. Filled an Indian Patent: '*A Polymeric Nanoformulation and a Method of Synthesis Thereof Patent Application No.: 202511082570,* August 30, 2025**'**

Chapter 3: Part-II

Co-delivery of Dihydroartemisinin and Piperine by Folate decorated poly[(N-acryloyl glycine)$_1$-co-(N-acryloyl-L-phenylalanine methyl ester)$_4$] copolymer for Triple Negative Breast Cancer Treatment

3.2.1 Abstract: Triple-negative breast cancer (TNBC), is an aggressive subtype of breast cancer characterized by heterogeneity. Its early recurrence due to lack of estrogen (ER), human epidermal growth factor-2 (HER-2), and progesterone (PR) that contributes to its invasiveness and high recurrence rate. Chemotherapy is the main adjuvant treatment option, but resistance often leads to failure. Tumor necrosis factor-related apoptosis-inducing ligand (TRAIL) based therapies show promise in inducing apoptosis in TNBC cells. This study aimed to investigate the potential effect of Dihydroartemisinin (DHA) with Piperine as an adjuvant in *in vitro* MDA-MB-231 cells for TNBC treatment. Accordingly, a folate conjugated copolymer of *N*-acryloyl glycine and *N*-acryloyl-L-phenylalanine methyl ester with a 1:4 monomer ratio, i.e., folate-p(NAG-*co*-NAPA)$_{(1:4)}$ NPs (fP4 NPs), has been developed, and encapsulated with DHA or Piperine to achieve TNBC targeting drug treatment. The physicochemical properties and morphological analysis revealed that the developed fP4 NPs are in the therapeutic range of ~90±10 nm and demonstrated an enhanced pH-dependent drug release behavior in the tumor microenvironment (acidic pH) as compared to neutral conditions. Further, *in vitro* MTT study on MDA-MB-231 resulted in a synergistic effect of drugs loaded fP4 nanoformulations (Co-NFs) with an IC_{50} of 280µg/mL. The flow cytometry results suggested that the inhibition of TNBC by Co-NFs is mainly due to the mitochondrial membrane potential mediated cell death by arresting G2-M phase. Further, gelatin zymography results demonstrated the anti-angiogenesis and non-invasion nature of nanoformulations with

decreased levels of MMP-2 and MMP-9 in extracellular matrix protein. Additionally, the RT-PCR results revealed that the Co-NF's DNA targeting capacity with anti-proliferative, anti-apoptotic, and anti-TNBC properties by downregulating DNMT3B, EGFR, Ki67, STAT3, Bcl2, and CDK2; and upregulating caspase 9, respectively. Together, these findings suggest that the designed targeted combination therapy holds future therapeutic potential for TNBC treatment.

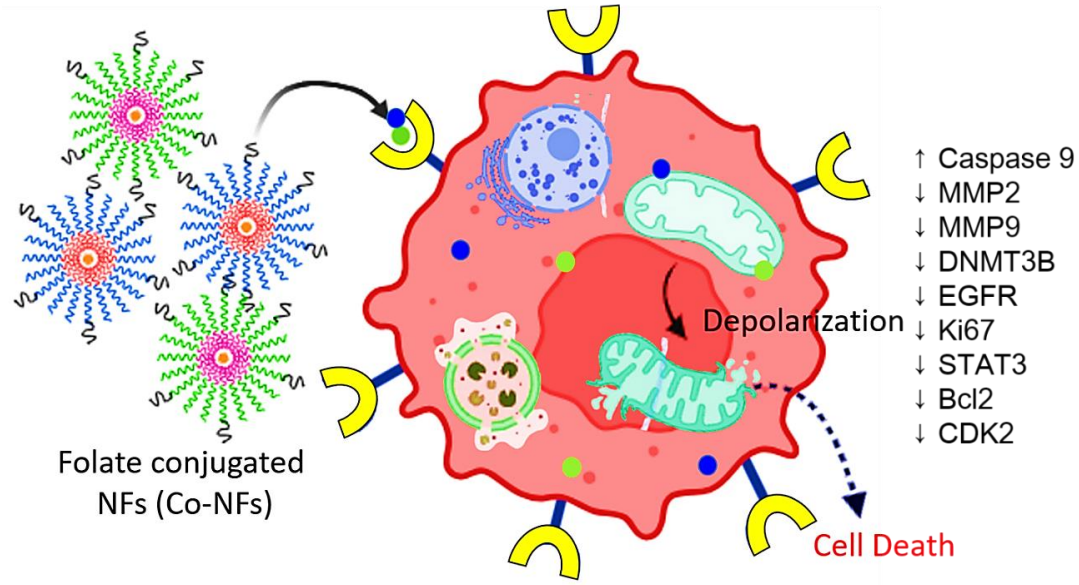

Table of Content Text: *F-p(NAG-co-NAPA)$_{(1:4)}$ NPs encapsulated with DHA or Piperine enhanced the targeting efficiency of the p(NAG-co-NAPA)$_{(1:4)}$ NPs towards TNBC. They promote cell death by mitochondrial membrane depolarization. Further, the changes in oncogenes confirms the successful inhibition TNBC through Co-NFs. The ToC is generated with the help of BioRender software.*

3.2.2 Introduction

Breast cancer is the most prevalent malignancy and the leading cause of cancer-related mortality in women globally.[1] In 2022, as per WHO, approximately 2.3 million women were diagnosed with breast cancer, leading to around 6,70,000 deaths globally. Approximately 99% breast cancer cases occur in women and 0.5–1% occur in men.[2] TNBC, accounts for 15-20% of breast cancer

cases and has the worst prognosis in terms of tumor relapse and patient survival compared to other breast cancer malignancies, making it a clinically aggressive type of cancer with no available targeted therapies.[3] Consequently, non-specific systemic chemotherapy, including anthracycline, platinum, and taxane-based regimens, remains the primary therapeutic option for TNBC patients, along with radiotherapy and immunotherapy based on the stages of TNBC.[4] However, TNBC patients face two major limitations: adverse events related to high-dose regimens and therapeutic failure due to intrinsic or de novo resistance. These circumstances provide a rationale for developing combinatorial therapies in TNBC, where the primary goals are to prevent dose escalation and decrease the chances of chemoresistance.[5]

In recent days, natural plant-derived compounds have received great attention as attractive sources for developing therapeutic regimens for TNBC. Dihydroartemisinin (DHA), an active hydrophobic metabolite of artemisinin, has shown significant potential in the treatment of TNBC through various mechanisms.[6] DHA is capable of mediating cell cycle arrest, inducing TRAIL-based apoptosis, inhibiting tumor growth and metastasis, selective toxicity and blocking angiogenesis.[7-10] On the other hand, piperine an hydrophobic alkaloid presents in black pepper (*Piper nigrum),* has received considerable attention for its anticancer effects across various malignancies. Beyond its pro-apoptotic, anti-proliferative, and anti-metastatic capacities, piperine mediated studies extends to include effects on chemoresistance.[11] It enhances the efficacy of TRAIL-based therapies, which are designed to induce apoptosis in cancer cells and making it a potent adjuvant in this therapeutic approach.[12, 13] Therefore, this study aimed to focus on the potential adjuvant effect of piperine on DHA by emphasizing on mode of action of drugs in combined way against TNBC. Furthermore, combination therapy using multiple drugs with different action sites effectively delays cancer adaptation and mutations.[14-17] It is very difficult

to achieve optimal effect due to their different biochemical activities and pharmacokinetics.[18] Additionally, this combination of free drugs often results in severe toxic side effects in the human body, posing a significant problem in clinical cancer treatments.[19]

Amphiphilic copolymer-based nanocarriers have garnered significant attention for hydrophobic drug delivery in cancer treatment due to their synthetic versatility, favorable size, biocompatibility, stability, controlled drug release, and altered pharmacokinetics compared to traditional agents.[20] In comparison to free drugs, nano-scaled drug carriers achieve better accumulation in solid tumors through the enhanced permeability and retention (EPR) effect.[21] Taking above discussions into account, poly(amino acids) are considered as much safer and much biocompatible in nature. These polymers are designed in such a manner that it can degrade at a rate that coincides with the desired function, which confirms the presence of material in biological system for particular duration without causing long term complications.[22] Further, targeted drug delivery systems are designed to enhance anticancer drug delivery to metastatic cancer cells and potentially bypass permeability barrier and efflux mechanisms. In order to achieve targeted delivery, receptor mediated drug delivery nanovehicles are designed. Many recent studies have demonstrated that Folic acid (FA) can be used in the development of tumor-targeting drug delivery systems because of its low molecular weight, nontoxicity, low cost, high affinity and binding specificity for over expressed folate receptor in cancer cells including TNBCs.[23, 24]

Our research group is focused on the development of biocompatible acrylate-amino acid based polymers. Previously, we have reported on p(NAPA) NPs which exhibited adjuvant properties on the innate immune system[25] and porous p(NAG) NPs which demonstrated as an excellent drug delivery carrier with enhanced anti-inflammatory effect.[26] In another report we have also reported the anticancer effect of combined DHA or Piperine loaded p(NAG-*co*-

NAPA)$_{(1:4)}$ NPs.[27] However, the underlying molecular pathways and cellular genes responsible for this inhibition were not studied there. Hence, there is a scope to modify the NPs with receptors and identify the potential biomarkers responsible for this therapeutic mechanism. In the above view, we have developed nanoformulations (NFs,), i.e., folate conjugated p(NAG-*co*-NAPA) NPs, [F-p(NAG-*co*-NAPA)$_{(1:4)}$] encapsulated with DHA or piperine and their pH sensitive drug release behavior were studied in normal and tumor microenvironment. Furthermore, the *in vitro* IC_{50} values of the NFs against the MDA-MB-231 cell line were determined to evaluate their TNBC inhibitory efficacy. Mechanistic insights were obtained through quantitative analysis of reactive oxygen species (ROS) generation, mitochondrial membrane potential (MMP), cell cycle arrest, and apoptosis using flow cytometry. Finally, the biomarkers responsible for TNBC inhibition are detected through gelatin zymography and RT-PCR studies.

3.2.3 Experimental

3.2.3.1 Materials

The chemicals and cell lines used for this work has been listed in Chapter 2 (Page No. 52-52, Section 2.2).

3.2.3.2 Synthesis of NAG and NAPA monomers and folate-p(NAG-*co*-NAPA)$_{(1:4)}$ (fP4) NPs

3.2.3.2.1 Synthesis of NAG and NAPA monomers

The synthesis procedure of NAG and NAPA monomers is given in Methodologies section of Chapter 2 (Page No. 53-55, Section 2.3.1.1. and 2.3.1.2.).

3.2.3.2.2 Synthesis of folate-p(NAG-*co*-NAPA)$_{(1:4)}$ NPs (fP4)

The synthesis method of folate-p(NAG-*co*-NAPA)$_{(1:4)}$ NPs (fP4) is described briefly in the Methodologies section of Chapter 2 (Page No. 55-56, Section 2.3.1.4.).

3.2.3.3. Physicochemical Characterizations of P4 andfP4 NPs

The characterization details, colloidal stability and morphology study of P4 and fP4 NPs are given in the Methodologies section of Chapter 2 (Page No. 57-59, Section 2.3.2. and 2.3.3.).

3.2.3.4. Preparation of Piperine or DHA loaded fP4 NPs (fDP4 and fPP4)

The preparation method of fDP4 and fPP4 NFs are given in the Methodologies section of Chapter 2 (Page No. 65-66, Section 2.3.6.1.). In this study, fP4 NPs is used to load DHA and Piperine.

3.2.3.5. *In vitro* drug release study of fPP4 and fDP4 NFs and Mathematical model fitting

The procedure for the *in vitro* drug release study of fDP4 and fPP4 NFs is described in the Methodologies section of Chapter 2 (Page No. 66, Section 2.3.6.2). Further, to predict the release kinetics, six different mathematical models were used to fit the release data (see supporting Eq. S3.2.1-S3.2.17). List of models are given in Chapter 2.

3.2.3.6. *In vitro* MTT assay of fP4 NPs

A detailed procedure for the MTT assay is described in the Methodologies section of Chapter 2 (Page No. 67, Section 2.3.7.1.). This study is performed using one cancer cell lines such as MDA-MB-231 for fP4 with a concentration range of 7.8125 to 1000µg/mL and for fPP4 AND fDP4 NFs with a concentration range of 25 to 2500µg/mL.

3.2.3.7. Evaluation of IC_{50} and combination index (CI) for fPP4, fDP4 and Co-NFs

The complete procedure for the evaluation of IC_{50} values for developed NFs is described in the Methodologies section of the Chapter 2 (Page No. 67-68, Section 2.3.7.2.).

3.2.3.8. Qualitative cellular uptake study by Confocal Microscopy

A detailed procedure for the cellular uptake study of P4, fP4, fPP4, fDP4, and Co-$NFs_{(8:2)}$ by MDA-MB-231 cells is described in the Methodologies section of the Chapter 2 (Page No. 70-71, Section 2.3.7.9.).

3.2.3.9. Quantitative cellular uptake and cellular internalization mechanism study

A detailed procedure for the cellular uptake study by P4 NPs in MDA-MB-231 cells is described in the Methodologies section of the Chapter 2 (Page No. 70, Section 2.3.7.8.).

3.2.3.10. Inhibition of *in vitro* MDA-MB-231 cell migration

The complete procedure for the in vitro inhibition of MDA-MB-231 cell migration study is described in the Methodologies section of Chapter 2 (Page No. 68, Section 2.3.7.4.). For this experiment fP4, fDP4, fPP4 and Co-$NFs_{(2:8)}$ were used at a concentration of 280µg/mL.

3.2.3.11. Apoptosis study by Annexin-V/ Propidium iodide

The complete procedure for the apoptosis study in MDA-MB-231 cell is described in the Methodologies section of Chapter 2 (Page No. 69, Section 2.3.7.6.). For this experiment P4, fP4, fDP4, fPP4 and Co-$NFs_{(2:8)}$ were used at a fixed concentration of 280µg/mL.

3.2.3.12. Cell cycle analysis

The complete procedure for the cell cycle analysis in MDA-MB-231 cell is described in the Methodologies section of Chapter 2 (Page No. 69, Section 2.3.7.5.). For this experiment P4, fP4, fDP4, fPP4 and Co-$NFs_{(2:8)}$ were used at a fixed concentration of 280µg/mL.

3.2.3.13. Determination of intracellular ROS and MMP

The complete procedure for the quantification of intracellular ROS generation and mitochondrial membrane potential (MMP) in MDA-MB-231 cell is described in the Methodologies section of Chapter 2 (Page No. 69-70, Section 2.3.7.7.). For this experiment P4, fP4, fDP4, fPP4 and Co-$NFs_{(2:8)}$ were used at a fixed concentration of 280µg/mL.

3.2.3.14. Estimation of extracellular MMP-2 and MMP-9 expression through Gelatin Zymography

The complete procedure for the gelatin zymography study in MDA-MB-231 cell is described in the Methodologies section of Chapter 2 (Page No. 71, Section 2.3.7.10.). For this experiment P4, fP4, fDP4, fPP4 and Co-$NFs_{(2:8)}$ were used at a fixed concentration of 280µg/mL.

3.2.3.15. Reverse Transcriptase polymerase chain reaction (RT-PCR)

To check the relative gene expression responsible for TNBC, RT-PCR experiment has been performed for all samples at 280µg/mL dose. The complete procedure for this study is described in the Methodologies section of Chapter 2 (Page No. 72-73, Section 2.3.7.11.).

3.2.3.16. Statistical Significance

Statistics applied on this work is described in Chapter 2 (Page No. 78, Section 2.4.).

3.2.4. Results and Discussions

3.2.4.1. Synthesis and Physicochemical characterization of monomers, P4 and fP4 NPs

To design the folate conjugated p(NAG-*co*-NAPA)$_{(1:4)}$ (fP4) NPs, at first two monomers were synthesized such as *N*-acryloyl glycine (NAG) and *N*-acryloyl-*L*-phenylalanine methyl (NAPA) ester. Their structures were confirmed through ^{1}H NMR (**Figure S3.1.2(a)** and **S3.1.3(a)**), ^{13}C NMR (**Figure S3.1.2(b)** and **S3.1.3(b)**) and FTIR spectroscopies (**Figure S3.1.4(a)** and **(b)**). The monomer synthesis is based on Schotten-Baumann reaction approach, where the amide groups were formed by reacting amine group of the monomers with the acryloyl chloride in basic medium.[28] Further, free radical polymerization mechanism was followed to synthesize P4 NPs as earlier reported in our work.[27] In brief: initially monomer in 1:4 ratio (NAG:NAPA) was dispersed in toluene, followed by addition of hexadecane as a co-stabilizer and DVB as a crosslinker. In a separate bottle, SDS in water solution was prepared and mixed to the above solution along with AIBN as an initiator. The solution was probe sonicated at desired parameters for 8-9minutes followed by stirring in oil bath at 70-75°C. After 16-20h of stirring, NPs was prepared and washed with water: ethanol (1:1) mixture for 8-10times for the complete removal of unreacted components. Further, these NPs were freeze dried for 24h and white powder was obtained and stored for FA conjugation. Here SDS acts as a surfactant, which prevent the aggregation formed during the emulsion process. P4 NP's structures were confirmed through ^{1}H NMR (**Figure 3.1.1(a)**), ^{13}C NMR (**Figure S3.1.5**) and FTIR spectroscopies (**Figure 3.1.1(a)**).

Further, FA has been conjugated to P4 NPs through EDC.HCl based click chemistry. For this, the esterification was performed in between FA with N-hydroxysuccinimide (NHS) in anhydrous DMSO in the presence of EDC.HCl and triethylamine as a catalyst as reported elsewhere.[29] Then, NHS-Folate in DMSO was incubated with P4 NPs suspension (pH 9.0) in 5

mM carbonate/bicarbonate buffer (pH 11.5) in dark for 12h at RT. The solution was centrifuged at 15,000RPM to settle down the fP4 NPs. The collected sediments were dialyzed against PBS (pH 7.4) for 3days followed by in water for another 4days. Finally, the collected fP4 NPs was freeze dried and used for further studies. The formation of fP4 NPs was confirmed through FTIR, UV-Vis and HR-TEM studies (**Figure 3.2.1**). Along with the distinct FTIR bands of P4 NP's in FTIR (3411cm^{-1}: 2° amine; 1739cm^{-1}:-C=O ester and 683cm^{-1} : aromatic -CH), one additional band is observed at 1604cm^{-1} which is for aromatic FA. Further, all bands of FA are also present in the fP4 NP's FTIR spectra (**Figure 3.2.1(a)**). Additionally, UV-Vis spectroscopy was performed to detect the additional band for FA and at λ_{max} 283nm a band is observed (**Figure 3.2.1 (b)**). This

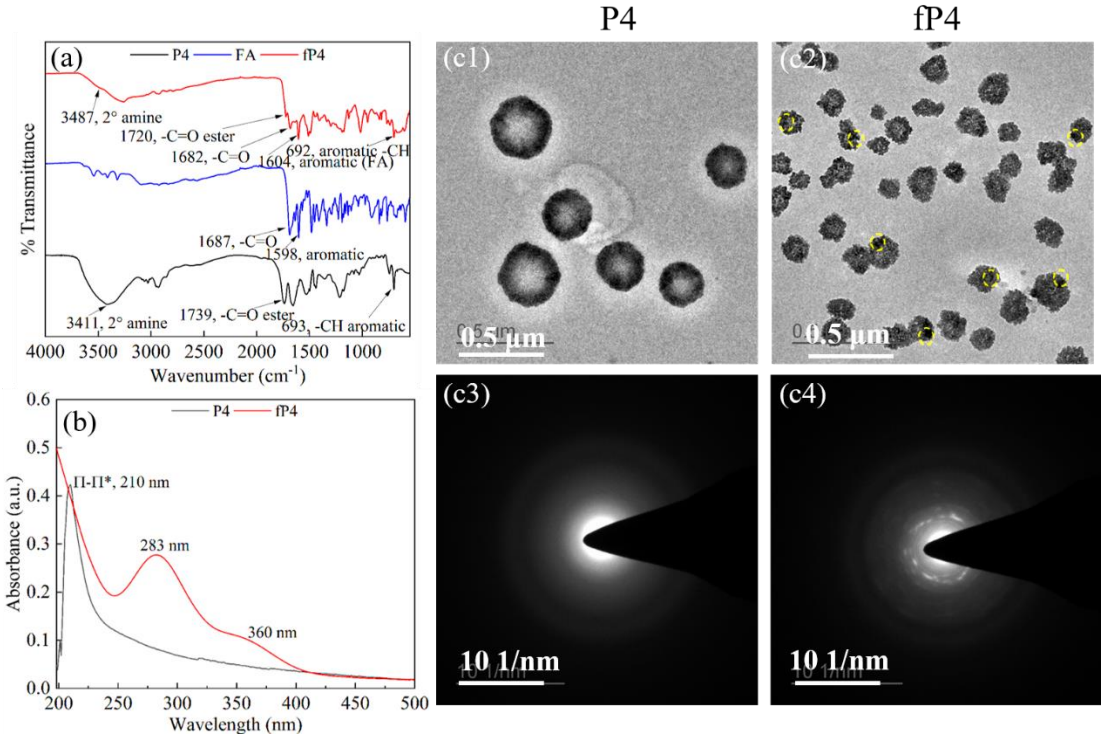

Figure 3.2.1. *Physicochemical characterization of P4 and fP4 NPs. Fig. (a) FTIR of P4, FA and fP4 NPs, (b) UV-Vis of P4 and fP4 NPs, (c1) and (c2) HR-TEM images of P4 and fP4 and (c3) and (c4) SAED pattern of (c1) and (c2), respectively. Yellow dash line circle in figure c2 represents the conjugation of FA over P4 NPs.*

283nm band belongs to FA and interestingly in P4 NPs this band is absent, which further confirms the successful conjugation of FA with P4 NPs. In order to visualize the changes in morphology of the P4 NPs after FA conjugation, HR-TEM images were acquired (**Figure 3.2.1(c2)**). In comparison with P4 NPs (**Figure 3.2.1(c1)**), it is clearly observed that, the structure has been slightly altered and some impressions (yellow dashed line circle) were visualized over each of the fP4 NPs. Further, the SAED pattern of the fP4 NPs was recorded (**Figure 3.2.1(c4)**). Although P4 NPs are amorphous in nature (**Figure 3.2.1(c3)**), however fP4 NPs are semicrytalline. This crystallinity in fP4 NPs characterize the presence of FA in the developed NPs. Therefore, the obtained results from various physicochemical studies confirms the successful preparation of fP4 NPs, which can be further used for *in vitro* studies to achieve maximum targeting efficiencies towards TNBC.

3.2.4.2. Preparation, Characterization and *in vitro* drug release behavior of fPP4 and fDP4 NFs

After successful preparation of fP4 NPs, hydrophobic drugs piperine and DHA were used to encapsulated inside the NPs separately and designated as fPP4 and fDP4 NFs, respectively. The LE% and EE% were calculated for both the NFs and represented in **Table 3.2.1**. It was observed that the encapsulation efficiencies for DHA (93.87%) is better as compared to piperine (34.95%). This discrepancy in encapsulation efficiency is due to the extent of hydrophobicity of the two drugs. Further, it can be highlighted that the higher EE% in fDP4 is due to the complex hydrophobic ring structure of DHA with respect to piperine.

Table 3.2.1. Physicochemical properties of fP4 NPs, fPP4 and fDP4 NFs.

Nanoparticles	Size (d.nm)	Zeta potential (mV)	PDI	EE (%)	LE (%)
fP4	213.0	-10.21	0.787	-	-
fPP4	429.7	-21.54	1.000	34.95	25.89
fDP4	492.6	-23.62	1.000	93.87	48.41

To check the thermal stability of all the NFs, TGA was carried out from 25°C to 600°C and it was observed that all the developed NFs are quite stable upto 50°C. The minor weight loss (~4-5%) at 100°C is due to the surface moisture. The degradation above 170°C is due to the degradation of polymer chain or breaking of some crosslinking bonds. It can be noted that, after encapsulation also, fPP4 and fDP4 NFs showed good thermal stability (**Figure 3.2.2 (a)**) and can be used for healthcare applications. Further, XRD was performed for the prepared NFs (**Figure 3.2.2(b)**). XRD results clearly, depicts the intactness of the semicrystaline nature of the fP4 NPs after loading of drugs into it. The release profile of the NFs holds potential significance in the field of healthcare and therapeutics. Therefore, the *in vitro* drug release behavior for both the NFs was studied in two different mediums (pH 6.8 and 7.4) for 30 days by following dialysis bag approach and shown in **Figure 3.2.2(c)** and **(d)**. It is clearly observed that, in both the medium, release is occurred in step wise manner. It is interesting to mention here that, fDP4 NFs showed firster release at 6.8 pH as compared to other NFs in other mediums. It can be noted that, upto 30days fPP4 and fDP4 NFs has released only 20% and 45% of the loaded drug, respectively, which means further scope is there for longer and sustained release. The stepwise release is observed here, may be due to the periodically polymer chains are breaking and due to the controlled pH dependent drug release behavior achieved.[30]

Further, best drug release kinetic model was determined by fitting all the drug release data to six different standard mathematical models (Zero order, first order, Higuchi, Hixson Crowell, Korsmeyer Peppas and Weibull) and depending on the R^2 value, drug release type has been established (**Figure 3.2.2(e)-(h)**). All the mathematical models depict different types of delivery modalities. Higuchi model shows diffusion controlled release of drugs through a square root time relation whereas Korsmeyer-Peppas represents the non-fickian diffusion of drugs specially used

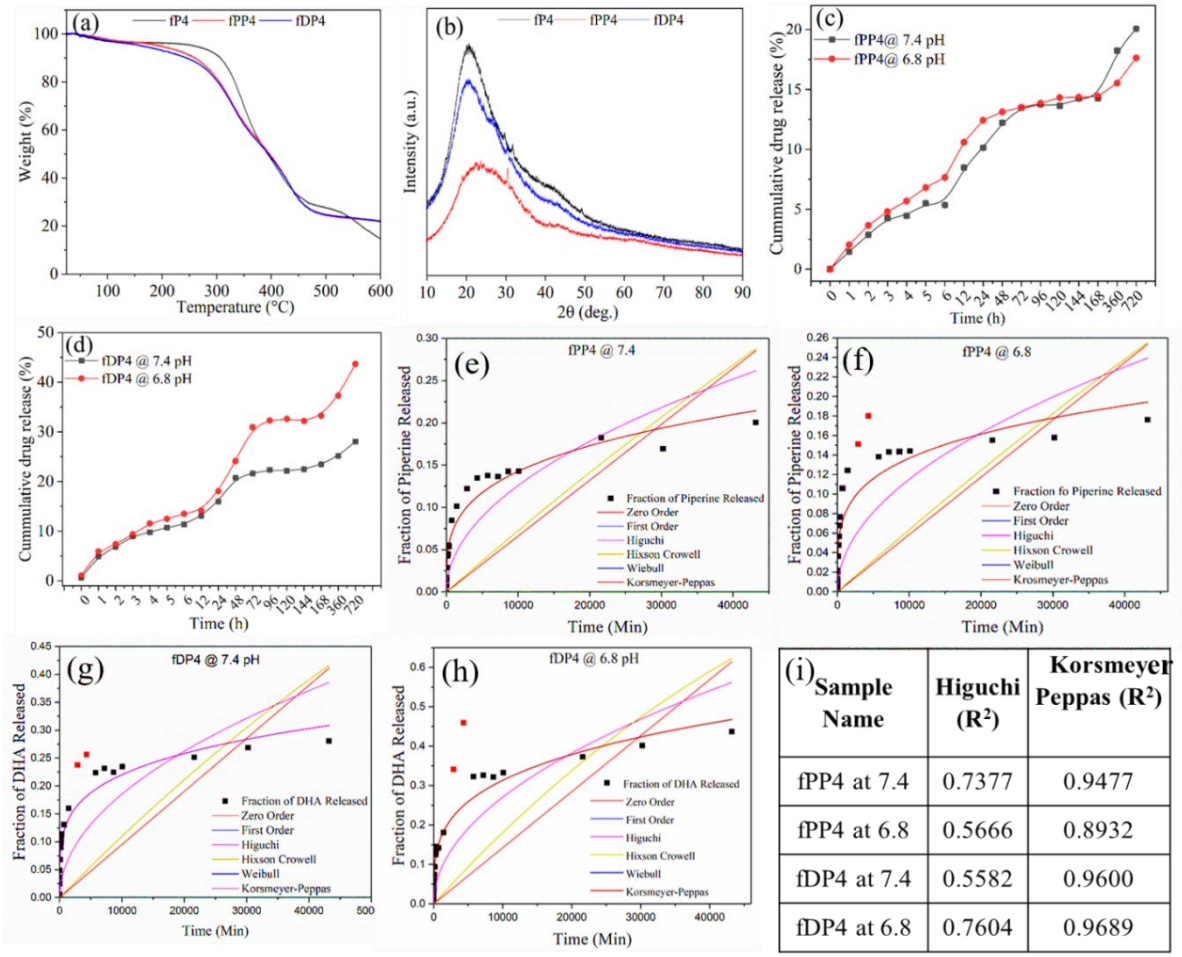

(i)

Sample Name	Higuchi (R^2)	Korsmeyer Peppas (R^2)
fPP4 at 7.4	0.7377	0.9477
fPP4 at 6.8	0.5666	0.8932
fDP4 at 7.4	0.5582	0.9600
fDP4 at 6.8	0.7604	0.9689

Figure 3.2.2. *Thermal stability, in vitro drug release and release kinetics study of fP4 NPs, fPP4 and fDP4 NFs. Fig. (a) and (b) TGA and XRD of fP4 NPs, fPP4 and fDP4 NFs, (c) and (d) in vitro drug release % of NFs at pH 6.8 and 7.4, (e)-(h) mathematical model fitting of drug release kinetics data in six different standard models (Zero, First, Higuchi, Hixson Crowell, Weibull, and Korsmeyer-Peppas), and (i) regression coefficient (R^2) of two best fitted mathematical models.*

for polymer systems. Out of six drug release kinetics, Higuchi and Korsmeyer-Peppas models yielded the greater R^2 value (**Figure 3.2.2(i)**). All other models are having negative R^2 value, which represents the poor fitting of release data set with those models (**Table S3.2.1**). Further, in between Higuchi and Korsmeyer-Peppas models, R^2 value are higher for Korsmeyer-Peppas model for both the NFs in both the condition. Hence, the drug release mechanism is adhered to Korsmeyer-Peppas model. This R^2 value > 0.89 and n< 0.45 indicate that it is following a passive diffusion mechanism by controlling the diffusion of drugs from the non-swellable and non-erodible polymer systems.[31] All the theory behind the mathematical modelling, equations and the assumptions for the models are provided in the supplementary. Additionally, a table has been provided by listing all the obtained constant values during the fitting of release data to different models for each NFs in both the pH condition (**Table S3.2.2**).

3.2.4.3. *In vitro* cytotoxicity and migratory effect of fP4 NPs, fPP4, fDP4, and Co-NFs$_{(8:2)}$

To assess the cell viability % of fP4 NPs, MTT study was performed with MDA-MB-231 cell line for 7.8 to 1000µg/mL (**Figure 3.2.3(a)**). The obtained cell viability % are 94.18±0.37, 93.0±1.14, 92.21±0.21, 89.01±0.08, 85.92±0.36, 74.78±0.32, 68.84±0.38 and 62.21±0.50 for 7.8, 15.9, 31.25, 62.5, 125, 250, 500 and 1000µg/mL, respectively. Further, cytotoxicity of designed NFs against TNBC were checked for different doses varying from 25 to 2500µg/mL (**Figure 3.2.3(b-d)**). These results clearly depict that, treatment of TNBC is purely dose dependent. The IC_{50} values obtained for fPP4 and fDP4 NFs were 388µg/mL and 330µg/mL, respectively. In order to use as combination therapy, by varying the ratios of NFs, TNBC inhibition was checked (**Figure 3.2.3(c)** and **S3.2.1**). The ratio 8:2 (fDP4:fPP4) was found to be promising. Further, different concentrations of fDP4:fPP4 at 8:2 ratios were used to check the TNBC inhibition efficiency. The IC_{50} value was also calculated and found to be 280µg/mL. Furthermore, by using the Chou and

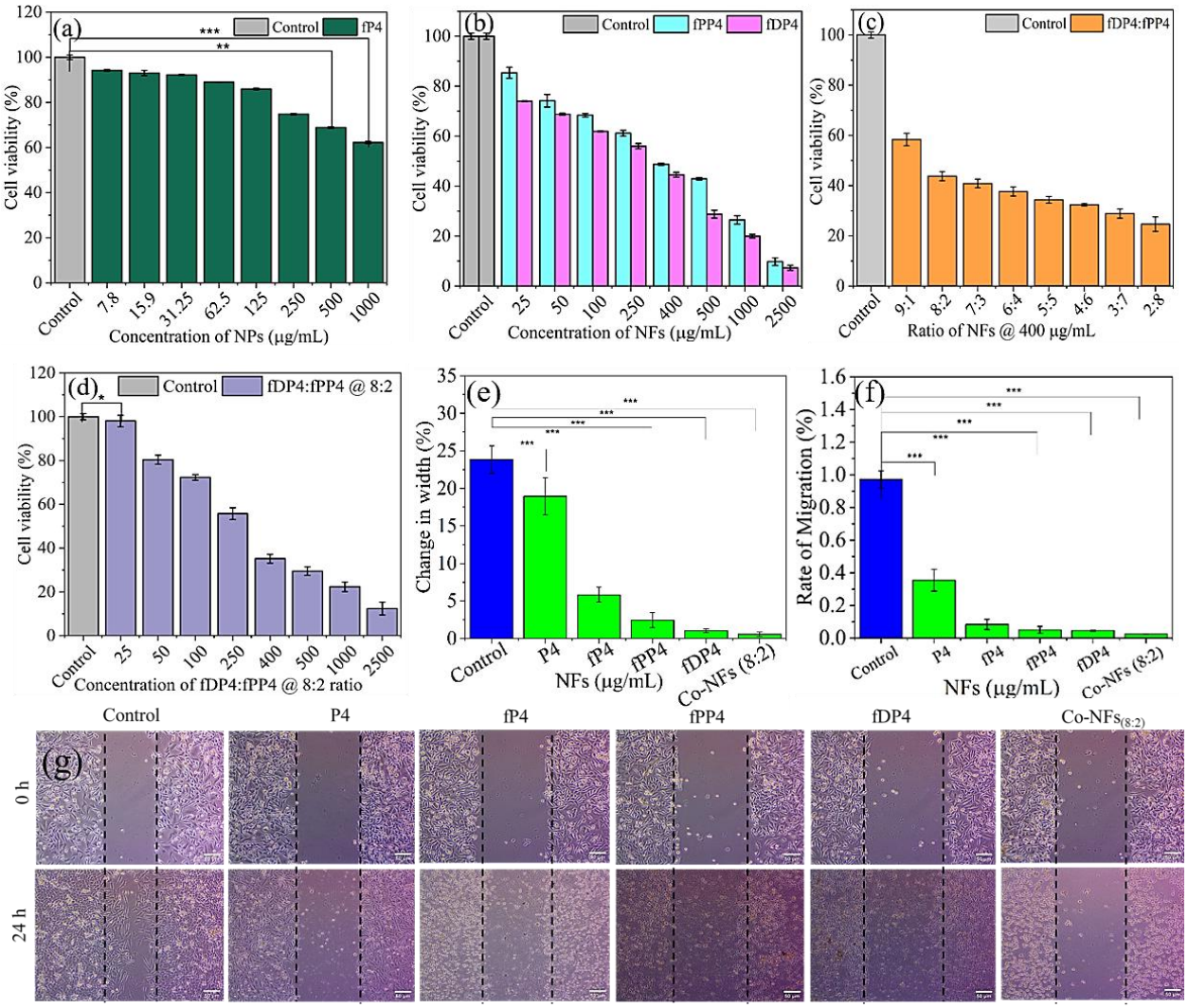

Figure 3.2.3. *In vitro cytotoxicity and migratory effect of NFs in MDA-MB-231 cells. Fig. (a)-(d) treatment efficiency of NPs and NFs studied against TNBC with different concentrations, (e) and (f) the change in width (%) and rate of migration (%), respectively calculated from the microscopic images (g) by Fiji imageJ software, and (g) microscopic images of wound scratch assay (scale: 50µm). For figure (b-d) all the concentrations are showing significant difference of '***' with control.*

Talalay equation (Eqn. 3.2.3), CI was calculated. This CI value was found to be 0.8, which implies the synergetic effect of the fDP4:fPP4 at 8:2 ratio rather than additive or antagonism effect.

To prevent metastasis caused by the tumor cells, it is required to study the migration behavior of the designed NFs against the targeted cells. To study the *in vitro* anti-proliferative and anti-

migration effect of the designed NFs, wound scratch study was performed with the MDA-MB-231 cell lines upto 24h at 280µg/mL (**Figure 3.2.3(e-g)**). The change in width % values are found to be 23.82±1.82, 18.94±2.45, 5.83±1.00, 2.44±1.00, 1.03±0.25, and 0.54±0.29 for control, P4, fP4, fPP4, fDP4 and Co-NFs$_{(8:2)}$, respectively (**Figure 3.2.3(e)**). In comparison to control and P4 NPs, the change in width % is negligible for NFs and Co-NFs$_{(8:2)}$. Similarly, the rate of cell migration for control, P4, fP4, fPP4, fDP4 and Co-NFs$_{(8:2)}$ are found to be 0.97±0.05, 0.35±0.06, 0.08±0.03, 0.05±0.02, 0.04±0.001 and 0.02±0.002, respectively (**Figure 3.2.3(f)**). The rate of migration for Co-NFs$_{(8:2)}$ found is very low (0.02%). Thus, based on the above results, further *in vitro* studies were performed by using 280µg/mL of all the NFs including P4 and fP4 NPs as control.

3.2.4.4. Cellular internalization mechanism of P4 NPs, Morphology study and mitochondrial ROS generation through NFs post treatment

To achieve effective drug delivery at the targeted site, the NPs should get internalized inside the targeted cells. With respect to this, cellular internalization mechanism for P4 NPs was studied though flow cytometry study by using standard endocytosis inhibitors (**Figure 3.2.4(a)**). Among three selected inhibitors, amiloride.HCl inhibits the micropinocytosis, chloropremazine inhibits clathrin mediated endocytosis and Nystatin inhibits calveoli mediated endocytosis. The drastic diffrence in uptake % for chloropremazine treated cells (77.33%) with respect to amiloride (99.12%) and nystatin (98.60) inhibitors confirms that, P4 NPs shows clathrin mediated endocytosis. It can be noted that, in case of without inhibitors, the uptake is 99.19%, which implies that the designed NPs are showing ~100% internalization. Further, to visualize the changes in morphology after treatment with control, NPs, NFs, Co-NFs$_{(8:2)}$, confocal microscopy study was performed (**Figure 3.2.4(b)**). It is clearly visible that, for control and P4 NPs, elongated actin filament with intact nuclear structure are persist post treatment, whereas for fP4 NPs, the cell

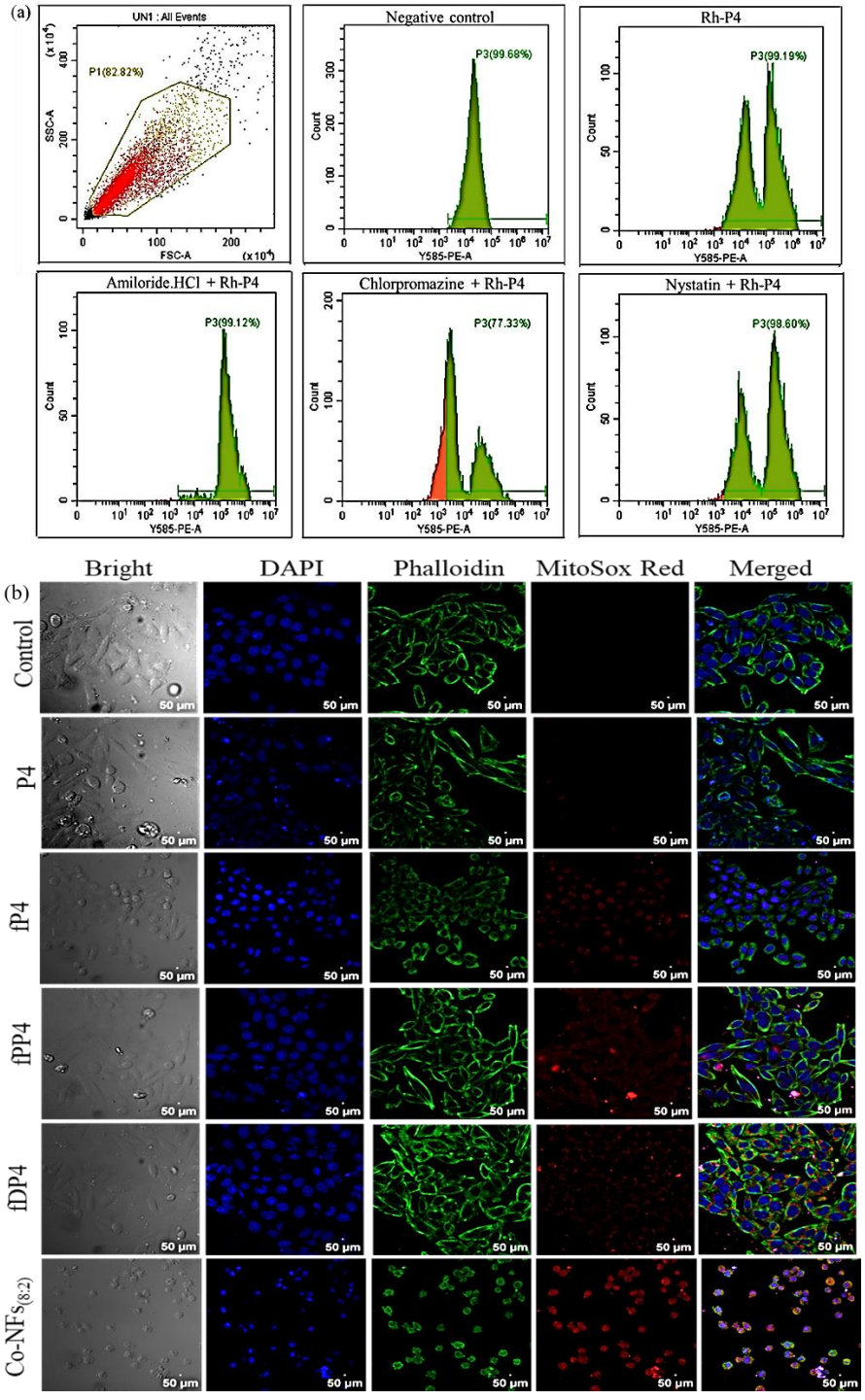

Figure 3.2.4. *Cellular uptake study of P4, fP4 NPs, fPP4, fDP4 and Co-NFs$_{(8:2)}$. Fig. (a) the cellular internalization mechanism of Rh-P4 NPs through flow cytometry, and (b) morphological changes study due to NFs through confocal microscopy in MDA-MB-231 cells (scale: 50µm). DAPI (blue), Phalloidin (green), MitoSox (red) used for nuclear, actin filament and mitochondrial ROS staining.*

structure has been partially altered. This alteration in structure is due to the conjugation of FA with the P4 NPs. Further, for NFs, the observed structures are also quite similar to the fP4 NPs i.e., squeezed actin filament with porous structure of nucleus. However, in case of Co-NFs, the complete change in morphology of the cells (oval to round shape) with distorted nucleus is observed. This distinct change in the shape and structure of the MDA-MB-231 cells post treatment with Co-NFs suggest the NF's potential inhibition against TNBC. In addition to this, mitosox red was used here to check the generation of mitochondrial ROS in different treatment group after incubation or treatment with 280μg/mL of concentration to MDA-MB-231 cells. The microscopic images clearly represent that from control and P4 NPs, no any ROS has been generated whereas from fP4 to Co-NFs, the fluorescent intensity has been increased. This increase in red fluorescence intensity depicts the NF's potential in mitochondrial mediated cell death by producing ROS inside the cell. However, an extensive flow cytometry study was performed to confirm the reason behind MDA-MB-231 cell death.

3.2.4.5. Effect of fPP4, fDP4, and Co-NFs$_{(8:2)}$ on cell death, cell cycle and TNBC inhibition mechanism

The IC_{50} values for NFs and Co-NFs$_{(8:2)}$ were obtained from the MTT assay of MDA-MB-231 cells and fixing the concentration at 280μg/mL, an extensive flow cytometry study was performed with all the samples to check the cell death type, cell cycle arrest and mechanism behind the cell death (**Figure 3.2.5**). Initially, the cell death study was performed to confirm the type of cell death (apoptotic or necrotic) take place due to the NPs and NFs by using Annexin-V/PI. As reported earlier, P4 is inducing partial necrotic cell death (14.10%) as compared to control sample (89.47%).[27] fP4 NPs are inducing increase necrotic death as compared to control and P4 samples, which is corroborating well with the earlier cell viability results (**Figure 3.2.3(a)**). Comparing fPP4

and fDP4, fPP4 induce more necrotic cell death (extent of live cells: 44.85%, early apoptotic cells: 0.17%, late apoptotic cells: 13.06% and necrotic cells: 41.92%). However, fDP4 promote early apoptotic cell death (extent of live cells: 55.80%, early apoptotic cells: 22.19%, late apoptotic cells:13.43% and necrotic cells: 8.57%). Hence, it justified the use of considered Co-NF's ratio fDP4:fPP4, i.e., 8:2 for the inhibition of TNBC. The use of DHA with folic acid conjugation upsurged the early apoptotic stage from 0.17% to 22.19%, which is highly remarkable for targeting TNBC. Furthermore, Co-$NFs_{(8:2)}$ showed increase number of cells in late apoptotic stage (21.91%) and necrotic stage (14. 46%). As it a combination therapy of two drugs with FA conjugation over the NP's surface, it is showing mixture of apoptosis and necrosis mediated cell death. Thus, instead of individual NFs, the Co-$NFs_{(8:2)}$ can be used for TNBC inhibition.

To establish the potential TNBC inhibition properties of the NFs, one important key aspect is controlling cell cycle of MDA-MB-231 cells (**Figure 3.2.5(b)**). Based on the cell cycle study, comparing to control (62.88%), for P4 (67.11%) and fP4 NPs (69.21%), the reduction in cell viability is primarily caused due the reduction in G0-G1 phase. In contrast, for fPP4 and fDP4 NFs, although G0-G1 phase are in similar range, a drastic change has been observed for S (14.41%) and G2-M (21.48%) phases of control group. For fPP4 NFs, S phase decreases to 6.32%, whereas, G2-M phase increases to 26.70%. In similar manner, for fDP4 NFs, S phase decreases to 11.04%, whereas, G2-M phase increases to 25.51%. This implies that for both the NFs, G2-M phase is dominant. In similar manner, for Co-$NFs_{(8:2)}$ the G2-M phases has been increased from 21.48% (control group) to 25.34%. It can stated that the Co-$NFs_{(8:2)}$ inhibited the cell growth by arresting the cell cycle at G2-M phase. The TNBC inhibition mechanism was further confirmed through quantification of ROS and MMP using DCFDA and Rh-123 as two fluorescent dyes, respectively.

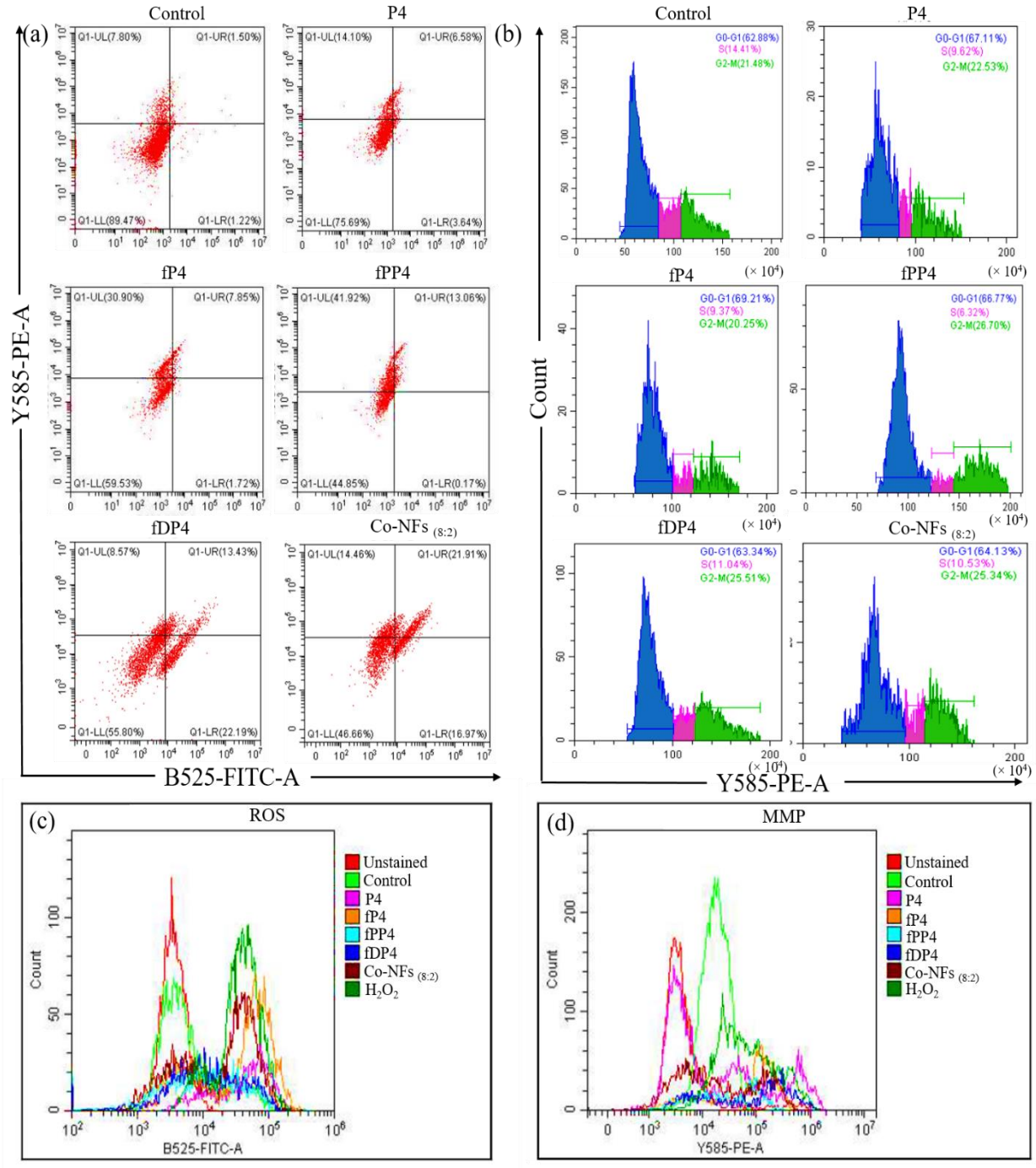

Figure 3.2.5. *Annexin-V/PI flow cytometry study, (b) cell cycle analysis, quantification of (c) ROS and (d) MMP of P4, fP4, fPP4, fDP4 and Co-NFs$_{(8:2)}$ at 280µg/mL with unstained (only cells) and control (only dye) samples.*

The green fluorescent intensity generated post treatment is directly proportional to the amount of ROS generated, whereas for MMP, decrease in fluorescence intensity leads to the mitochondrial membrane depolarization, and ultimately leads to cell death. For ROS, all the samples including Co-NFs$_{(8:2)}$, shift towards positive control (H_2O_2), which depicts that all the NF's have potential to inhibit TNBC by producing ROS. Particularly for Co-NFs$_{(8:2)}$, the fluorescence intensity value approached in the range of ~10^3-10^5 (**Figure 3.2.5(c)**). However, in case of MMP, all the treatment samples are overlap with the positive control (H_2O_2) and the plots are distributed in the region of ~10^3-10^6 order of fluorescence intensity (**Figure 3.2.5(d)**). The variation in fluorescence intensity range of ROS and MMP (~100x) clearly depicted that, the underlying TNBC inhibition or killing mechanism through Co-NFs$_{(8:2)}$ is governed by the mitochondrial membrane potential mediated cell death. Therefore, it can be stated that, the final Co-NFs$_{(8:2)}$ exhibited early apoptotic cell death by arresting G2-M phase following the MMP based killing mechanism.

3.2.4.6. Modulation of Gene Expressions via Co-NFs in TNBC

In order to detect the responsible biomarkers for the inhibition for TNBC through NFs and Co-NFs$_{(8:2)}$, two cell based studies were taken into consideration. The change in expression level of potential biomarkers were quantified by performing gelatin zymography and RT-PCR for all the samples at 280µg/mL. From gelatin zymography study, two major angiogenic proteins expressions such as MMP-2 and MMP-9 were checked (**Figure 3.2.6(a)**). It is clearly observed in the figure that, for all the samples including control, all four types of MMP-2 and MMP-9 proteins are expressed. Further, with respect to control, in the order of P4 NPs to Co-NFs$_{(8:2)}$ a sharp decrease in band intensity is observed. This decrease in band intensity suggest the antiangiogenic and non-invasion nature of the Co-NFs$_{(8:2)}$. Further, RT-PCR study was performed to quantify the expression of some preliminary biomarkers responsible for inhibiting TNBC, such

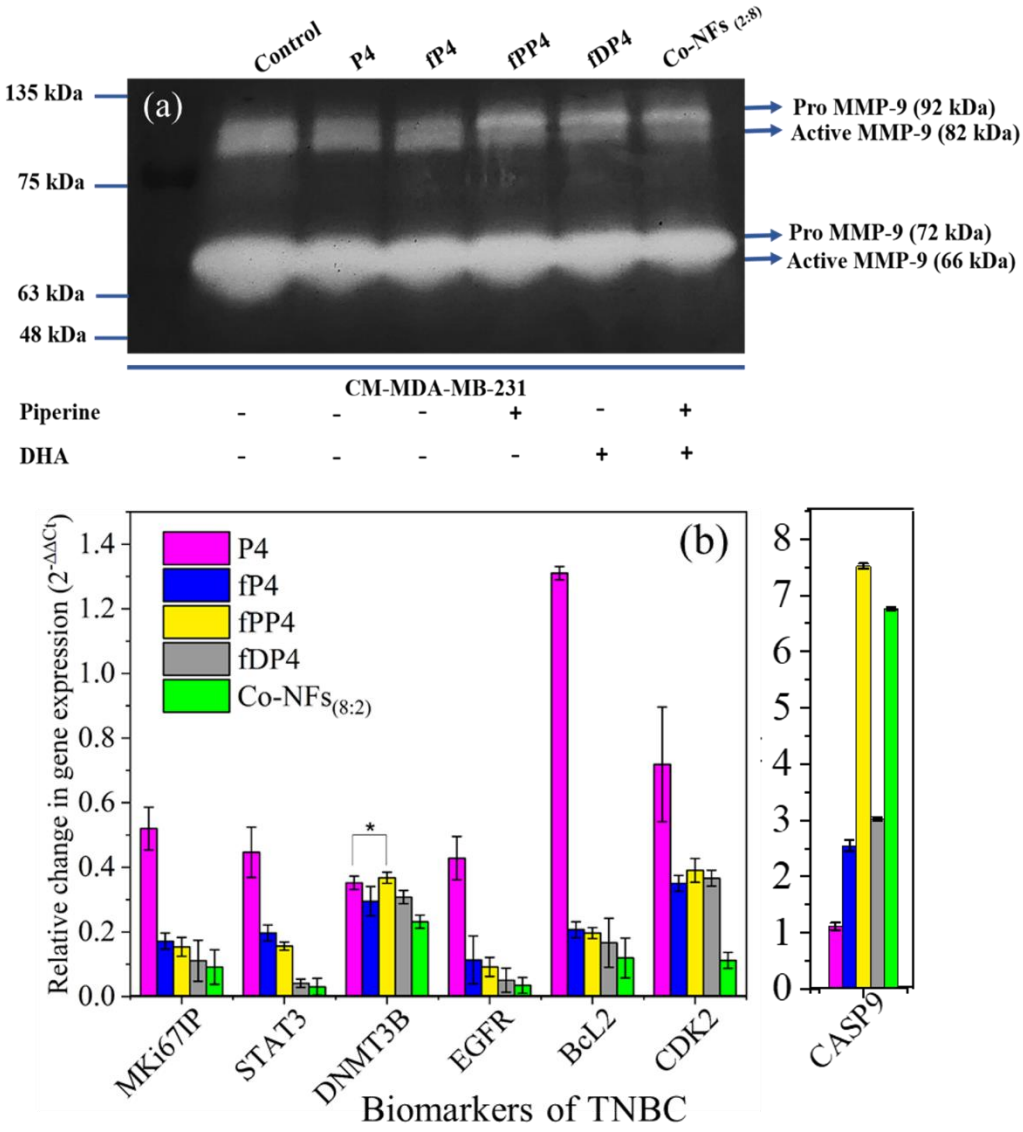

Figure 3.2.6. *Modulation in expressions of potential TNBC biomarkers due to treatment with developed NFs. Fig. (a) represents the expression of MMP-2 and MMP-9 through gelatin zymography assay (CM: Conditioned media), and (b) expression of MKi67IP, STAT3, DNMT3B, EGFR, BcL2, CDK2 and Casp9 through RT-PCR study of post treatment with NFs. For figure (b) all the NFs are showing significant difference of '***' with P4 NPs for all the biomarkers.*

as Ki67, DNMT3B, BcL2, CDK2, STAT3, EGFR and Casp9 (**Figure 3.2.6(b)**). Ki67 is a TNBC proliferation marker and the decrease level of Ki67 represents the inhibition of TNBC.[32] DNMT3B plays a crucial role by influencing the DNA methylation and modulate the genetic

expression in TNBC.[33] BcL2 is an anti-apoptotic protein and its inhibition plays a significant role in achieving therapeutic target for TNBC.[34] Inhibition of CDK2 can help in reduction of cell proliferation, cell cycle arrest or even cell death in TNBC.[35] The suppression in STAT3 signal can inhibit TNBC progression and eventually increase the sensitivity of cells towards chemotherapy. [36] Further, the decrease in EGFR expression can directly lead to the decrease in cell proliferation, increase in apoptosis and enhancement of chemosensitivity [37] and Casp9 is important due to the capacity of triggering apoptotic cell death with tumor suppression and metastasis [38]. Therefore, as per the primary requisite for TNBC inhibition, biomarkers like Ki67, DNMT3B, BcL2, CDK2, STAT3, and EGFR are significantly downregulated; and casp9 is remarkably upregulated for Co-$NFs_{(8:2)}$ with respect to P4 and fP4 NPs (**Figure 3.2.6(b)**). Finally, these biomarker's expression levels demonstrate DNA targeting capacity with anti-proliferative, anti-apoptotic, anti-metastasis, non-invasion and antiangiogenic nature of the Co-$NF_{(8:2)}$ and suggest it's future therapeutic potential for TNBC treatment.

3.2.5. Summary and Conclusions for this part

The current challenges associated with the targeted therapy is drug resistance, tumor heterogeneity and limitation in predicting the responsible biomarkers for TNBC. Our earlier work has reported the anticancer effect of combined DHA or Piperine loaded P4 NPs. However, the underlying molecular pathways and cellular genes responsible for inhibiting TNBC are not elucidated. Further, there is a scope to achieve improved targeting efficiency by modifying the NPs with receptors. In this line, we have conjugated the P4 NPs with FA to achieve maximum TNBC targeting efficiency through click chemistry method. Physicochemical properties were studied to ensure their successful synthesis followed by *in vitro* studies to check their TNBC efficiency. The prepared NFs exhibited an excellent pH dependent drug release through passive diffusion mechanism. The low

IC_{50} value of Co-$NFs_{(8:2)}$, revealed the synergetic treatment efficiency of TNBC rather than antagonism or additive behaviour. The flow cytometry results depicted mitochondrial membrane potential mediated cell death in TNBC through arresting G2-M phase. Gelatin zymography study revealed the suppression of MMP-2/MMP-9 activity by focusing the anti-angiogenic non-invasive properties of CO-NFs. RT-PCR results confirms the anti TNBC nature of Co-NFs by demonstrating the changes in specific oncogenic markers such as DNMT3B, EGFR, Ki67, STAT3, Bcl2, CDK2 and Casp9 which further confirm the DNA-targeting, anti-proliferative and pro-apoptotic nature of Co-NFs. However, to comprehend the anti TNBC potential of the NFs and for successful clinical translation, *in vivo* studies are taken under consideration and will be reported as the advancement of this work.

3.2.6. References

1. Sedeta, E.T., B. Jobre, and B. Avezbakiyev, *Breast cancer: Global patterns of incidence, mortality, and trends*. 2023, American Society of Clinical Oncology.
2. WHO, *Breast Cancer*. 2024, World Health Organization.
3. Li, X., et al., *Triple-negative breast cancer has worse overall survival and cause-specific survival than non-triple-negative breast cancer.* Breast Cancer Research and Treatment, 2017. **161**(2): p. 279-287.
4. Bianchini, G., et al., *Triple-negative breast cancer: challenges and opportunities of a heterogeneous disease.* Nature Reviews Clinical Oncology, 2016. **13**(11): p. 674-690.
5. Bianchini, G., et al., *Treatment landscape of triple-negative breast cancer — expanded options, evolving needs.* Nature Reviews Clinical Oncology, 2022. **19**(2): p. 91-113.
6. Kongpatanakul, S., et al., *Comparative study of dihydroartemisinin and artesunate safety in healthy Thai volunteers.* International journal of clinical pharmacology and therapeutics, 2009. **47**(9): p. 579-586.
7. Lu, J.-J., et al., *Dihydroartemisinin induces apoptosis in HL-60 leukemia cells dependent of iron and p38 mitogen-activated protein kinase activation but independent of reactive oxygen species.* Cancer Biology & Therapy, 2008. **7**(7): p. 1017-1023.
8. Chen, H.-H., et al., *Antimalarial dihydroartemisinin also inhibits angiogenesis.* Cancer Chemotherapy and Pharmacology, 2004. **53**(5): p. 423-432.
9. Ba, Q., et al., *Dihydroartemisinin Exerts Its Anticancer Activity through Depleting Cellular Iron via Transferrin Receptor-1.* PLOS ONE, 2012. **7**(8): p. e42703.

10. Lu, J.-J., et al., *Dihydroartemisinin accelerates c-MYC oncoprotein degradation and induces apoptosis in c-MYC-overexpressing tumor cells.* Biochemical Pharmacology, 2010. **80**(1): p. 22-30.
11. Kumar, S., et al., *Role of piperine in chemoresistance*, in *Role of nutraceuticals in cancer chemosensitization*. 2018, Elsevier. p. 259-286.
12. Abdelhamed, S., et al., *Piperine Enhances the Efficacy of TRAIL-based Therapy for Triple-negative Breast Cancer Cells.* Anticancer Research, 2014. **34**(4): p. 1893.
13. Quijia, C.R. and M. Chorilli, *Piperine for treating breast cancer: A review of molecular mechanisms, combination with anticancer drugs, and nanosystems.* Phytotherapy Research, 2022. **36**(1): p. 147-163.
14. Duan, X., et al., *Smart pH-Sensitive and Temporal-Controlled Polymeric Micelles for Effective Combination Therapy of Doxorubicin and Disulfiram.* ACS Nano, 2013. **7**(7): p. 5858-5869.
15. Chen, T., et al., *Cancer-cell-membrane-camouflaged supramolecular self-assembly of antisense oligonucleotide and chemodrug for targeted combination therapy.* Nanoscale, 2023. **15**(4): p. 1914-1924.
16. Lin, L., et al., *Formation of ssDNA nanotubes from spherical micelles and their use as a delivery vehicle for chemotherapeutics and senolytics to triple negative breast cancer cells.* Nanoscale, 2023. **15**(22): p. 9801-9812.
17. Liu, Y., et al., *Amplification of oxidative stress via intracellular ROS production and antioxidant consumption by two natural drug-encapsulated nanoagents for efficient anticancer therapy.* Nanoscale Advances, 2020. **2**(9): p. 3872-3881.
18. Hu, C.-M.J., S. Aryal, and L. Zhang, *Nanoparticle-assisted Combination Therapies for Effective Cancer Treatment.* Therapeutic Delivery, 2010. **1**(2): p. 323-334.
19. Zhao, Y., D.Y. Alakhova, and A.V. Kabanov, *Can nanomedicines kill cancer stem cells?* Advanced Drug Delivery Reviews, 2013. **65**(13): p. 1763-1783.
20. Kim, S., et al., *Overcoming the barriers in micellar drug delivery: loading efficiency, in vivo stability, and micelle–cell interaction.* Expert Opinion on Drug Delivery, 2010. **7**(1): p. 49-62.
21. Peer, D., et al., *Nanocarriers as an emerging platform for cancer therapy.* Nature Nanotechnology, 2007. **2**(12): p. 751-760.
22. Thompson, M. and C. Scholz *Highly Branched Polymers Based on Poly(amino acid)s for Biomedical Application*. Nanomaterials, 2021. **11**, DOI: 10.3390/nano11051119.
23. Sudimack, J. and R.J. Lee, *Targeted drug delivery via the folate receptor.* Advanced Drug Delivery Reviews, 2000. **41**(2): p. 147-162.
24. Sega, E.I. and P.S. Low, *Tumor detection using folate receptor-targeted imaging agents.* Cancer and Metastasis Reviews, 2008. **27**(4): p. 655-664.
25. Yamala, A.K., et al., *Poly-N-acryloyl-(l-phenylalanine methyl ester) hollow core nanocapsules facilitate sustained delivery of immunomodulatory drugs and exhibit adjuvant properties.* Nanoscale, 2017. **9**(37): p. 14006-14014.
26. Gupta, P.S., et al., *Nitric oxide releasing novel amino acid-derived polymeric nanotherapeutic with anti-inflammatory properties for rapid wound tissue regeneration.* Nanoscale, 2024. **16**(4): p. 1770-1791.

27. Patra, S., et al., *Organ-targeted drug delivery systems (OTDDS) of poly[(N-acryloylglycine)-co-(N-acryloyl-l-phenylalanine methyl ester)] copolymer library and effective treatment of triple-negative breast cancer.* Journal of Materials Chemistry B, 2025. **13**(12): p. 3876-3894.
28. Bentolila, A., et al., *Poly(N-acryl amino acids): A New Class of Biologically Active Polyanions.* Journal of Medicinal Chemistry, 2000. **43**(13): p. 2591-2600.
29. Lee, R.J. and P.S. Low, *Delivery of liposomes into cultured KB cells via folate receptor-mediated endocytosis.* Journal of Biological Chemistry, 1994. **269**(5): p. 3198-3204.
30. Zhang, P., et al., *A programmable polymer library that enables the construction of stimuli-responsive nanocarriers containing logic gates.* Nature Chemistry, 2020. **12**(4): p. 381-390.
31. Gao, Y., et al., *In Vitro Release Kinetics of Antituberculosis Drugs from Nanoparticles Assessed Using a Modified Dissolution Apparatus.* BioMed Research International, 2013. **2013**(1): p. 136590.
32. Keam, B., et al., *Ki-67 can be used for further classification of triple negative breast cancer into two subtypes with different response and prognosis.* Breast Cancer Research, 2011. **13**(2): p. R22.
33. Man, X., et al., *DNMT3A and DNMT3B in Breast Tumorigenesis and Potential Therapy.* Frontiers in Cell and Developmental Biology, 2022. **Volume 10 - 2022**.
34. Inao, T., et al., *Bcl-2 inhibition sensitizes triple-negative human breast cancer cells to doxorubicin.* Oncotarget, 2018. **9**(39).
35. Cheung, A., et al., *CDK Inhibition Primes for Anti-PD-L1 Treatment in Triple-Negative Breast Cancer Models.* Cancers, 2022. **14**(14): p. 3361.
36. Qin, J.-J., et al., *STAT3 as a potential therapeutic target in triple negative breast cancer: a systematic review.* Journal of Experimental & Clinical Cancer Research, 2019. **38**(1): p. 195.
37. Masuda, H., et al., *Role of epidermal growth factor receptor in breast cancer.* Breast Cancer Research and Treatment, 2012. **136**(2): p. 331-345.
38. Falahi, F., et al., *Caspase-9 suppresses metastatic behavior of MDA-MB-231 cells in an adaptive organoid model.* Scientific Reports, 2024. **14**(1): p. 15116.

Chapter 3

Results and Discussion (Part III)

The outcome of this part:

1. Published in RSC Nanoscale: '*Self-assembled Amino-based copolymer Nanoparticles for Wound Healing and tissue regeneration: structure studied through Molecular Dynamic Simulation, 2025, Advance Article***'**

2. Filled an Indian Patent: '*A plurality of self-assembled copolymer nanoparticles and a method of synthesis thereof*". Patent Application no.: 202511043769, Dated: 6th May 2025**'**

Chapter 3: Part-III

Self-assembled Amino acid based copolymer Nanoparticles for Wound Healing and tissue regeneration: structure studied through Molecular Dynamic Simulation

3.3.1. Abstract: Amino acid-based block copolymer nanoparticles (NPs) with cross-linkers have garnered growing interest in recent years. However, its' intricate synthesis and purification difficulties, along with stability concerns linked to intermicellar crosslinking, restrict their potential use in healthcare and therapeutic applications. In this line, the present work is aimed to design amphiphilic block copolymer NPs of *N*-acryloyl glycine and *N*-acryloyl-(*L*-phenylalanine methyl ester), i.e., p(NAG-*co*-NAPA)$_{wc}$, without using a cross-linker via miniemulsion free radical polymerization. The self-assembled π-π stacking structural arrangement of copolymer at different temperatures has been confirmed through the molecular dynamics (MD) simulation, which corroborated the structural stability of copolymer NPs at physiological temperature (37ºC). The cell migration results of p(NAG-*co*-NAPA)$_{wc}$ NPs are complementary to the CEMA assay and reveal their tissue regeneration properties. Further, the *in vivo* wound healing study demonstrated that within 13 days of post-treatment, the wound can be healed ~97%, whereas for the control, it is found to be only ~80%. Additionally, the RT-PCR results revealed that p(NAG-*co*-NAPA)$_{wc}$ NPs possess anti-inflammatory and tissue regeneration properties by downregulating TNF-α and IL-1β; and upregulating PECAM-1 and VEGF-A, respectively. In conclusion, this p(NAG-*co*-NAPA)$_{wc}$ NPs are paramount with an extensive clinical potential for the regeneration of acute wounds and can be used for other therapeutic applications.

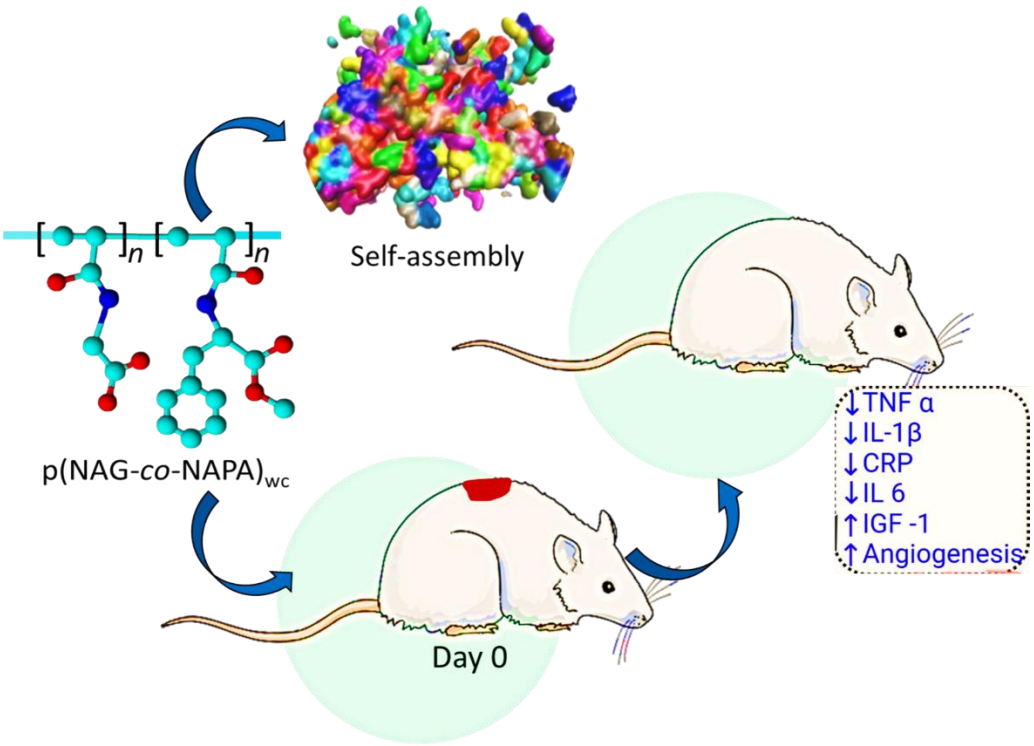

Table of Content Text. *The self-assembled p(NAG-co-NAPA)$_{wc}$ copolymer NPs is formed by physical cross-linking of monomers by forming π-π stacking of benzene rings and confirmed through MD Simulation. Further, this copolymer itself showed effective regenerative property with wound healing capacity within 13 days of post treatment without using any additional drugs, cytokines or cells etc.*

3.3.2. Introduction

Amino acids-based random block copolymers have gained huge attention in biomedical applications due to their unique structures and molecular properties. Block copolymers can be self-assembled into various stable nano-objects based on the conditions applied.[1, 2] They can be conjugated with biomolecules, like drugs or genetic materials or encapsulated through absorption/adsorption or chemical reactions on their surface or in the void space.[3, 4] Their biocompatibility and high bioavailability, have received considerable attention over the other properties.[5] The presence of hydrophilic/hydrophobic functional groups in polymer chains

facilitates the smart attachment of other multiple blocks that subsequently helps in developing surface multi-functionality, high cross-linking, interlocking or branching structure, excellent solubility and symmetric effect. Further, the degradation of their secondary bonds causes pore formation, which is influenced by varying temperature, humidity, solvent, pH.[6]

Self-assembly, hydrothermal synthesis, phase separation, reversed atom transfer radical polymerization, and mini/macro emulsion radical polymerizations are often followed to synthesize polymer NPs. Cross-linkers play a major role in minimizing premature disintegration and providing prolonged circulation time with controlled release of biomolecules.[7, 8] Polymeric NPs with chemically bonded cross-linkers are more stable in high dilutions due to their complex interconnected network. However, they show poor response to any external stimuli and self-healing. Excessive use of cross-linkers makes the polymeric particle rigid and can cause severe toxicity to organs.[9] Further, cross-linkers are highly chemically active and tend to bind with the endothelial cells, body proteins, metal ions, enzymes and lipids.[10, 11] Major challenges lie with the cross-linkers that they can hinder the systematic cellular activities.[12] Due to all these limitations, a series of chemically synthesized covalently cross-linked NPs are restricted for clinical trials.[13] On the other hand, non-covalently cross-linked polymeric NPs are often favoured due to their dynamic evolution and ease of preparation.[14, 15] The stability of non-covalent cross-linked NPs arises due to hydrogen bonds, dipole-dipole interactions, π-π stacking, coordination complexing and hydrophilic or hydrophilic interactions.[16] Double hydrophilic block copolymer of PEG-*b*-PNIPAM were synthesized following RAFT polymerization based on hydrogen bonds.[17] Similarly, phenylboronic acid-modified-PEG-*b*-P(Asp-co-AspPBA) was synthesized through the ROP approach to encapsulate insulin from the attack of external proteases, which was stabilized by hydrophobic interactions.[18] However, in both the cases the presence of PNIPAM

limits their extensive uses in therapy. Compared to all other secondary interactions, π-π stacking provided more stability to the polymeric NPs despite the presence of weak interaction. The π-π stacking is a spatial arrangement of phenyl rings that usually exists in between two molecules deficient or abundant with electrons. The π-π stacking-based polymer micelles showed improved loading and delivery of hydrophobic drugs containing aromatic groups to tumors and a many-fold decrease in CMC.[19] The self-assembled polymeric NPs supported by physical cross-linkers are often reversible and dynamic.[20] To enhance the noncovalent interactions and higher stability, self-assembled polymeric NPs can be composed of both hydrophilic and hydrophobic units.[21] It can be noted that the non-covalently cross-linked self-assembled amino acid-based block copolymers is still to be explored with their therapeutic applications.

In the above line, the small size of the 'NAG' unit and the presence of a phenyl ring in the 'NAPA' unit motivated us to design a random di-block copolymer of *N*-acryloyl glycine (NAG) and *N*-acryloyl-(*L*-phenylalanine methyl ester) (NAPA), p(NAG-*co*-NAPA)$_{wc}$ via non-covalent cross-linking for biomedical applications. The self-assembly nature of the polymer chains could form the NPs without using additional crosslinkers. Considering this, the self-assembled nature of NAPA-NAG at different temperatures has been expored through the molecular dynamic (MD) simulation. The atomistically modelled p(NAG-*co*-NAPA)$_{wc}$ are allowed to reveal their internal properties using MD simulations. 500 dimer units of NAPA-NAG (as obtained from MALDI-ToF results) have been inserted randomly and solvated with water within an orthogonal periodic box and allowed to evolve for 100 ns. The effect of the temperature on the molecular morphology of dimers while forming self-assembled copolymer NPs has been studied in detail. Through the MD simulation, we further have delved into the analysis of the structure of the agglomerates at different temperatures through analysis of the radial distribution functions between critical pairs. Further,

how the interconnected network-like molecular morphology are formed that also has been predicted in the presence of carboxylic and amide groups that could interact with water and help to stabilize the self-assembled polymeric nanostructures by electrostatic interactions. It can be noted that the exposure of these groups present on the surface of NPs can also be ensured by surface potential. Hence, the MD simulation study has been employed to ensure the colloidal stability of such copolymer NPs.

Additionally, NAG and NAPA monomers are highly soluble in organic solvents and their copolymers are well known for their wide applications in healthcare as therapeutics.[22, 23] Therefore, the hemocompatibility and cytocompatibility of p(NAG-*co*-NAPA)$_{wc}$ NPs have been studied against rat RBCs and L929 (mouse fibroblast), respectively and their potential use in wound healing has been investigated through the scratch wound assay and CEMA assay. The present study further investigated the irritation and sensitization, levels of pro-inflammatory cytokines and relative folds change in gene expressions of p(NAG-*co*-NAPA)$_{wc}$ nanoformulation in rat based *in vivo* wound healing model with Rats.

3.3.3. Experimental

3.3.3.1. Materials

The chemicals and cell lines used for this work has been listed in Chapter 2 (Page No. 52-52, Section 2.2).

3.3.3.2. Synthesis of NAG and NAPA monomers and p(NAG-*co*-NAPA)$_{wc}$ block copolymer NPs

3.3.3.2.1. Synthesis of NAG and NAPA monomers

The synthesis procedure of NAG and NAPA monomers are given in Methodologies section of Chapter 2 (Page No. 53-55, Section 2.3.1.1. and 2.3.1.2.).

3.3.3.2.2. Synthesis of p(NAG-*co*-NAPA)$_{wc}$ block copolymer NPs

A detailed synthesis procedure of p(NAG-*co*-NAPA)$_{wc}$ block copolymer NPs is described in the Methodologies section of Chapter 2 (Page No. 56, Section 2.3.1.5.).

3.3.3.3. Characterization of NAG, NAPA, and p(NAG-*co*-NAPA)$_{wc}$ NPs

The characterization details are given in Methodologies section of Chapter 2 (Page No. 57, Section 2.3.2.).

3.3.3.4. Colloidal Stability and Morphological Evaluation

The colloidal stability and morphology study details are given in Methodologies section of Chapter 2 (Page No. 58-59, Section 2.3.3.).

3.3.3.5. CMC Determination

A complete procedure for the CMC determination of p(NAG-*co*-NAPA)$_{wc}$ NPs (1000µg/mL to 0.488µg/mL) are given in Methodologies section of Chapter 2 (Page No. 58-59, Section 2.3.1.1.).

3.3.3.6. Molecular Dynamics Simulation

The complete method followed for MD simulation is briefly described in the Methodologies section of Chapter 2 (Page No. 61-62, Section 2.3.5.3.).

3.3.3.7. *In vitro* cell viability study through MTT assay

The procedure followed for the cell viability of the p(NAG-*co*-NAPA)$_{wc}$ NPs (1000µg/mL to 7.9 µg/mL) with L929 cells is described in the Methodologies section of Chapter 2 .

3.3.3.8. Hemolysis Study

The procedure followed for the Hemolysis study of p(NAG-*co*- NAPA)$_{wc}$ NPs (500µg/mL to 7.8125 µg/mL) is described in the Methodologies section of Chapter 2.

3.3.3.9. *In vitro* Wound scratch assay

The procedure followed for wound scratch assay for p(NAG-*co*-NAPA)$_{wc}$ NPs (250µg/mL to 62.5 µg/mL) with L929 cells is described in the Methodologies section of Chapter 2.

3.3.3.10. Chicken Embryo Membrane assay (CEMA)

The procedure followed for CEMA assay for p(NAG-*co*-NAPA)$_{wc}$ NPs with 250, 125 and 62.5µg doses is described in the Methodologies section of the Chapter 2 (Page No. 73-74, Section 2.3.8.).

3.3.3.11. Development of p(NAG-*co*-NAPA)$_{wc}$ nanoformultion and macroscopic evaluation

The preparation method of p(NAG-*co*-NAPA)$_{wc}$ nanoformulation is described in the Methodologies section of the Chapter 2 (Page No. 56-57, Section 2.3.1.6.). The nanoformulation

was further used for macroscopic qualitative assessment. The parameters considered for macroscopic evaluation are given in **Table S3.3.3**.

3.3.3.12. Biological Evaluation of p(NAG-*co*-NAPA)$_{wc}$ nanoformulation

3.3.3.12.1. Ethical Approval

All information related to animal ethical approval is given in the Methodologies section of Chapter 2 (Page No. 74, Section 2.3.9.1.).

3.3.3.12.2. *In vivo* skin irritation and sensitization.

The method followed for skin irritation and sensitization test of p(NAG-*co*-NAPA)$_{wc}$ nanoformulation is described in the Methods section of Chapter 2 (Page No. 75, Section 2.3.9.3.).

3.3.3.12.3. *In vivo* wound healing

The steps followed for the treatment efficiency of p(NAG-*co*-NAPA)$_{wc}$ nanoformulation for wound healing is described in the Methods section of Chapter 2 (Page No. 75-76, Section 2.3.9.4.).

3.3.3.12.4. Study of histology and immunochemical assay

The procedure followed to study the histology and immunochemical analysis is described briefly in the Methodologies section of Chapter 2 (Page No. 76, Section 2.3.9.5. and 2.3.9.6.).

3.3.3.12.5. Reverse transcription and polymerase chain reaction (RT-PCR)

The procedure followed for the RT-PCR study of tissue samples is described in the Methodologies section of Chapter 2 (Page No. 76-77, Section 2.3.9.7.).

3.3.3.13. Statistical Significance

Statistics applied on this work is described in Methods section of Chapter 2 Page No. 78, Section 2.4.).

3.3.4. Results and Discussion

3.3.4.1. Synthesis and Characterization of monomers (NAG and NAPA) and random block copolymers NPs (p(NAG-*co*-NAPA)$_{wc}$)

The p(NAG-*co*-NAPA)$_{wc}$ was synthesized in two different steps. The first step was the synthesis of monomers (NAG and NAPA) (**Scheme 3.3.1 (Step-1)**) and followed by the synthesis of copolymer NPs (**Scheme 3.3.1 (Step-2)**). The monomer synthesis was carried out using the Schotten-Baumann reaction, where an amine group of amino acids react with acryloyl chloride in an alkaline medium to form an amide bond.[3, 23] The characteristic bands appeared in FTIR and NMR (^{1}H and ^{13}C) for both the monomers are shown in **Figure S3.1.1** to **S3.1.3**. For the synthesis of copolymer p(NAG-*co*-NAPA)$_{wc}$ NPs, free radical mini-emulsion polymerization method was followed as previously reported synthesis method (**Scheme 3.3.1, step-3)**) with slight modification i.e.; avoided the use of cross linker (divinylbenzene).[3] In the p(NAG-*co*-NAPA)$_{wc}$ NPs synthesis procedure, hexadecane (HD) was used as a co-stabilizer to increase the stability of the droplets formed in the emulsion process to prevent coagulation of the particles. Both the monomers were dispersed in the oil phase (toluene) and monomer droplets were formed. The radical initiator AIBN allows the initiation of the polymerization reaction at 65-75°C within the oil/monomer droplet and at the interface of oil/monomer droplets and the aqueous phase. The oily core surrounded by a thin polymeric membrane was stabilized by cross-linking the monomer droplets with NAG which can generate pores in the NPs. The NAG to NAPA wt% ratio was maintained constant (i.e. 50:50)

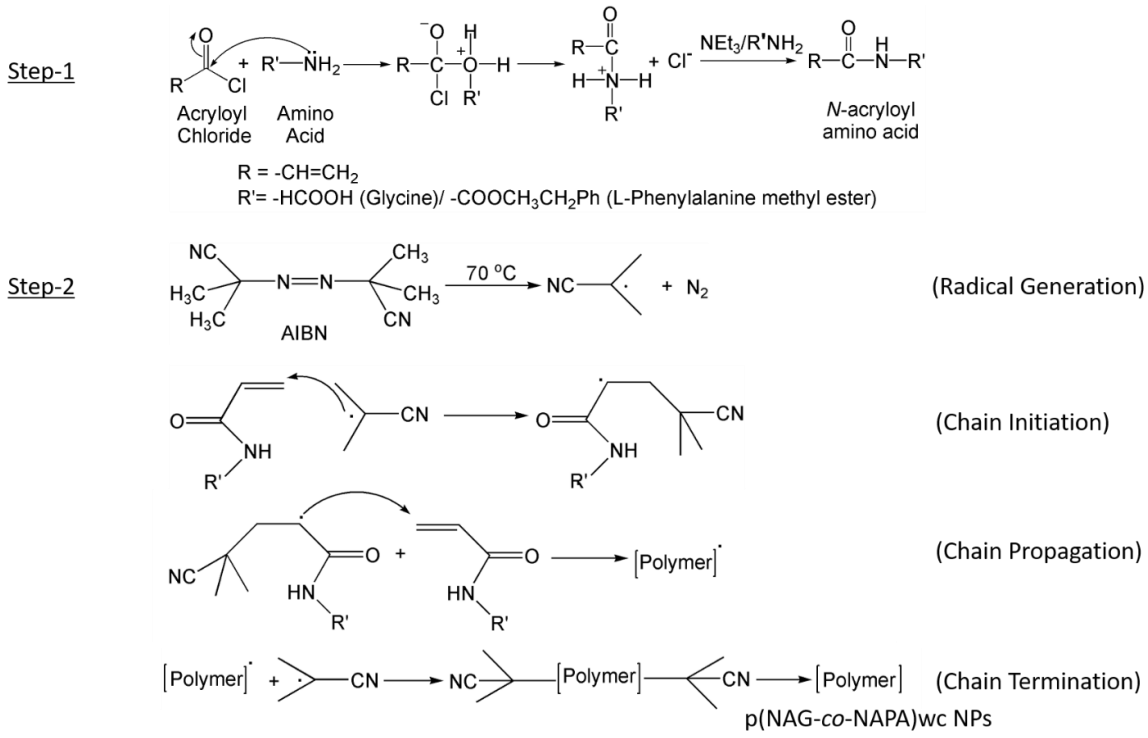

Scheme 3.3.1. *Schematic represents the mechanism involved in the synthesis of NAG (Step-1), NAPA (Step-1) and p(NAG-co-NAPA)$_{wc}$ NPs (Step-2).*

throughout the reaction process. SDS was used as an emulsifier. NPs synthesis without SDS causes decrease in stability and forms aggregates during synthesis. The mechanism lying behind this copolymer synthesis is simple and straightforward. In brief: at first, AIBN initiates the reaction by attacking to hydrogen attached to terminal sp^2 hybridized primary carbon of NAG and NAPA and forms radical ions of both monomers. Then these radicals propagate the chain and eventually the chain undergoes termination, where different growing chains meet 'head-to-head' by forming a π-bond (**Scheme 2**). The copolymer p(NAG-*co*-NAPA)$_{wc}$ formed are amphiphilic in nature, i.e. carboxylic acid group (-COOH) in NAG and one phenyl rings present in NAPA provide hydrophilic and hydrophobic nature to the whole system, respectively. They form a self-assembled structure by moving phenyl rings towards the core of the micelle and carboxylic groups towards the outer side of the micelle. This arrangement of phenyl rings is facilitated by the electrostatic

intramolecular π-π stacking among phenyl groups as reported by Hunter and Sanders in 1990.[24] Thus, this arrangement helps in generating a network like copolymer without using any cross-linker and it promotes to stabilization of the NPs through the molecular packing.[25]

Further, chemical functionalities of p(NAG-*co*-NAPA)$_{wc}$ NPs are confirmed through ^{1}H NMR, ^{13}C NMR and FTIR, and the molecular weight has been estimated through the MALDI-ToF. The position and number of hydrogen atoms present in p(NAG-*co*-NAPA)$_{wc}$ NPs are confirmed through ^{1}H and ^{13}C NMR. The important bands are designated as follows: ^{1}H NMR: δ = 8.15 (1H, d, (secondary amine of NAG monomer)), 7.25 (1H, d, (secondary amine of NAPA monomer)), 7.15 (5H, m, aromatic H), 4.02 (3H, t, alkoxide), 7.05 (-C (=O) N) cis and 5.60 (-C (=O) N) trans, 3.96-2.37 (1H, m, (-CH_2 adjacent to amide of NAG monomer)), 3.21-2.29 (1H, m, (-CH_2 adjacent to amide of NAPA monomer)) and 2.51 (1H, dd, J= 11.3, 9.5) (**Figure 3.3.1(a)**), ^{13}C NMR: disappearance of all the bands for monomers and only one band at δ ranging from 40.33 to 39.32 shows the splitting of 2° alkane (**Figure S3.3.1**) and FTIR (KBr), ν (in cm^{-1})= 3328 (secondary -NH, s), 3020 (aromatic –CH, s), 2925 and 2863 (alkane –CH, s), 1726 (ester C=O, s), 1649 (-NH-C=O, s), and 739 (aromatic –CH, b) (**Figure 3.3.1(b)**). UV-Vis spectra confirms the formation of p(NAG-*co*-NAPA)$_{wc}$ NPs with the absorption bands appearing at 220nm and 258nm, corresponding to π-π* and n- π* transitions, respectively (**Figure S3.3.2**). The π-π* transition confirms the presence of the carbonyl group, while n- π* transition confirms the presence of double bonds in p(NAG-*co*-NAPA)$_{wc}$ NPs. MALDI-ToF analysis confirms the molecular weight of the copolymers ranging from 377Da to 493Da with an intense band at 400.02Da, which depicts that possibly most of the fragments are nearly equal to the summation of individual molecular mass of one NAG and one NAPA units. Therefore, the highest intense fragments consist of a dimer of NAG and NAPA. The first highest fragment is obtained at 406.31 (*m/z*), i.e. number average molecular

weight ($\bar{M}_n$), and 400.02 (*m/z*), i.e., weight average molecular weight ($\bar{M}_w$), with a PDI of 0.99. The difference between two adjacent peaks varies from 13Da to 45Da, which further confirms the formation of random p(NAG-*co*-NAPA)$_{wc}$ copolymer NPs with a heterogeneous population in the system (**Figure S3.3.3**). Therefore, all these chemical functionalities-based observations confirm the successful synthesis of p(NAG-*co*-NAPA)$_{wc}$ NPs.

The thermal stability of p(NAG-*co*-NAPA)$_{wc}$ NPs exhibited which five steps weight loss ranging from 130°C to 356°C (**Figure 3.3.1(c)**). The thermal stability of the NPs at physiological temperature (37°C) is crucial for its use in therapeutic applications. The five steps weight loss (%) are as follows: (I) 45-108°C (3%), (II) 108-158°C (3%), (III) 158-240°C (13%), (IV) 240-310°C (21%), and (V) 310-390°C (30%) are observed. Stage I is observed due to the loss of free moisture and stages II, III, IV and V are observed due to the thermal degradation of polymer chains. It can be noted that beyond 390°C, the leftover materials are the carbon residues only. The DTGA plot of p(NAG-*co*-NAPA)$_{wc}$ NPs (**Figure 3.3.1(c)**) provides an idea of degradation temperatures temperatures corresponding to each weight loss step. The maximum rates of degradation are found to be at 130 °C, 178 °C, 273 °C and 356 °C. Degradation at lower temperature is observed due to the presence of low molecular weight of p(NAG-*co*-NAPA)$_{wc}$ NPs .This quite low degradation temperature is observed, may be due to the low molecular weight p(NAG-*co*-NAPA)$_{wc}$ NPs. Furthermore, to evaluate the thermal phase transition, the DSC of p(NAG-*co*-NAPA)$_{wc}$ NPs was conducted from RT to 350 °C (**Figure 3.3.1(d)**). The glass transition temperature (T_g) is observed at 47 °C with an endothermic peak (endo down). An additional endothermic peak is observed at 305 °C, due to the decomposition of p(NAG-*co*-NAPA)$_{wc}$ NPs. From XRD, it is confirmed that the p(NAG-*co*-NAPA)$_{wc}$ NPs are amorphous in nature, which is matching well with the diffused ring of SAED patterns obtained from HR-TEM image of p(NAG-*co*-NAPA)$_{wc}$ NPs (**Figure 3.3.1(e)**

and inset image) represented in subsequent section (**Figure 3.3.2(b)**). The amorphous nature of p(NAG-*co*-NAPA)$_{wc}$ NPs helps in improving the NP's apparent bioavailability.[26, 27]

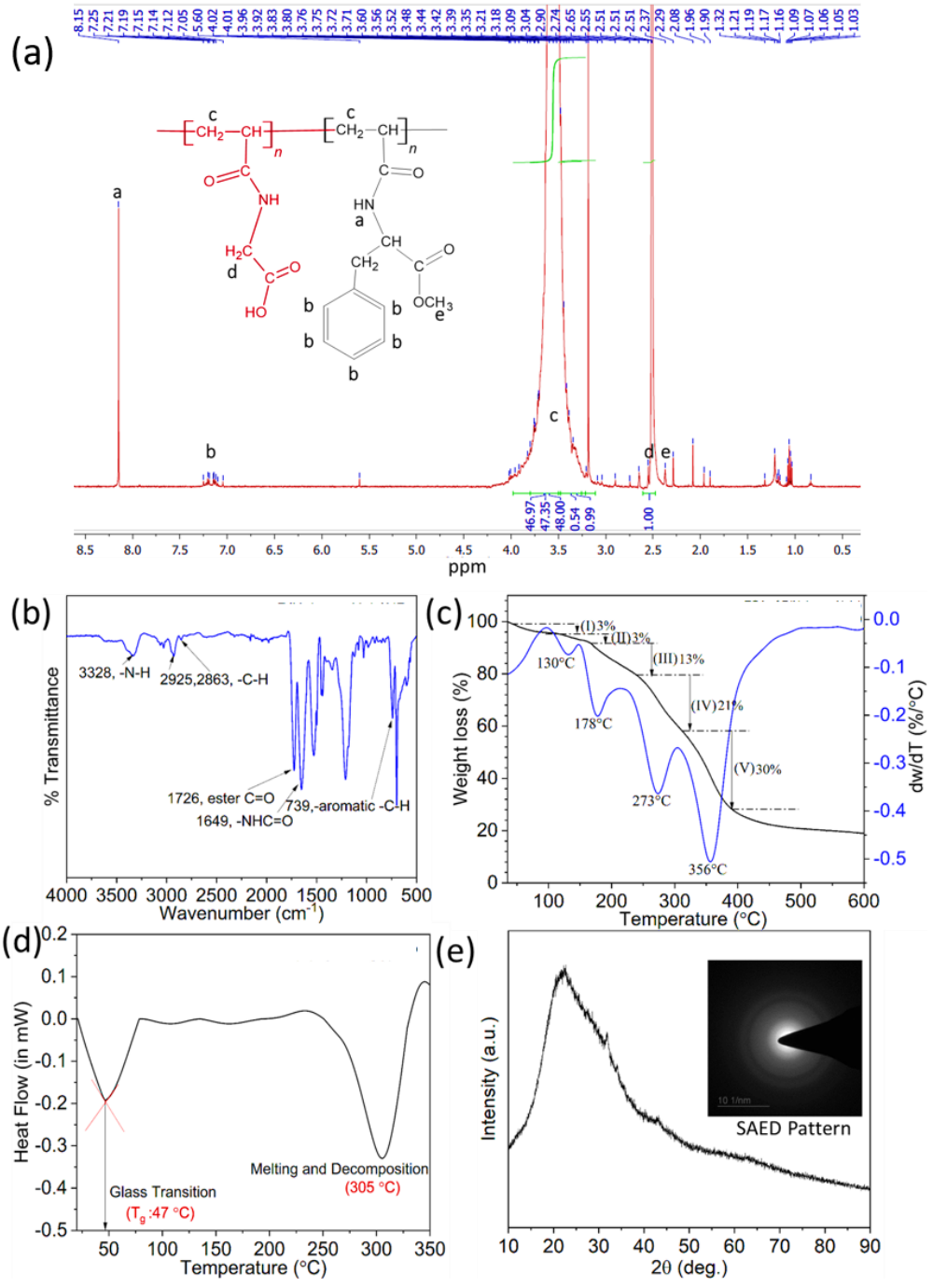

Figure 3.3.1. *Physicochemical properties of p(NAG-co-NAPA)$_{wc}$ NPs. Fig. (a) ^{1}H NMR spectra, (b) FTIR spectra, (c) TGA and DTGA thermograms, (d) DSC thermogram and (e) XRD pattern of p(NAG-co-NAPA)$_{wc}$ NPs. Inset image of (e) is the SAED pattern for p(NAG-co-NAPA)$_{wc}$ NPs.*

3.3.4.2. Morphology and colloidal stability of p(NAG-*co*-NAPA)$_{wc}$ NPs

The shape, size and morphology of the p(NAG-*co*-NAPA)$_{wc}$ NPs were investigated by using FESEM, HR-TEM, and AFM analysis (**Figure 3.3.2**). The microscopic images (**Figure 3.3.2(a)**, (b) and (d)) revealed that p(NAG-*co*-NAPA)$_{wc}$ NPs are spherical in nature with diameter ranging from 120-400nm. **Figure 3.3.2(e)** represents the particle size distribution (120-200nm) obtained from FESEM images. From HR-TEM images (**Figure 3.3.2(b)**), the size was calculated to be 200-220nm in diameter. From AFM, the size is calculated to be 200-300nm in diameter. The variation in the sizes of p(NAG-*co*-NAPA)$_{wc}$ NPs obtained from different microscopy results is due to the different modes of the experimental procedure. However, the dark core-like structure as observed in **Figure 3.3.2(b)**, is due to the self-assembly nature of polymer chains of p(NAG-*co*-NAPA)$_{wc}$ NPs as shown in **Scheme 3.3.2**. This self-assembly occurs due to the presence of a hydrophilic carboxylic group on the surface of the particle by forming corona and hydrophobic phenyl rings present inside the shell. The hydrophobic rings are arranged in T-shaped π stacking (**Scheme 3.3.2**). MD simulation study has been performed to confirm the self-assembly structure of p(NAG-*co*-NAPA)$_{wc}$ polymer chains in NPs, which has been discussed in the subsequent section. Further, the colloidal stability of the p(NAG-*co*-NAPA)$_{wc}$ NPs was checked by DLS in MilliQ at RT (**Figure 3.3.2(c)**) and the hydrodynamic diameter is calculated from size distribution by intensity plot and Z-average is found to be 389nm with 0.171 PDI. Further, volume distribution by intensity report and combined plot of intensity vs size are shown in **Figure S3.3.4**. The increase in size of p(NAG-*co*-NAPA)$_{wc}$ NPs is observed due to the entrapment of water molecules in the copolymers network and possible swelling of the NPs.

The zeta potential was calculated to be -50.94mV, which comprises colloidal stability of p(NAG-*co*-NAPA)$_{wc}$ NPs (**Figure 3.3.2(f)**). The optical properties of p(NAG-*co*-NAPA)$_{wc}$ NPs

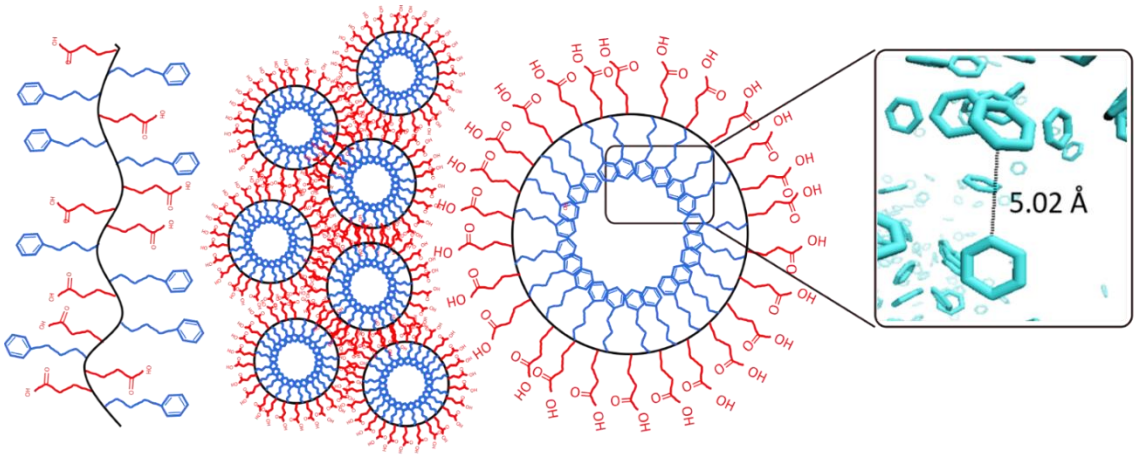

Scheme 3.3.2. *Schematic representation of p(NAG-co-NAPA)$_{wc}$ NPs forming self-assembled nanostructure via physical cross-linking induced by π-π stacking.*

was confirmed through the CD spectroscopy as mentioned in the experimental section with concentrations of 1000 to 125µg/mL at 25ºC. In all concentrations, a distinct narrow CD band appeared at λ_{max} = (230 ± 5)nm (**Figure 3.3.2(g)**) due to the presence of optically active NAPA monomer in the copolymer NPs.[28] As reported earlier, with increase in the concentration of NPs (i.e.; subsequently increase in the concentration of NAPA monomer) the intensity of the CD spectra increases. From **Figure 3.3.2(g)** it is evident that as the positive and negative bands are separated from each other comprising the formation of a self-assembled structure in the medium.[29] Further, by fixing the p(NAG-*co*-NAPA)$_{wc}$ NP's concentration with 125µg/mL, CD spectra were recorded at three different temperatures (25°C, 37°C and 42°C) (**Figure 3.3.2(h)**). Similar CD spectra is obtained for each with a λ_{max} = 218nm, which comprises the existence of secondary structure of the polymer chains in the copolymer NPs. Using JASCO software, it is also identified that the copolymer consists of ~100% turn-type of secondary arrangements formed in the polymeric particles, with a few numbers of small loops consisting of hydrogen bonds (**Figure**

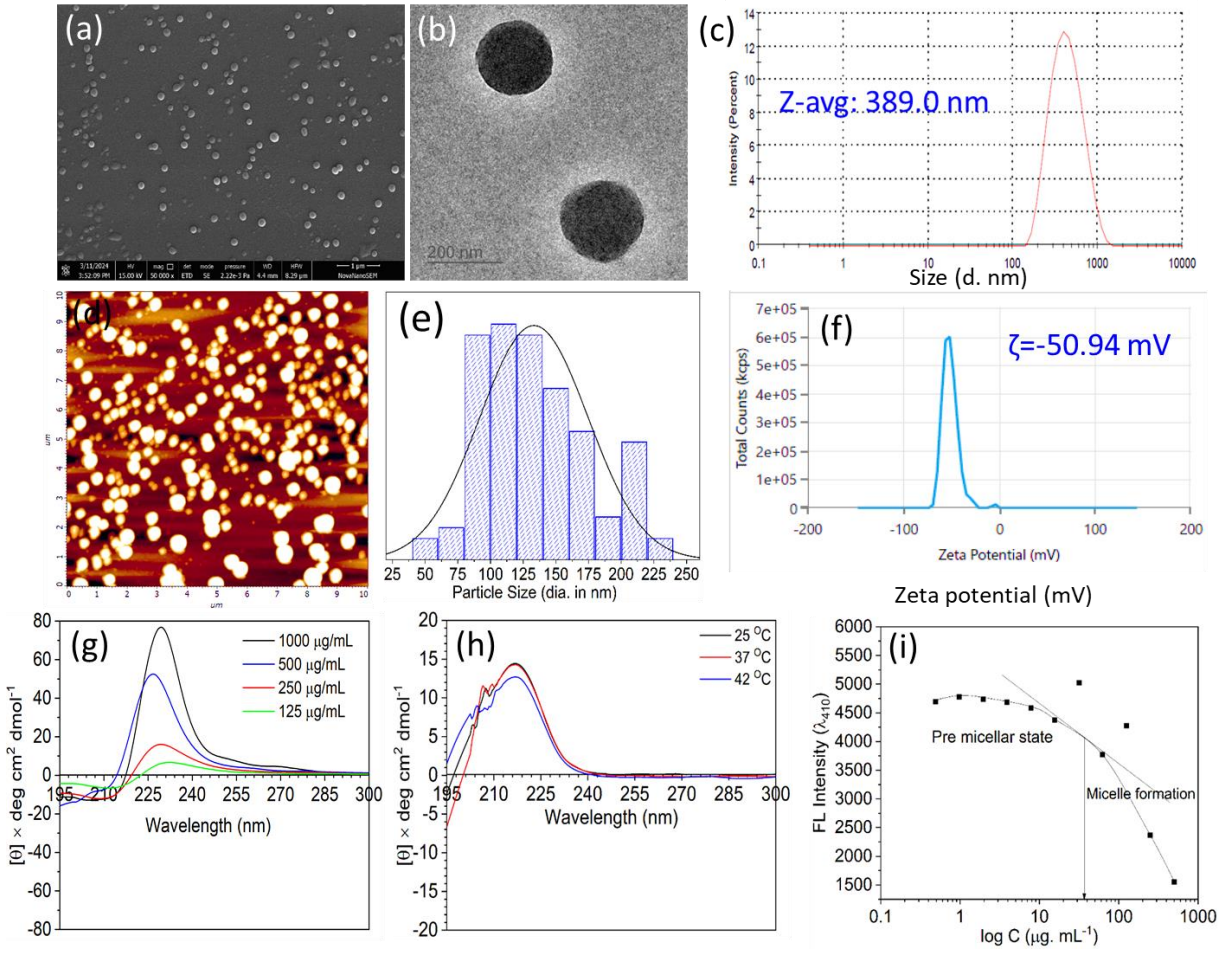

Figure 3.3.2. *Size, shape, morphology and colloidal stability of p(NAG-co-NAPA)$_{wc}$ NPs. Fig. (a) FESEM, (b) HRTEM image (scale bar: 200 nm), (c) DLS, (d) AFM, (e) particle size distribution obtained from Fig. 2 (a), (f) Zeta potential, (g) and (h) CD spectra of p(NAG-co-NAPA)$_{wc}$ NPs at different concentrations and three different temperatures, respectively and (i) CMC of p(NAG-co-NAPA)$_{wc}$ NPs.*

S3.3.5). All these results also assist the formation of fibrils like of structural arrangement in the copolymer NPs.[30] Subsequently, these secondary structures can help in understanding the interactions between NPs and drug molecules, and further this can be helpful in designing a drug or vaccine with desired stability, shelf-life and efficacy of treatment. The CMC is an important parameter in colloid chemistry, which denotes the minimum concentration needed to form a self-

assembled structure of NPs in the liquid medium. The magnitude of the CMC is closely related to the size of the NPs and hydrophobic block present in the system. It can be noted that a block copolymer is biocompatible and a precise ratio should be maintained between hydrophobic and hydrophilic units for its effective use in therapy.[31, 32] Herein, the CMC for the p(NAG-*co*-NAPA)$_{wc}$ NPs was calculated to be 1.56µg/mL (**Figure 3.3.2(i)**). This low extent of CMC demonstrated that a good hydrophobic to hydrophilic ratio is maintained in the system with increase in the extent of π-π stacking due to the physical cross-linking. The MD simulation results also demonstrate that the benzene rings are present in close proximity with a distance of 5.02Å (**Scheme 3.3.2**). This leads to the formation of aggregates of p(NAG-*co*-NAPA)$_{wc}$ NPs in the particular medium or solvent. Furthermore, such systems with low CMC can tolerate the high degree of dilution, i.e., bloodstream dilution and makes the NPs biologically and mechanically more stable. It can be further elucidated that the physical cross-linking can reform the NPs even after disintegration of the self-assembly structure, which is known as self-healing of NPs.[33, 34]

3.3.4.3. Molecular aggregation of p(NAG-*co*-NAPA)$_{wc}$ NPs

Molecular dynamics simulation of atomistically modelled p(NAG-*co*-NAPA)$_{wc}$ molecules revealed the molecular aggregation in the presence of water. 500 dimer units of NAG-*co*-NAPA were randomly inserted within an orthogonal periodic box followed by solvation with water. The aqueous solution of NAG-NAPA, having a concentration of 0.2 g/mL, was allowed to evolve for 100ns. The concentration of the dimer in the simulations is much higher compared to the concentration range used in the experiments (7.8-1000 µg/mL). To prepare the computational systems having con-centration in this range, the number of solvent molecules in the simulation box would be very large (more than 200 times the pre-sent), and the computation work would be extremely expensive and time-consuming.

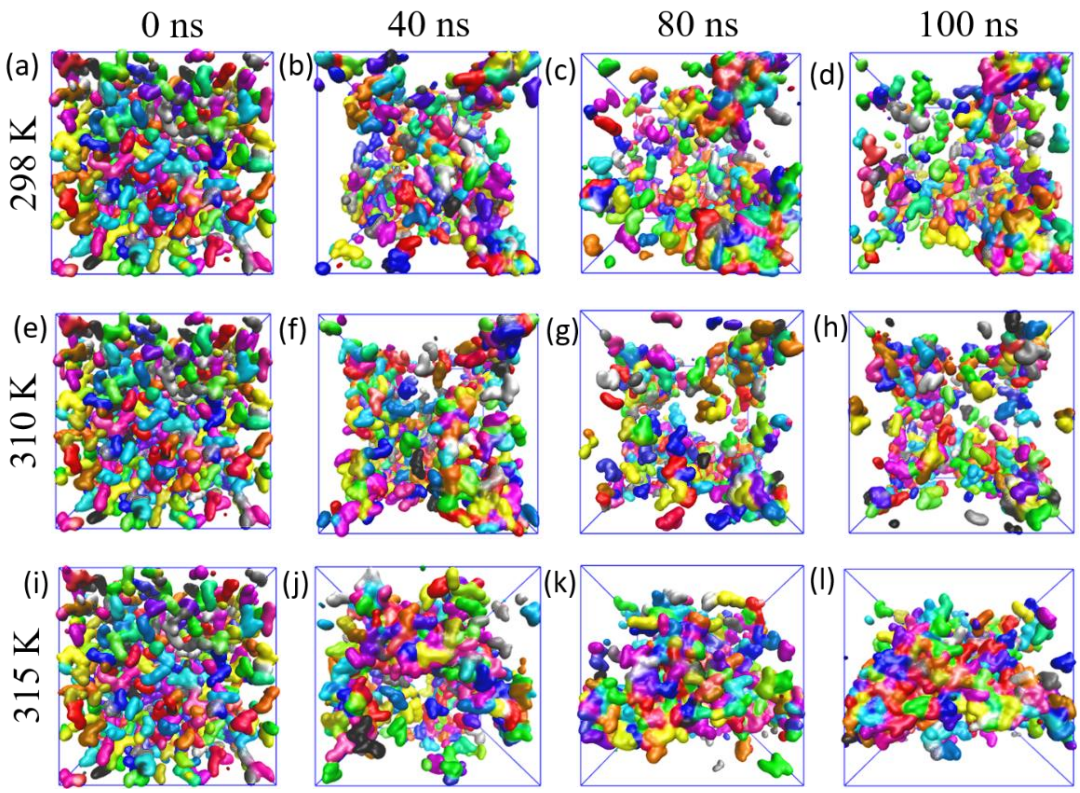

Figure 3.3.3. *Show the structural evolution of NAPA-NAG at three different temperatures (298K, 310K, and 315K) at 0, 40, 80 and 100ns. The dimers are represented as QuickSurf using VMD and other components of the solutions were omitted for visual clarity.*

Figure 3 shows the evolution of dimer molecules in solution to reveal their organization and their structural properties at three different temperatures, such as 298 K, 310 K and 315 K. The initial configurations shown in **Figure 3 (a, e, and i)** indicated that the di-mer molecules (different colours for different molecules) are ran-domly distributed in the water medium (not shown for clarity). From the snapshots in the top row of **Figure 3**, it is evident that the dimer molecules are forming interconnected aggregates (indicated by continuous surfaces with multiple colors) spreading over the whole simulation box. Additionally, **Figures 3(c)** and **3(d)** indicate that the interconnected aggregates evolved their structure with time. How-ever, the interconnected aggregates are building up the walls of the porous structure as observed in experiments. From

Figure 3(e-f), it is revealed that the NAG-co-NAPA dimer molecules are also forming interconnected structures at 25 °C (298 K), which further manifests the porous structure of the NPs obtained in the experi-ments. As the temperature rises to 37 °C (310 K), the number of interconnected fragments decreases (**Figure 3 (g-h)**; hence, the porosity in the structure decreases. However, this extent of change is negligible. At 42 °C (315 K) at 40 ns, a distinct agglomeration is observed (**Figure 3 (j)** compared to the 25 °C and 37 °C (**Figure 3(b)** and **3(f)**), respectively). However, at 80 ns, a deviation is observed with respect to the previous two cases. This phenomenon is observed as a larger number of agglomerated units were present (**Figure 3(k)**) which are surrounded by water molecules. This would lead to the formation of structure with less porosity. However, till 100ns (**Figure 3.3.3(l)**) the structure remained alike. This revealed that there is an impact of the temperature on the molecular morphology of dimers while forming NPs. Further, the interconnected network-like molecular morphology of NPs also indicated that the hydrophilic groups such as carboxylic and amide are interacting with water molecules strongly prefer to be exposed to water. These molecular arrangements help in stabilizing the structure of the NPs. The presence of these groups at the surface of NPs are with negative zeta potential (**Figure 3.3.2(f)**) that ensures the colloidal stability of designed NPs in aqueous medium. Additionally, to establish a better correlation, the aggregation behavior of hydrophobic phenyl group present in NAPA unit and hydrophilic carboxyl groups present in NAG units after 0, 40 and 80ns of simulation run in three concerned temperatures as shown in **Figure S3.3.7** and **S3.3.8**.

3.3.4.4. Structural Properties of p(NAG-*co*-NAPA)$_{wc}$ Molecular Assembly

We further delved into the analysis of the structures of the agglomerates at different temperatures through analysis of the radial distribution functions between critical pairs of atoms. In **Figure 3.3.4(a-c)**, the RDF between water and carboxylic, phenyl and amine groups are shown,

respectively, at different temperatures. The pair-correlation between the carboxyl groups and the water molecules can be strongly correlated, as indicated by the appearance of the sharp repetitive peaks at regular intervals. However, the local density of the water molecule has not reached to the overall density of the system, comprising the formation of an agglomerated structure (**Figure 3.3.3**). Another interesting aspect to note here is the drop in the peak intensity with temperatures. This observation suggested that the solvation shells gradually become less populated as the temperature rises. The pair correlation between the water and phenyl groups did not pose a sharp peak (**Figure 3.3.4(b)**), indicating the presence of a structured water layer surrounding the phenyl rings due to the electronic cloud of phenyl rings. The pair-correlations gradually increase towards unity, suggesting the formation of an overall agglomerated structure. In the case of this pair, the number of water molecules present around the phenyl rings also have decreased with increase in the temperature of the system. The amide/amine nitrogen atoms, however, showed a stronger affinity with water molecules compared to the phenyl groups as indicated by the appearance of a sharp peak (**Figure 3.3.4(c)**). It is also revealed that the amine groups hold the water molecules at ~2.8Å, which allows the formation of hydrogen bonds with the nitrogen atoms. In this case, the peak height is decreased slightly with increase in the temperature. Further, the coordination numbers for 310K to 315K are found higher in values compared to the temperature range of 298 to 310K, (inset **Figure 3.3.4(c)**). The interplay between hydrophilic and hydrophobic groups have played a key role in the aggregation of copolymers. More specifically, the hydrophobic phenyl groups played a crucial role in agglomeration due to possible π-π stacking. Further, we have calculated the RDF between carbon atoms at the 1 and 4 positions of different phenyl rings, denoted as Ph_{11}, Ph_{14}, and Ph_{44} (**Figure 3.3.4(d)**). In this figure, the comparisons of RDFs between different pairs are shown with different temperatures. The 4-4 pairs correlation showed a stronger

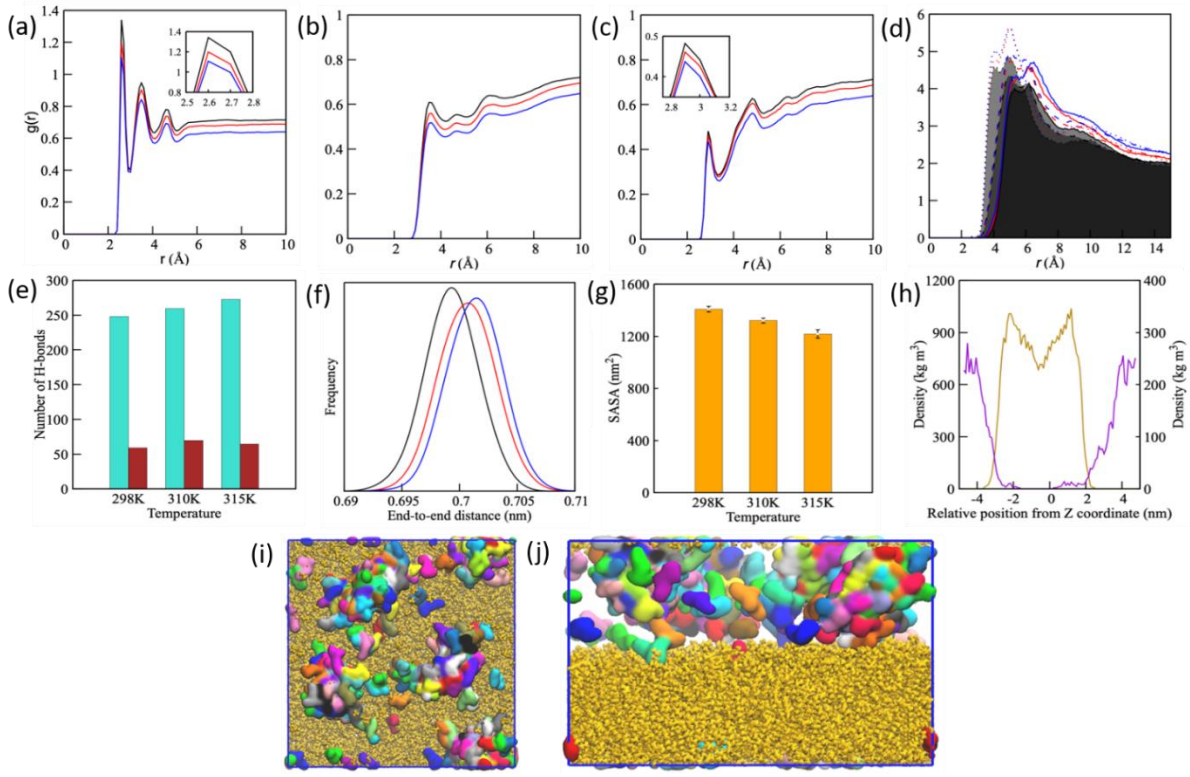

Figure 3.3.4. *The radial distribution function between oxygen atoms in water molecules and (a) the carboxylic groups, (b) phenyl groups, (c) nitrogen atoms in dimers at different temperatures. The black, red and blue lines of figures represented the temperatures, 298, 310 and 315K, respectively. (d) radial distribution functions between phenyl carbon atoms at 1 and 4 positions at different temperatures, respectively, (e) Number of intramolecular hydrogen bonds between –COO and –NH atoms with the total number of hydrogen bonds between copolymer units at different temperatures, (f) distribution of end-to-end distance of the copolymers at different temperatures, (g) Change in SASA of polymers matrix in aqueous solution at different temperatures with the evolution time, (h) density distribution of copolymer and POPC membrane along the direction perpendicular to the membrane surface, and (i-j) side and top views of agglomerates of copolymers in water on POPC membrane at 310K, respectively.*

split of peaks at lower distance, whereas the other pairs exhibited weaker peaks at higher distance. This indicated that the 4-4 interactions are quite stronger and thus played a dominating role in agglomerating the polymer chains. However, the structure is amorphous in nature, as indicated by the absence of any sharp peak. This dominance for Ph_{44} could be due to its readily accessible

position along with the presence of a bulky group with Ph_{11}. Hence, to avoid steric hindrances, close associations of 4-4 pairs are favored across all three temperatures, demonstrating a T-shaped π- π stacking.[35] Furthermore, the histograms of angle distribution at three different temperatures are provided in **Figure S3.3.9**. On the other hand, the 1-1-pair correlation exhibited a broader split peak at a longer distance. Whereas, interestingly the 1-4 pairs showed a cross-over of the RDF of two individual pairs. As the temperature of the system increases, all the RDF peak height increased as well as broadened. This indicates that the amorphous nature of the agglomerates increases with increase in the temperature.

Further, to elucidate the behavior of dimers in the aqueous system, the number of hydrogen bonds play a pivotal role in aggregation between the dimers and water molecules, which was calculated at all temperatures. The average number of hydrogen bonds formed between copolymers are shown in **Figure 3.3.4(e)**. Additionally, the intermolecular hydrogen bonds are formed predominantly. However, the total number of hydrogen bonds formed are approximately five times more than that of the intramolecular hydrogen bonds formed between the carboxylic acid groups and amine groups. The total number of hydrogen bonds increased with the increase in temperature, while the extent of intramolecular bindings decreased. At lower temperatures, due to the presence of a large number of intramolecular hydrogen bonds, a less interconnected hydrogen-bonding network formed that leads to the inclusion of more water molecules in the agglomerates. However, with an increase in temperature, the molecules assembled into a larger network through the formation of hydrogen bonds, allowing the molecules to agglomerate tightly in an elongated manner. Additionally, the number of hydrogen bonds formed between dimers and water molecules is shown in **Figure S3.3.10(a)** at three temperatures, which also further demonstrates that with an increase in temperature, there is a sharp decrease in the number of hydrogen bonds. This decrease

in the extent of hydrogen bonds matches well with the number of contact results as shown in **Figure S3.3.10(b)**. The end-to-end distribution of the copolymers, also quantifies the elongation of the molecules, as shown in **Figure 3.3.4(f)**. As the temperature increases, the end-to-end distribution of peaks is shifted towards the right indicating the formation of a more elongated conformation of the molecules in the agglomerates. Hydrophilicity of the agglomerated structure is a key parameter in utilizing it for therapeutic applications. Thus, we have calculated solvent accessible surface area (SASA) to quantify it (**Figure 3.3.4(g)**), it can be seen that with increase in the temperature, SASA decreases, which supports the hydrophobic nature of the agglomerates. A lower SASA value at 315K hints towards the formation of larger globular aggregates. However, a slightly higher solvent-accessible surface area is available at the physiological temperature (310K). These finding suggest that the higher aggregation occurred at the higher temperatures and subsequently it helps in stabilizing the NPs. Additionally, the biocompatibility of copolymers was assessed through the interactions with the POPC bilayer membrane at 310K. The density distribution of copolymers shown in **Figure 3.3.4(h)**, was calculated around the z-axis of the membrane, showing that copolymer aggregates (**Figure 3.3.4(i)**) have formed bonds to the membrane within 100ns. Further, the dimers formed a close association with the bilayer surface of the membrane as shown in **Figure 3.3.4(j)**.

3.3.4.5. Biocompatibility, Hemocompatibility, Proliferative and migratory behavior of p(NAG-*co*-NAPA)$_{wc}$ NPs through *in vitro* study

Biocompatibility and hemocompatibilty are the major parameters that need to be studied for any biomedical application of copolymer NPs. The fibroblast cells are abundantly present in mammals and we have selected L929 cells to check the biocompatibility of the developed p(NAG-*co*-NAPA)$_{wc}$ NPs. It is noticed that L929 cells treated with p(NAG-*co*-NAPA)$_{wc}$ NPs demonstrated

concentration dependent proliferative behavior and are cytocompatible in nature. Additionally, as the concentration of p(NAG-*co*-NAPA)$_{wc}$ NPs increases, the cell viability (%) steadily increases. However, from 500 to 1000µg/mL, cell viability (%) slowly decreases. This decrease in cell viability (%) is obtained due to high contact inhibition experienced by cells in the respective confined space for a longer period of time (24h). It is worth mentioning that the concentrations of p(NAG-*co*-NAPA)$_{wc}$ NPs taken 7.8125, 15.625, 31.25, 62.5 and 125µg/mL and the cell viability (%) are observed to be 137.1± 2.3, 122.9±2.5, 119.2±1.9, 119.9±1.2 and 119.3±1.4, respectively (**Figure 3.3.5(a)**). These results clearly suggest that the designed p(NAG-*co*-NAPA)$_{wc}$ NPs are biocompatible and can promote the proliferation of L929 cells. Further, hemocompatibilty is also a crucial parameter for nanobiomaterials for its use in therapeutic applications, as the NPs during systemic circulation can cause toxic effects and limit the therapeutic benefits. The copolymer should have hemolysis below 5% to avoid any toxic effect. Thus, the hemolytic activities of p(NAG-*co*-NAPA)$_{wc}$ NPs were studied in both dose and time-dependent manner over a range of 500 to 7.8125µg/mL concentrations at 2 and 8h. Herein, distilled water was considered as a positive control, and pure RBC suspension was considered as a negative control. Although a varied degree of hemolysis (%) was observed at concerned time for all the concentrations taken in this study, the hemolysis value calculated to be below 5% (**Figure 3.3.5(b)**). At 500µg/mL, hemolysis values are observed to be 8.0±1.1 % and 10.1±1.5 % for 2h and 8h, respectively (**Figure 3.3.5(b)**). In conclusion, the p(NAG-*co*-NAPA)$_{wc}$ NPs can be considered as the safe biomaterial, which can be used up to 250µg/mL for various therapeutic applications.

Skin fibroblast cells migration is an important aspect of regenerative medicine or wound healing processes.[36] As the cell proliferative behaviour of p(NAG-*co*-NAPA)$_{wc}$ NPs was studied from the cell viability assay. Further, the pro-migratory effect of p(NAG-*co*-NAPA)$_{wc}$ NPs was

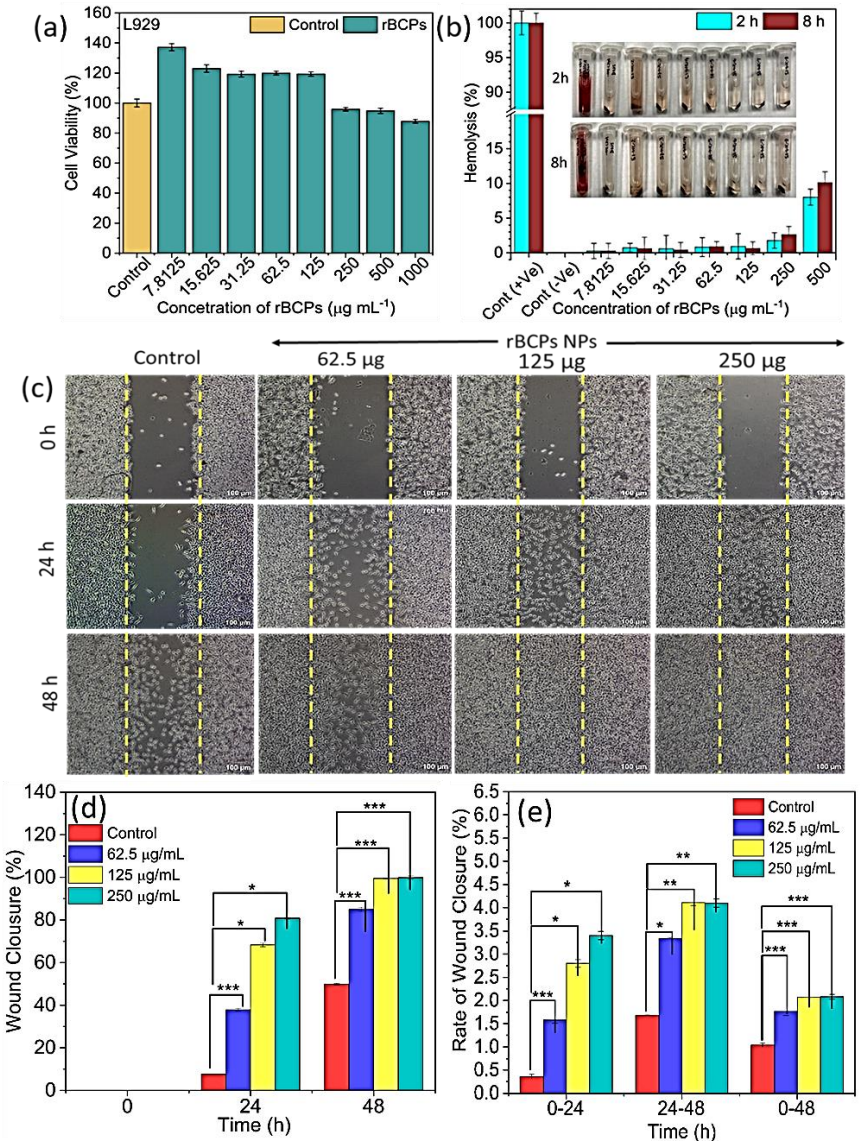

Figure 3.3.5. *Biocompatibility, hemocompatibility and proliferation nature of p(NAG-co-NAPA)$_{wc}$ NPs. Shows (a) cell viability (%), (b) hemolysis (%) of p(NAG-co-NAPA)$_{wc}$ NPs at different concentrations against L929 cells and rat erythrocytes, respectively. The inset image of figure 3.3.5(b) represents the micro-centrifuge tubes showing hemolysis at 2 and 8h. MTT of p(NAG-co-NAPA)$_{wc}$ NPs shows no significant difference for both L929 and hemolysis (%) of NPs are non-significant with respect to the control (-ve) and significant (*) with respect to the control (+ve) for 2 and 8h, respectively. Hemolysis (%) for 500µg/mL is significant (**) with respect to the control (-ve) at 8h. Fig. (c) Represents the microscopic images of the wound scratch assay of p(NAG-co-NAPA)$_{wc}$ at 0, 24 and 48h taken at 10X magnification with a scale bar of 100µm, (d) and (e) Wound closure (%) and Rate of wound closure (%) of L929. rBCPs represents p(NAG-co-NAPA)$_{wc}$ NPs. Data are given as mean ±SD (n=3) (*p ≤ 0.05, **p ≤ 0.05-0.01, ***p ≤ 0.05-0.001 and ns: non-significant).*

checked using *in vitro* wound scratch assay for a period of 0 to 48 h at three different concentrations (62.5 to 250µg/mL). At three different time points, optical microscopic images were acquired as shown in **Figure 3.3.5(c)**. It is observed that p(NAG-*co*-NAPA)$_{wc}$ NPs can efficiently cover the wounds in L929 cells. Furthermore, to quantify the wound closure efficiency (%) and wound closure rate (%), Fiji ImageJ software was used.[37] After 24h of incubation of cells with p(NAG-*co*-NAPA)$_{wc}$ NPs, 37.84±0.06%, 68.32±0.8% and 80.76±0.0009% of scratched area are filled for 62.5, 125 and 250µg/mL, respectively. Whereas for the control 7.55±0.06% scratch is covered (**Figure 3.3.5(d)**). After 48h of incubation, 84.97±0.9%, 99.56±0.3% and 99.94±0.007% scratched area are covered for 62.5, 125 and 250µg/mL, respectively. Whereas for control only 49.86±0.2% scratch is covered (**Figure 3.3.5(d)**). Further, it is noticed that during the initial 24h, over all three concentrations, wound closure rate (%) is quite faster as compared to the next 24h. In case of wound closure rate (%), a similar trend is observed (**Figure 3.3.5(e)**). From 0-24h and 24-48h, the wound closure rate is quite faster as compared to 0-48h. These variations in results are observed due to the contact inhibition and confined space available for the cells to proliferate and migrate. The results obtained from wound scratch assay demonstrated that p(NAG-*co*-NAPA)$_{wc}$ NPs can fill the scratched area by ~10 times more efficiently compared to the control. From both wound closure (%) and rate of wound closure (%) results, it is clearly evident that p(NAG-*co*-NAPA)$_{wc}$ NPs show dose dependent proliferative and migratory efficiency. Furthermore, it is evident that even at a very low concertation of 62.5µg/mL the p(NAG-*co*-NAPA)$_{wc}$ NPs can accelerate the wound healing efficiency.

3.3.4.5. Dose and time dependent angiogenic nature of p(NAG-*co*-NAPA)$_{wc}$ NPs

Angiogenesis plays an important role in the field of wound healing and regenerative medicine. It is a process where the new blood vessels emerge and/or proliferate from an existing blood

vessels.[38] As the results obtained from cell viability study (**Figure 3.3.5(a)**) and wound scratch assay (**Figure 3.3.5(c-e)**) against L929 cells, demonstrated that p(NAG-*co*-NAPA)$_{wc}$ NPs are proliferative in nature. Further chicken embryo membrane assay (CEMA assay) was performed to establish the angiogenic or vascular sprouting nature of p(NAG-*co*-NAPA)$_{wc}$ NPs. For this, three different doses (62.5, 125 and 250 µg) of p(NAG-*co*-NAPA)$_{wc}$ NPs were incubated separately with chick embryos. It is revealed that the presence of p(NAG-*co*-NAPA)$_{wc}$ NPs causes increase in the thickness of blood vessels and length (**Figure 3.3.6(a)**). Further to quantify the angiogenic properties, Explant area, Vessel area, Junction density and Mean-E-lacunarity were calculated asmentioned in the experimental section. Explant area means the overall region where blood vessels are developed. It is observed that compared to the control, at 125 and 250µg doses, very less explant area has been increased. While for 62.5µg dose, ~80% increase is observed at 8h (**Figure 3.3.6(b)**). A similar result is observed in the case of the Vessel area (%). Vessel area means the total surface area of blood vessels occupied in an explant area. Herein, at lower dose, the vessel area is increased up to 180% (at 8h), while for higher dose, it is increased up to 140% (**Figure 3.3.6(c)**). In case of junction density, a decrease in percentage is observed at lower dose, while for higher doses a slight increase in Junction densities is observed (**Figure 3.3.6(d)**). Further, Mean-E-lacunarity (%) was also quantified, which suggests the empty spaces available after the incubation with the material. In the case of 62.5µg dose, the Mean-E-lacunarity (%) is decreased to 69%, whereas for control it is found to be 88% at 8h. However, in application of higher doses such as 125 and 250µg, no such variation in Mean-E-lacunarity (%) is observed (**Figure 3.3.6(e)**). However, based on time points from 0 to 8h, in all considered parameters 62.5µg dose, it is also showing better angiogenic in nature as compared to the other doses. Thus, the results obtained from CEMA assay clearly depicted that p(NAG-*co*-NAPA)$_{wc}$ NPs are showing branching

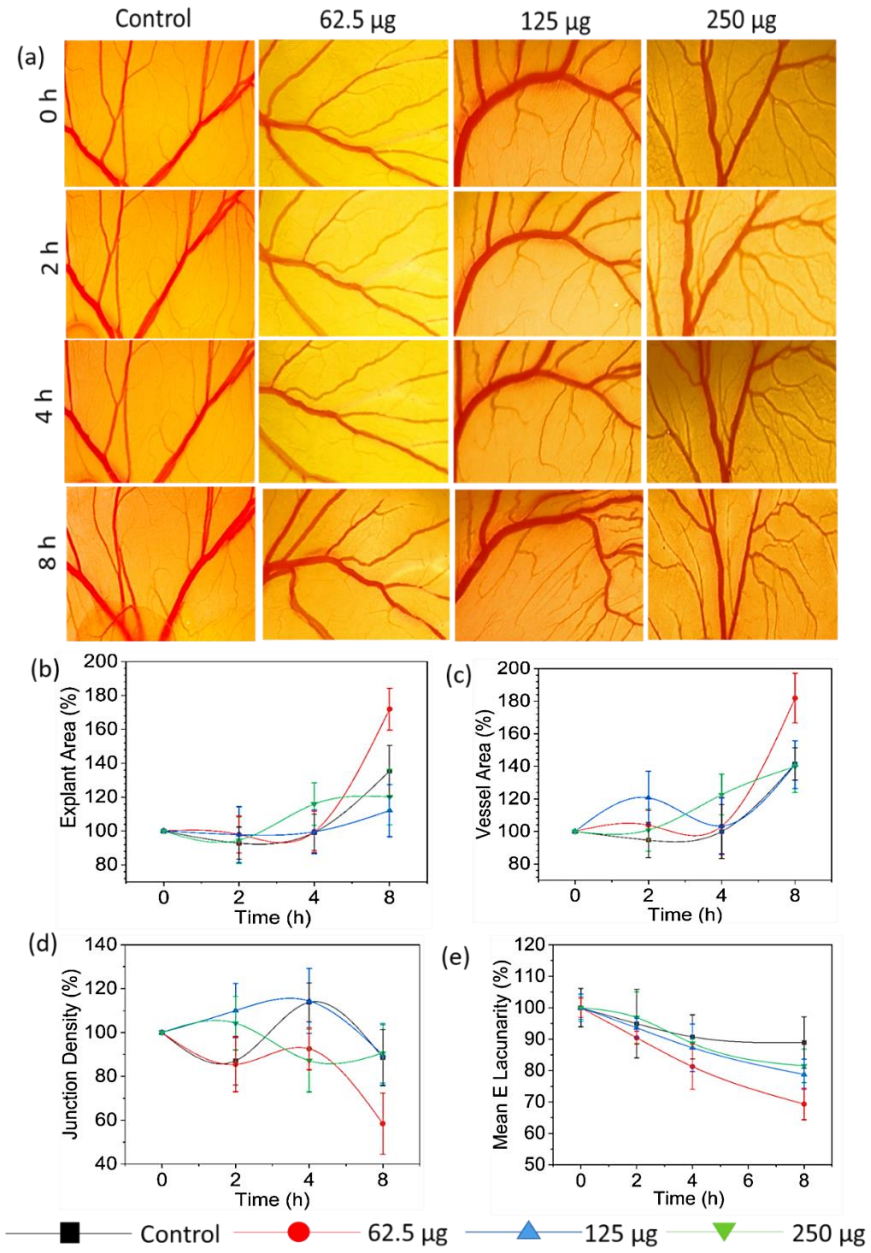

Figure 3.3.6 *Angiogenic effect of p(NAG-co-NAPA)$_{wc}$ NPs. Fig. (a) In ovo CEMA assay in the presence of p(NAG-co-NAPA)$_{wc}$ NPs support the branching angiogenesis in dose dependent manner. (b)-(e) represents several % changes in angiogenic parameters in percentage like Explant area, Vessel Area, Junction Density and Mean-E-Lacunarity, respectively in time and dose dependent manner.*

angiogenesis rather than sprouting of new blood vessels in dose and time dependent manner, where length and thickness of the developed blood vessels are found to be increased up to 8h of incubation. These results are matching well with the previously obtained cell based studies (**Figure 3.3.5**) and suggest that p(NAG-*co*-NAPA)$_{wc}$ NPs are angiogenic in nature at lower doses in time dependent manner and are effective for regenerative purposes.

3.3.4.6. *In vivo* wound healing efficacy of p(NAG-*co*-NAPA)$_{wc}$ nanoformulation

To check the *in vivo* wound healing efficiency of the prepared p(NAG-*co*-NAPA)$_{wc}$ NPs, a nanoformulation was developed. This nanoformulation was prepared by triturating the p(NAG-*co*-NAPA)$_{wc}$ NPs with an oleaginous base (see **Table S.3.2**) as mentioned in the method section. To avoid any kind of incongruities, it was examined for phase homogeneity, discolouration and aggregations. It seems to be smooth, consistent and devoid of any aggregation by observing under white light and touching (**Table S3.3.3**). As the target application is wound healing, therefore initially skin irritation study was performed with p(NAG-*co*-NAPA)$_{wc}$ nanoformulation, oleaginous base, –ve control with no treatment and +ve control with application of 1% formalin. For the reference, the irritation nature of 1% formalin was also tested with the *in ovo* model up to 24h, and images are shown in **Figure S3.3.12**. After 48h of treatment, it is observed that, other than +ve control group, no other groups exhibited skin irritation (**Figure 3.3.7(b1)**, **(b3)** and **(b4)**). In +ve control group, a substantial irritation at the site of application is clearly observed (**Figure 3.3.7(b2)**, black dashed circle). Further, the histology images were acquired from respective rat skin (**Figure 3.3.7(b1-b4)** and demonstrated that in +ve control group, damage areas are persisting in epidermis layer of skin (**Figure 3.3.7(c2)**, black dashed circle), whereas in all other three cases, layers of skin tissue are highly intact with no damage. Furthermore, for sensitivity study, development of erythema and edema is observed and certain values are assigned to each rat based

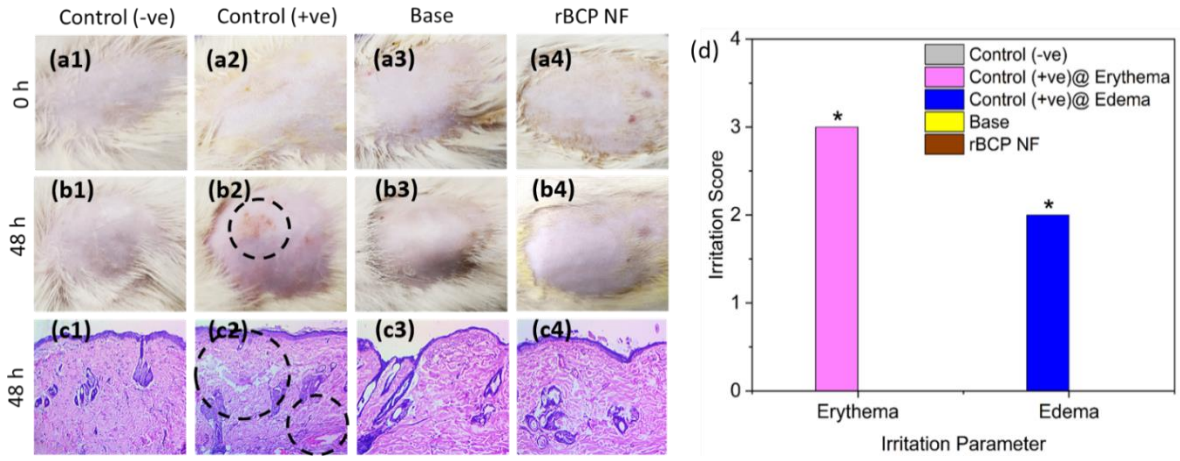

Figure 3.3.7. *In vivo skin irritation study. (a1-a4) Camera photographs of skin irritation study captured at 0h (before treatment) and (b1-b4) at 48h (after treatment), (c1-c4) histology images of H&E staining of tissue samples collected from b1-b4 rat skin at 20X magnification, and (d) calculation of irritation score based on occurrence of erythema and edema after 48h of treatment. The scale or erythema and edema are given in Table S3.3.4. rBCP NF represents p(NAG-co-NAPA)$_{wc}$ NPs based nanoformulation. Data are given as mean ± SD (n=3) (*p ≤ 0.05, **p ≤ 0.05-0.01, ***p ≤ 0.05-0.001 and ns: non-significant).*

on the irritation score (**Table S3.3.4**). It is observed that only +ve control group has developed erythema (value = 3) and edema (value = 2) on the skin (**Figure 3.3.7(d)**). The PDII score for the +ve control group and other groups are found to be 2 and 0.25, respectively. Which signifies that the p(NAG-*co*-NAPA)$_{wc}$ nanoformulation is non-irritant and non-sensitive to the skin up to 48h and furthermore ensures to use for *in vivo* wound healing study.

The *in vivo* wound healing experiments were performed on Wistar rats as mentioned in the methods section. For clear understanding, a timeline is provided in **Figure 3.3.8(a)**, which represents the procedure from day 0th (wound creation) to 15th day (healed tissue collection) along with treatment days and blood collection days. The impact of p(NAG-*co*-NAPA)$_{wc}$ nanoformulation was assessed and compared with control and base (**Figure 3.3.8**). It can be noted that the wound healing is a normal phenomenon of body homeostasis with time. However, from

Figure 3.3.8(b1-b15), it is evident that the wound healing progress is swift in p(NAG-*co*-NAPA)$_{wc}$ nanoformulation followed by base. However, for the control group it is delayed (**Figure 3.3.8(c)**). In the control group, complete wound closure is not achieved even after 13 days of post treatment and subsequently the wound closure rate is also increased for p(NAG-*co*-NAPA)$_{wc}$ nanoformulation at least 2-3 days earlier as compared to the control group. Moreover, relative wound area (%) was calculated and shown in **Figure 3.3.8(c)**. The corresponding wound areas (%) are found to be 94.96±2.04, 86.65±2.03 and 80.66±1.94 for control; 51.30±1.63, 54.98±2.20 and 30.55±1.36 for base and 83.33±4.20, 54.00±3.96, and 32.21±3.16 for p(NAG-*co*-NAPA)$_{wc}$ nanoformulation on 4th, 7th and 10th day of post treatment, respectively. Although on 7th and 10th day of treatment, both the base and p(NAG-*co*-NAPA)$_{wc}$ nanoformulation are exhibiting similar healed areas (%), however, on 13th day it decreases from 12.06±4.05 % for base to 3.71±3.26 % for p(NAG-*co*-NAPA)$_{wc}$ nanoformulation group. Particularly, on day 7th it is clearly visible from the wounded image of base (**Figure 3.3.8(b8)**) that some redness is observed on the skin. This redness may appear due to the inflammation occurred in the presence of base component only. To confirm this phenomenon, further inflammatory markers were checked and they supported our results, which is discussed in the subsequent sections. Additionally, it can be noted from the wounded images (**Figure 3.3.8(b1-b15)**) that from 4th day in all groups wound scabs developed and subsequently prevented the passage of blood and any fluids.[39] Although this early inflammatory healing stage is observed in all groups, progress is predominantly observed more in p(NAG-*co*-NAPA)$_{wc}$ nanoformulation group as shown in **Figure 3.3.8(b12)**. As anticipated, on 7th day of post-treatment, the production of granulation tissue in the p(NAG-*co*-NAPA)$_{wc}$ nanoformulation treated groups is significantly higher in the p(NAG-*co*-NAPA)$_{wc}$ nanoformulation group than control groups and by the 13th day of post treatment, the wounds in

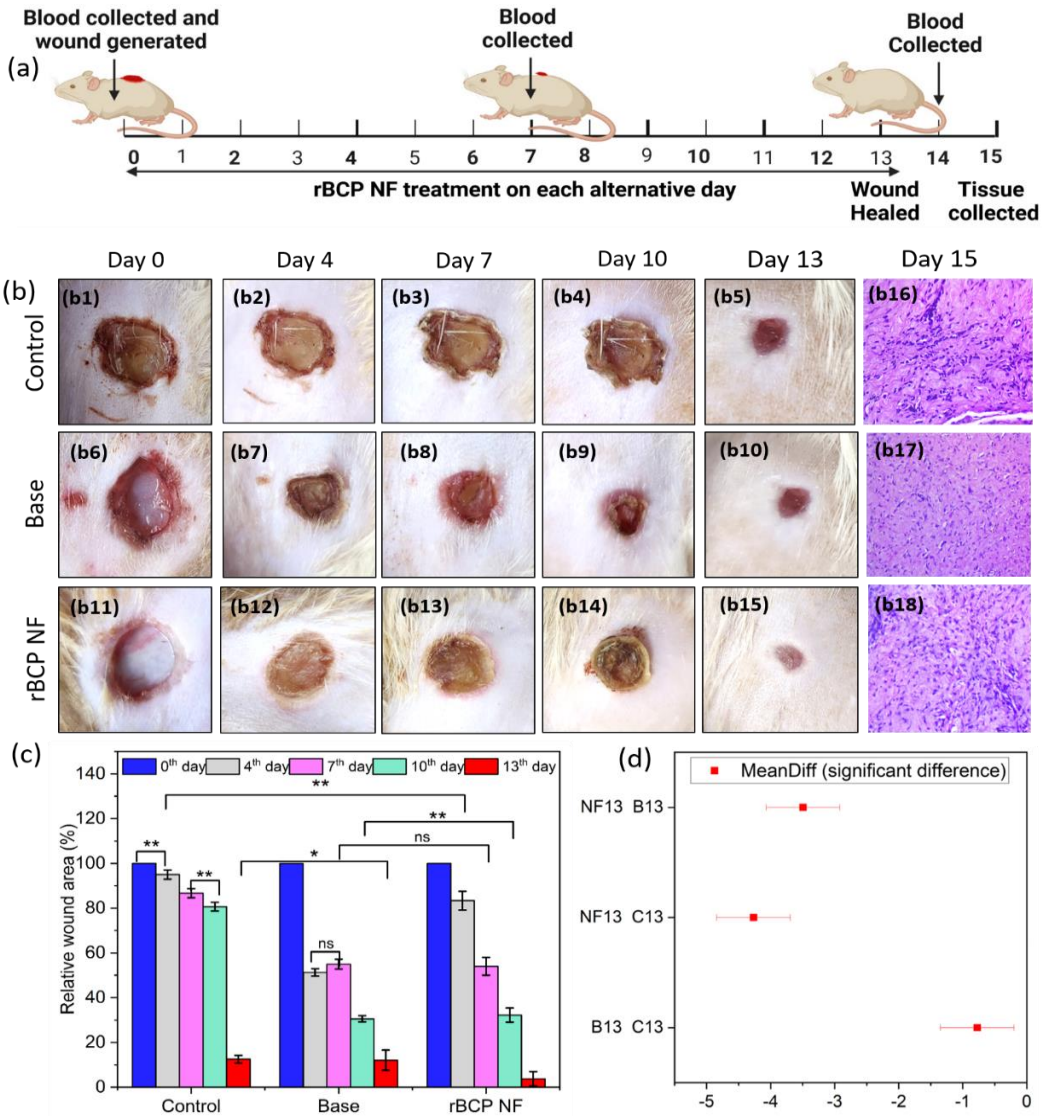

Figure 3.3.8. *Represents in vivo wound healing results. Fig. (a) Timeline of in vivo animal experiment followed in this work, (b) Optical microscopy images of wounds in three different groups (Control (b1-b5), Base (b6-b10) and rBCP NF (b11-b15) acquired in high resolution camera on 0^{th}, 4^{th}, 7^{th}, 10^{th} and 13^{th} days and (b16-b18) histology images of H&E staining of healed tissue on 15^{th} day of post treatment of control, base and rBCP NF, respectively, acquired at 20X magnification, (c) Relative wound area (%) at five different days (0^{th}, 4^{th}, 7^{th}, 10^{th} and 13^{th}) remaining to heal, and (d) Significant difference of mean wound area on 13^{th} day using the Turkey test to compare the mean in between three different groups. In figure 3.3.7(d), C: Control group, B: Base group and NF: rBCP nanoformulation. Other than represented statistical significance, all other combinations are significant with $P \leq 0.001$. rBCP NF represents $p(NAG\text{-}co\text{-}NAPA)_{wc}$ NPs based nanoformulation. Data are given as mean ±SD (n=3) (*$P \leq 0.05$, **$P \leq 0.05$-0.01, ***$P \leq 0.05$-0.001 and ns: non-significant)*

the p(NAG-*co*-NAPA)$_{wc}$ nanoformulation group are completely surrounded and covered by fully developed skin layers. In contrast, a significant wound area is remained unhealed in the control group. To support all these findings, histology study was performed for the tissue samples collected on the 15th day of post treatment (**Figure 3.3.8(b16-b18)**). From images, it is clearly evident that in the control group, clumped fibroblasts are generated. On the otherhand, in the base and p(NAG-*co*-NAPA)$_{wc}$ nanoformulation groups well defined dispersed fibroblasts are present. Further, among in the base and p(NAG-*co*-NAPA)$_{wc}$ nanoformulation groups, more fibroblasts are present in wounded area of the p(NAG-*co*-NAPA)$_{wc}$ nanoformulation group. This increased number of fibroblast cells suggested that on 15th day of post treatment a well-defined skin layer is formed and the wound is completely covered (**Figure 3.3.8(b18)**). Furthermore, a significant difference in mean wound area on 13th day using the Tukey test is shown in **Figure 3.3.8(d)** to compare the mean in between all the groups. Thus, the developed p(NAG-*co*-NAPA)$_{wc}$ nanoformulation can enhance wound healing process through angiogenesis (as discussed in previous section) which helps in repairing and remodelling the tissue via carrying nutrients and oxygen to the wounded site.

The levels of cytokine markers were checked using ELISA KIT on three different phases of wound healing, i.e.; inflammatory phase (0th day), proliferative phase (7th day), and remodelling phase (14th day). During these phases of wound healing, inflammatory markers level changes significantly and they manifest the effectiveness of applied nanoformulation. It is observed that on 14th day of post treatment, the relative levels of TNF-α, IL-1β and IL-6 are apparently lower than the control and base group (**Figure 3.3.9(a-c)**). The C-reactive protein (CRP), is generally released from liver to blood stream due to the reaction of inflammatory cytokines. After any injury or damage, the CRP level suddenly increases and with time as the wound get healed, the CRP level decreases. Herein, also on 0th and 14th day of post treatment CRP levels are observed to be high in

case of control as compared to p(NAG-*co*-NAPA)$_{wc}$ nanoformulation group (**Figure 3.3.9(d)**). On 7th and 14th day of post treatment, increased levels of IGF-1 are observed for p(NAG-*co*-NAPA)$_{wc}$ nanoformulation group, which suggests the higher rate of migration of keratinocytes to the damaged site (**Figure 3.3.9(e)**).[40] In contrast to the above findings, base is also showing wound healing capacity and on 7th day of post treatment an increased level of pro-inflammatory (TNF-α, IL-1β and IL-6) markers are observed as compared to the control group. This deterrent effect is observed due to the inflammation generated by base and it is clearly matching with the images obtained on the 7th day of post treatment (**Figure 3.3.8(b8)**). Furthermore, to study the relative fold change in selected gene expressions, RT-PCR study was conducted as mentioned in the method section and is shown in **Figure 3.3.9(f)** and **(g)**. It can be noted that, here in this study GAPDH was used as a housekeeping gene and control group's normal and wounded tissue's gene expression values are considered as internal control for normal and wounded tissues of base and p(NAG-*co*-NAPA)$_{wc}$ nanoformulation treated groups, respectively. RT-PCR studies of 14th day tissue samples revealed that, in the base group although the expression level of wounded tissue's TNF-α is decreased as compared to the normal tissue, however IL-1β expression level is found to be higher in value. This increased IL-1β expression in wounded tissue demonstrates that although ~88% wound is covered, still inflammation is there at wound site. Further, PECAM-1 (CD31) plays a central regulatory role in wound healing and helps in angiogenesis. Compared to normal tissue, in wounded tissue PECAM-1 expression is highly increased. In the process of wound healing, VEGF-A (Vascular Endothelial Growth Factor A) contributes both directly and indirectly to the migration of inflammatory cells and keratinocytes by stimulating cell proliferation and collagen deposition in remodelling phase and interacts with the KDR receptor (Kinase Insert

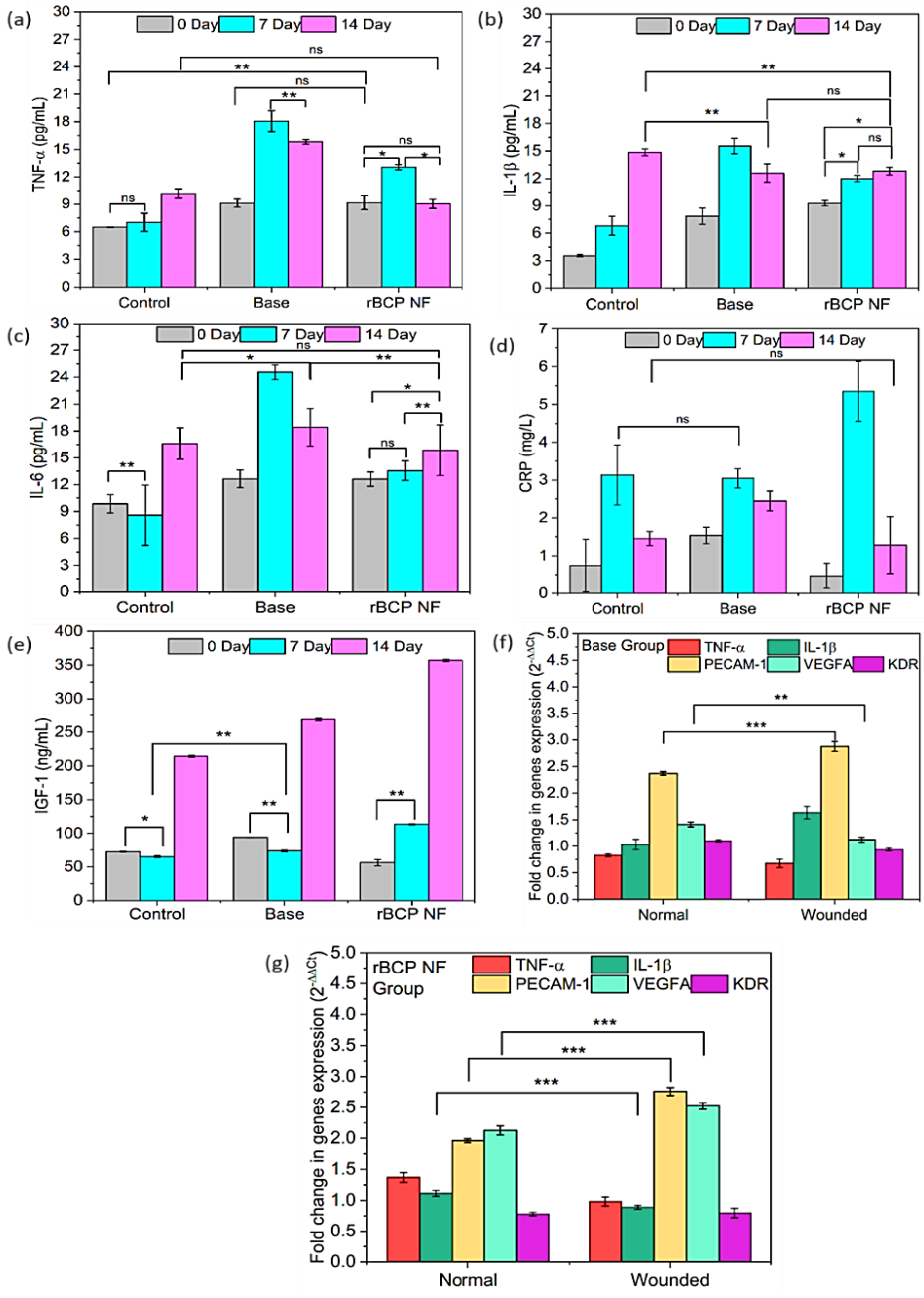

Figure 3.3.9. *Wound healing markers and real time expressions of selected genes during in vivo wound healing. Fig. (a) TNF-α, (b) IL-1β, (c) IL-6, (d) CRP and (e) IGF-1 levels analyzed by ELISA on 0th day (before wound creation), 7th and 14th day. Each data point represents the average ±SD of three independent determinations ($p< 0.05$). (f) and (g) Represents relative fold change in gene expressions (TNF-α, IL-1β, PECAM-1, VEGFA and KDR) obtained from RT-PCR results. Other than represented statistical significance, all other combinations are significant with $P \leq 0.001$. rBCP NF represents p(NAG-co-NAPA)$_{wc}$ NPs based nanoformulation. Data are given as mean ±SD (n=3) (*$P \leq 0.05$, **$P \leq 0.05$-0.01, ***$P \leq 0.05$-0.001 and ns: non-significant).*

Domain Receptor), facilitating its internalization into the nucleus. This interaction ultimately leads to the activation of the PI3-kinase/AKT signalling pathway.[41, 42] Although, for wounded tissues, the expression values of VEGFA and KDR are decreased with respect to the normal group, however these changes are statistically non-significant. Furthermore, in the p(NAG-*co*-NAPA)$_{wc}$ nanoformulation treated groups, for TNF-α and IL-1β, a decrease in gene expression values are observed for wounded tissue as compared to the normal tissue, which signifies that the wound is fully covered with no inflammation. For PECAM-1 and VEGEA an increase in gene expression levels are observed, which is evident from the earlier experiments (**Figure 3.3.8(c)**). For KDR, no such change in gene expression level is identified. Therefore, it can be suggested that p(NAG-co-NAPA)wc nanoformulation possesses an excellent regulatory effect on TNF-α, IL-1β, PECAM-1 and VEGFA genes for wound healing and tissue regeneration.

Here, in this work, we have synthesized the physically cross-linker free amino acid-based p(NAG-*co*-NAPA)$_{wc}$ copolymer NPs with tissue regenerative properties. The synthesis method is based on miniemulsion radical polymerization, which is quite simple and straightforward (**Scheme 3.3.1**). In this synthesis method we have avoided the use of chemical cross-linker like DVB or others in order to evade the toxicity generated due to their presence.[10, 12] The well-designed nanosystems have the particle sizes in the submicron range, to ensure effective interactions with biochemical and cellular components.[43] From various chemical and physical characterizations, it is confirmed that p(NAG-*co*-NAPA)$_{wc}$ NPs werev formed with a size range of c.a. 120-400nm (**Figure 3.3.2(a-b)** and **(d-e)**. From the zeta potential measurement, it is observed that the p(NAG-*co*-NAPA)$_{wc}$ NPs are stable as suspension (**Figure 3.3.2(f)**). The optical property and secondary structure of p(NAG-*co*-NAPA)$_{wc}$ NPs are investigated using CD spectroscopy, which demonstrates that p(NAG-*co*-NAPA)$_{wc}$ NPs exist in 100% β-turns form (**Figure 3.3.2(g)**). Further the distinct

separation between positive and negative bands of CD spectra (**Figure 3.3.2(g)**) is depicting the formation of a self-assembled structure in the selected medium.[28]

Further, a detailed MD simulation study has been performed to check the aggregation behaviour of the p(NAG-*co*-NAPA)$_{wc}$ NPs at three different temperatures (298, 310 and 315K). Compared to all three temperatures, particularly at 310K (physiological temperature) the aggregation of the polymer chains is found quite high. This aggregation behaviour revealed the higher stability of NPs in body temperature (**Figure 3.3.3**). From MD simulation, it is further revealed that the p(NAG-*co*-NAPA)$_{wc}$ NPs are self-assembled two different regions exist, i.e., hydrophobic and hydrophilic. The hydrophobic region is made up of phenyl rings present in the NAPA unit and the hydrophilic region appears based on the carboxylic acid group present in the NAG unit. The calculation of the distance between two benzene rings in a hydrophobic region are found to be in the range of 4.2 to 5.4Å, which further confirms the existence of π-π interactions between the hydrophobic benzene rings (**Scheme 3.3.2**). It is further confirmed that self-assembled porous p(NAG-*co*-NAPA)$_{wc}$ NPs are formed by noncovalent crosslinking, and due to the π-π interactions or π stacking. Simultaneously, dynamics of p(NAG-*co*-NAPA)$_{wc}$ NPs has been studied at POPC bilayer membrane, which is an important aspect for *in vivo* studies (**Figure 3.3.4(i)** and **(j)**). These interaction studies revealed the biocompatible nature of p(NAG-*co*-NAPA)$_{wc}$ NPs. It is important to note that, although a concentrated system was employed in simulations to investigate the structure and biocompatibility of the p(NAG-*co*-NAPA)$_{wc}$ NPs, the results obtained were found to be in good agreement with experimental observations conducted at a diluted concentration (self-assembly behavior of the NP (**Figure 3**) with good colloidal stability (**Figure 2(f)**) and close association of dimer unit with POPC bilayer **Figure 4(j)** i.e., biocompatible nature of the NP **Figure 5(a)**.

Further to establish the biomedical applications of p(NAG-*co*-NAPA)$_{wc}$ NPs, cytocompatibility and hemocompatibility of p(NAG-*co*-NAPA)$_{wc}$ NPs have been checked. It is found that the p(NAG-*co*-NAPA)$_{wc}$ NPs are proliferative in L929 mouse fibroblast cells up to 1000µg/mL (**Figure 3.3.5(a)**). The hemocompatibility study confirmed that designed NPs are non-hemolytic in rat erythrocytes as compared to +ve control (**Figure 3.3.5(b)**), which means that the p(NAG-*co*-NAPA)$_{wc}$ NPs do not interfere with the mechanisms of Na+/K+ ATPase and aquaporins.[44] The migration and proliferation of fibroblasts in the presence of biomaterials are essential processes in the healing of skin wounds. The ability of p(NAG-*co*-NAPA)$_{wc}$ NPs to promote both proliferation and migration supports the idea that they aid in re-epithelialization and the restoration of skin functions (**Figure 3.3.5(c)**).[45] During acute injury, blood vessel damage leads to the nutrient and oxygen shortages in tissues. From *in ovo* CEMA assay, it is found that p(NAG-*co*-NAPA)$_{wc}$ NPs help to enhance the vascular sprouting and angiogenesis, particularly at lower concentrations (**Figure 3.3.6**). These *in vitro* and *in ovo* results confirm that p(NAG-*co*-NAPA)$_{wc}$ NPs can be used in *in vivo* wound healing.

For *in vivo* study, medical grade materials were used to develop p(NAG-*co*-NAPA)$_{wc}$ nanoformulation and underwent standard quality control tests for preclinical studies, ensuring its suitability for topical applications by adjusting for skin pH using triethanolamine (**Table S3.3.3**). Further, homogeneity and spreadability are crucial for any nanoformulation as lack of uniformity can lead to secondary injuries by causing delayed healing processes. Therefore, conducting a dermal irritancy test is essential. After applying the formulation, it is assessed for erythema and edema using the Draize scoring scale (**Table S3.3.4**), with results converted into PDII values via eqn. (3.3.1). The p(NAG-*co*-NAPA)$_{wc}$ nanoformulation was applied on rat skin and was compared with standard irritant, i.e., formalin. Except positive control, no rats showed cutaneous irritation

(**Figure 3.3.7(b2)** and **(c2)**). Additionally, a period of 7-days observation was carried out for all groups and none of the animals showed any unusual behavior or toxicity. Furthermore, wound healing capacity of p(NAG-*co*-NAPA)$_{wc}$ nanoformulation was carried out using Wistar rats by generating an 8-10mm wound on rats. It is observed that within 13th day of post treatment, major part of the wound is covered as compared to the base and control group (**Figure 3.3.8(b5)**, **(b10)** and **(b15)**). Although base and p(NAG-*co*-NAPA)$_{wc}$ nanoformulation treated groups are showing similar extent of wound covered areas up to 10th day of post treatment, however, on 13th day of treatment whole wound was covered for p(NAG-*co*-NAPA)$_{wc}$ nanoformulation treated groups. These findings are matching well with the results obtained from histology study of 14th day old wounds, which demonstrates the formation of dense and dispersed fibroblast cells in the p(NAG-*co*-NAPA)$_{wc}$ nanoformulation treated groups as compared to the base and control group (**Figure 3.3.7(b18)**).

Finally, the study focused on the inflammatory, proliferative and remodelling phases of wound healing i.e., 0th, 7th and 14th day of treatment, respectively. It is observed that the topically applied p(NAG-*co*-NAPA)$_{wc}$ nanoformulation influenced various chemokines, cytokines and growth factors in the systemic blood of both control and treated groups of animals in all these three days. The p(NAG-*co*-NAPA)$_{wc}$ nanoformulation treated groups exhibited almost equal levels of TNF-α, IL-1β and IL-6 (**Figure 3.3.8(a-c)**), indicating effective anti-inflammatory regulation by p(NAG-*co*-NAPA)$_{wc}$. For CRP also a decrease in marker level is observed on 14th day of post treatment for the p(NAG-*co*-NAPA)$_{wc}$ nanoformulation treated groups, which demonstrates no inflammation persists on the wound site. While for the base, although the wound is relatively closed as compared to the control group, CRP is still higher in value on 14th day (**Figure 3.3.9(d)**). By day 14th, IGF-1 levels significantly increased in the treated groups, suggesting enhanced keratinocyte migration

towards the wound site (**Figure 3.3.9(e)**). This rise in IGF-1 values is also correlated with the increased vascularity, as it activates the PI3-kinase/Akt signalling pathway and up-regulates PDGFB, MMPs and other angiogenic growth factors.[22] Additionally, the RT-PCR results of 14th day of tissue samples revealed that comparing to base group, in p(NAG-*co*-NAPA)$_{wc}$ nanoformulation treated groups TNF-α and IL-1β expression levels are less and VEGFA and PECAM-1 expression levels are high, which clearly signifies that p(NAG-*co*-NAPA)$_{wc}$ nanoformulation has a strong correlation with regulatory genes related to wound healing and tissue regeneration (**Figure 3.3.9(f)** and **(g)**). Hence, from this work it can be stated that, this self-assembled physically cross-linked p(NAG-*co*-NAPA)$_{wc}$ can efficiently act as a potential regenerative medicine.

3.3.5. Summary and Conclusions for this part

In summary, we have successfully synthesized a novel self-assembled amino acid based random di-block copolymer NPs of NAG and NAPA, i.e.; p(NAG-*co*-NAPA)$_{wc}$. From various spectroscopy studies, it is confirmed that p(NAG-*co*-NAPA)$_{wc}$ was formed via mini emulsion radical polymerization without using any additional covalent cross-linker. The H-bonds caused by carboxylic acid groups of NAG and π-π stacking caused by the phenyl ring of NAPA triggered non-covalent cross-linking and accelerated the formation of self-assembled spherical p(NAG-*co*-NAPA)$_{wc}$ NPs and promoted the construction of a beautiful network-like structure. MD simulation studies also revealed that the p(NAG-*co*-NAPA)$_{wc}$ NPs formed aggregates in the temperatures range of 298 to 315K. In aggregates, hydrophobic and hydrophilic groups can make separate domains and shows interactions in a proximity. As anticipated, the hemolysis study and *in vitro* cytotoxicity assay revealed that p(NAG-*co*-NAPA)$_{wc}$ NPs are hemocompatible and cytocompatible in nature. The exciting hallmarks, angiogenesis, cell migration and proliferation properties

established the regenerative property of p(NAG-*co*-NAPA) NPs. Additionally, *in vivo* experiments demonstrated p(NAG-*co*-NAPA)$_{wc}$ nanoformulation's potential for use in regenerative medicine i.e.; acute wound healing without additional growth factors such as cytokines, cells, or genes etc. Thus, p(NAG-*co*-NAPA)$_{wc}$ NPs are paramount for clinical and therapeutic applications.

3.3.6. References

1. Deane, O.J., J. Jennings, and S.P. Armes, *Shape-shifting thermoreversible diblock copolymer nano-objects via RAFT aqueous dispersion polymerization of 4-hydroxybutyl acrylate.* Chemical Science, 2021. **12**(41): p. 13719-13729.
2. Sun, H., D. Liu, and J. Du, *Nanobowls with controlled openings and interior holes driven by the synergy of hydrogen bonding and π–π interaction.* Chemical Science, 2019. **10**(3): p. 657-664.
3. Yamala, A.K., et al., *Poly-N-acryloyl-(l-phenylalanine methyl ester) hollow core nanocapsules facilitate sustained delivery of immunomodulatory drugs and exhibit adjuvant properties.* Nanoscale, 2017. **9**(37): p. 14006-14014.
4. Yamala, A.K., et al., *P-LME polymer nanocapsules stimulate naïve macrophages and protect them from oxidative damage during controlled drug release.* Journal of Applied Polymer Science, 2020. **137**(6): p. 48363.
5. Que, Y., et al., *Enhancing Photodynamic Therapy Efficacy by Using Fluorinated Nanoplatform.* ACS Macro Letters, 2016. **5**(2): p. 168-173.
6. Liu, X., et al., *The Aging Behavior and Life Prediction of CFRP Rods under a Hygrothermal Environment.* Polymers, 2023. **15**(11): p. 2490.
7. Talelli, M., et al., *Core-crosslinked polymeric micelles: Principles, preparation, biomedical applications and clinical translation.* Nano Today, 2015. **10**(1): p. 93-117.
8. Deng, C., et al., *Biodegradable polymeric micelles for targeted and controlled anticancer drug delivery: Promises, progress and prospects.* Nano Today, 2012. **7**(5): p. 467-480.
9. Jeong, C.H., et al., *In vitro toxicity assessment of crosslinking agents used in hyaluronic acid dermal filler.* Toxicology in Vitro, 2021. **70**: p. 105034.
10. Hanson, M. and A. Wypych, *1 - Introduction*, in *Databook of Curatives and Crosslinkers*, M. Hanson and A. Wypych, Editors. 2019, ChemTec Publishing. p. 1-2.
11. Chen, J., E.S. Garcia, and S.C. Zimmerman, *Intramolecularly Cross-Linked Polymers: From Structure to Function with Applications as Artificial Antibodies and Artificial Enzymes.* Accounts of Chemical Research, 2020. **53**(6): p. 1244-1256.
12. Amgoth, C., et al., *'Plate-like-coral' polymer particles with dendritic structure and porous channels: Effective delivery of anti-cancer drugs.* Journal of Applied Polymer Science, 2021. **138**(19): p. 50386.
13. Shao, Y., et al., *Reversibly Crosslinked Nanocarriers for on-demand Drug Delivery in Cancer Treatment.* Therapeutic Delivery, 2012. **3**(12): p. 1409-1427.

14. Buwalda, S., et al., *Stabilization of poly(ethylene glycol)-poly(ε-caprolactone) star block copolymer micelles via aromatic groups for improved drug delivery properties.* Journal of Colloid and Interface Science, 2018. **514**: p. 468-478.
15. Hu, Q., et al., *Tailoring the physicochemical properties of core-crosslinked polymeric micelles for pharmaceutical applications.* Journal of Controlled Release, 2016. **244**: p. 314-325.
16. Lin, M., et al., *Advances in non-covalent crosslinked polymer micelles for biomedical applications.* Materials Science and Engineering: C, 2021. **119**: p. 111626.
17. Chen, J., et al., *Core cross-linked double hydrophilic block copolymer micelles based on multiple hydrogen-bonding interactions.* Polymer Chemistry, 2017. **8**(20): p. 3066-3073.
18. Wu, G., et al., *Glucose-responsive complex micelles for self-regulated delivery of insulin with effective protection of insulin and enhanced hypoglycemic activity in vivo.* Colloids and Surfaces B: Biointerfaces, 2019. **180**: p. 376-383.
19. Zhuang, W.-R., et al., *Applications of π-π stacking interactions in the design of drug-delivery systems.* Journal of Controlled Release, 2019. **294**: p. 311-326.
20. Hosseinkhani, H., P.-D. Hong, and D.-S. Yu, *Self-Assembled Proteins and Peptides for Regenerative Medicine.* Chemical Reviews, 2013. **113**(7): p. 4837-4861.
21. Löwik, D.W.P.M. and J.C.M. van Hest, *Peptide based amphiphiles.* Chemical Society Reviews, 2004. **33**(4): p. 234-245.
22. Gupta, P.S., et al., *Nitric oxide releasing novel amino acid-derived polymeric nanotherapeutic with anti-inflammatory properties for rapid wound tissue regeneration.* Nanoscale, 2024. **16**(4): p. 1770-1791.
23. Gupta, P.S., et al., *In vivo potential of polymeric N-acryloyl-glycine nanoparticles with anti-inflammatory activities for wound healing.* Materials Advances, 2023. **4**(20): p. 4718-4731.
24. Hunter, C.A. and J.K.M. Sanders, *The nature of .pi.-.pi. interactions.* Journal of the American Chemical Society, 1990. **112**(14): p. 5525-5534.
25. Jiang, J., et al., *Self-Assembled Nanolayers of Conjugated Silane with π−π Interlocking.* ACS Nano, 2010. **4**(7): p. 3773-3780.
26. Purohit, H.S., et al., *Investigating the Impact of Drug Crystallinity in Amorphous Tacrolimus Capsules on Pharmacokinetics and Bioequivalence Using Discriminatory In Vitro Dissolution Testing and Physiologically Based Pharmacokinetic Modeling and Simulation.* Journal of Pharmaceutical Sciences, 2018. **107**(5): p. 1330-1341.
27. Schittny, A., J. Huwyler, and M. Puchkov, *Mechanisms of increased bioavailability through amorphous solid dispersions: a review.* Drug Delivery, 2020. **27**(1): p. 110-127.
28. Werber, L., et al., *Isothermal Titration Calorimetry of Chiral Polymeric Nanoparticles.* Chirality, 2015. **27**(9): p. 613-618.
29. Amdursky, N. and M.M. Stevens, *Circular Dichroism of Amino Acids: Following the Structural Formation of Phenylalanine.* ChemPhysChem, 2015. **16**(13): p. 2768-2774.
30. Adler-Abramovich, L., et al., *Phenylalanine assembly into toxic fibrils suggests amyloid etiology in phenylketonuria.* Nature Chemical Biology, 2012. **8**(8): p. 701-706.
31. Lu, Y., et al., *Strategies to improve micelle stability for drug delivery.* Nano Research, 2018. **11**(10): p. 4985-4998.

32. Kim, S., et al., *Overcoming the barriers in micellar drug delivery: loading efficiency, in vivo stability, and micelle–cell interaction.* Expert Opinion on Drug Delivery, 2010. **7**(1): p. 49-62.
33. Rideau, E., et al., *Liposomes and polymersomes: a comparative review towards cell mimicking.* Chemical Society Reviews, 2018. **47**(23): p. 8572-8610.
34. Yorulmaz Avsar, S., et al., *Biomolecules Turn Self-Assembling Amphiphilic Block Co-polymer Platforms Into Biomimetic Interfaces.* Frontiers in Chemistry, 2019. **6**.
35. Zhao, Y., et al., *Conformational Preferences of π–π Stacking Between Ligand and Protein, Analysis Derived from Crystal Structure Data Geometric Preference of π–π Interaction.* Interdisciplinary Sciences: Computational Life Sciences, 2015. **7**(3): p. 211-220.
36. Maksimenko, O., et al., *Doxorubicin-loaded PLGA nanoparticles for the chemotherapy of glioblastoma: Towards the pharmaceutical development.* International Journal of Pharmaceutics, 2019. **572**: p. 118733.
37. Zudaire, E., et al., *A Computational Tool for Quantitative Analysis of Vascular Networks.* PLOS ONE, 2011. **6**(11): p. e27385.
38. Li, R., et al., *Bioactive Materials Promote Wound Healing through Modulation of Cell Behaviors.* Advanced Science, 2022. **9**(10): p. 2105152.
39. Schultz, G.S., et al., *Principles of wound healing.* Mechanisms of vascular disease: A reference book for vascular specialists [Internet], 2011.
40. Deng, P., et al., *Chitosan-based hydrogels with injectable, self-healing and antibacterial properties for wound healing.* Carbohydrate Polymers, 2022. **276**: p. 118718.
41. Wilgus, T.A., *Vascular Endothelial Growth Factor and Cutaneous Scarring.* Advances in Wound Care, 2018. **8**(12): p. 671-678.
42. Domingues, I., et al., *VEGFR2 Translocates to the Nucleus to Regulate Its Own Transcription.* PLOS ONE, 2011. **6**(9): p. e25668.
43. Moreno-Sastre, M., et al., *Stability study of sodium colistimethate-loaded lipid nanoparticles.* Journal of Microencapsulation, 2016. **33**(7): p. 636-645.
44. Greco, I., et al., *Correlation between hemolytic activity, cytotoxicity and systemic in vivo toxicity of synthetic antimicrobial peptides.* Scientific Reports, 2020. **10**(1): p. 13206.
45. Han, G., et al., *Nitric Oxide–Releasing Nanoparticles Accelerate Wound Healing by Promoting Fibroblast Migration and Collagen Deposition.* The American Journal of Pathology, 2012. **180**(4): p. 1465-1473.

Chapter 3

Results and Discussion (Part IV)

The outcome of this part:

1. Communicated in RSC Materials Advances: '*Angiogenic properties of Poly(N-acryloyl-glycine)-co-(N-acryloyl-L-phenylalanine methyl ester) nanoparticles: Quantitative Assessment via Gray Level Co-occurrence Matrix based Image Processing***'**

2. Filled an Indian Patent: '*Quantitative Assessment of Angiogenesis via Gray Level Co-Occurrence Matrix Based Image Processing" Application No. 202511050871, Dated 27 May, 2025***'**

Chapter 3: Part IV

Quantitative Assessment of Angiogenesis via Gray Level Co-occurrence Matrix based Image Processing using poly(N-acryloyl-glycine)-co-(N-acryloyl-L-phenylalanine methyl ester) nanoparticles

3.4.1 Abstract: Angiogenesis, a complex physiological process that involves in the formation of new blood vessels. Despite the advancements in assessing the angiogenesis, there are still a substantial opportunity for the development of more accessible, reliable, and automated processes for estimating this complex phenomenon. Quantifying the angiogenesis is difficult due to the non-availability of the suitable methods. Manual analysis and quantification of such results with existing approaches are typically labour-intensive and affected by inter-experimenter variability. This line, the main aim of the present work is to develop a new method of assessing angiogenesis using gray-level co-occurrence matrix (GLCM)-based texture features image processing tool, which could be co-related with more reliable parameters. To establish this method, an amino acid based copolymer NPs such as poly[(*N*-acryloyl glycine)-*co*-(*N*-acryloyl-(L-phenylalanine methyl ester))] p(NAG-*co*-NAPA) has been synthesized through miniemulsion polymerization, with an average particle size of 100-13 nm in dia. with porous structure. p(NAG-*co*-NAPA) NPs is biocompatible and exhibit cell proliferation upto ~115-120% with L929 (mouse fibroblast), HUVEC (Human umbilical endothelial cells) and Raw 264.7 macrophages. In the 2nd step, the pro-angiogenic properties of p(NAG-*co*-NAPA) NPs were investigated through tube formation assay and '*in ovo'* model followed by analysis of images by Angiotool to predict regenerative efficacy. Then, microscopic images (~1000) of newly formed blood vessels were segmented using adaptive thresholding, and seven GLCM-based texture features were computed to analyze the images

correlating with seven different parameters (Number of pixels in blood vessels, Entropy, Energy, Mean, Contrast, Dissimilarity and Variance). The method developed through this work revealed that this new approach of analysis could be effective for assessing the angiogenesis with a conclusion that the p(NAG-*co*-NAPA) NPs could be paramount for various regenerative and therapeutic applications.

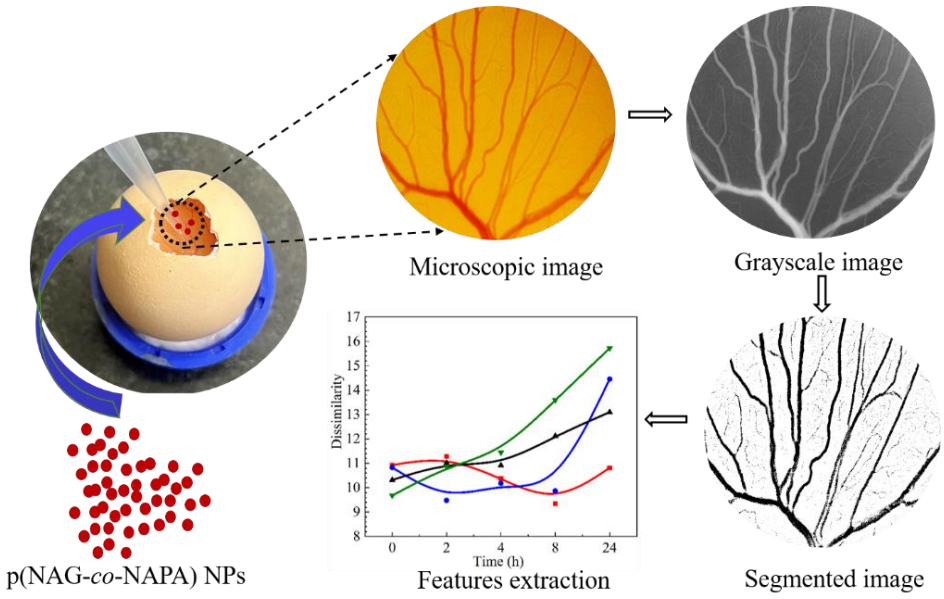

***Table of Content Text**: Poly(N-acryloyl glycine)-co-(N-acryloyl-L-phenylalanine methyl ester) copolymer p(NAG-co-NAPA) NPs with angiogenic properties and is paramount for the wound care and regeneration applications.*

3.4.2 Introduction

In the biological system, each organ is supplied by an artery that delivers oxygen and nutrients throughout the body.[1, 2] Endothelial cells, the major constituent of arteries are responsible for forming tubular vessels, which are lined by a basement membrane, mural cells, and extracellular matrix[1] that can be controlled by suitable biomaterials and medicines.[3] This complex three-dimensional (3D) structure of blood vessels can be remodeled to get response to stimulation from chemokines or cytokines released and/or by synthetic biomaterials including polymers[4] during

embryonic development, various diseases and disorders.[5, 6] The process ‘angiogenesis’ is a unique phenomenon that involves in the formation of new blood vessels from pre-existing one, which could be controlled using amino acid-based biopolymers as therapeutics.[7-10] In healthy tissues, it is tightly regulated to maintain vascular homeostasis and respond to changes in metabolic demands. However, in pathological conditions, it is dysregulated due to varying factors, like in tumors and cancer, and subsequently leads to the formation of abnormal, leaky blood vessels.[11] Thus, an accurate evaluation and quantification of angiogenesis is crucial for qualifying a novel therapeutic such as polymeric material for its use in clinical applications.

Microscopic images obtained through angiogenesis assay such as *in ovo or in vivo* models are the regular practice for analyzing tissue and cell structures both in normal and diseased conditions. Numerous CAM assay studies employ diverse vasculature quantification methods, leading to outcome heterogeneity in the results.[12-15] The image analysis through the available tools such as like ImageJ, AngioTool, and Angioquant each have their limitations, including computational demands, manual steps, and long processing times, with costly software.[16] While MATLAB-based tools like RAVE[17] and REAVER[18] although emerged, RAVE lacks in 3D image analysis capabilities, and REAVER remain under development. The absence of a standardized CAM vasculature quantification methodology limits inter-study data analysis and comparison. Thus, a new method for the analysis of angiogenesis accurately is essential. To address the said limitations, our present work utilizes a Gaussian adaptive threshold method followed by gray level co-occurrence matrix (GLCM)-based textural feature analysis for segmentation and angiogenesis assessment of a model amino acid based biopolymer. This thresholding method precisely segments blood vessels from the background,[19] outperforming contour[20] and clustering[21] algorithms. The texture-based features provide a more comprehensive description of the image and incorporate

information about the spatial distribution of changes in gray intensity levels.[22] By accounting for both spatial and intensity information, this method analyzes angiogenesis and predict the therapeutic doses for anti/pro-angiogenic biomolecules for multiple therapeutic applications.

Further, a wide variety of pro-angiogenic biomolecules and angiogenesis inhibitors have been designed using inorganic materials, polymers, or their composites, etc.[23] It is reported that the angiogenic responses could be controlled by tailoring the biomaterials' structure and properties.[4] Many peptide, gene, and growth factors based therapies are also reported, which were used through a multifaceted approach to enhance angiogenesis and tissue regeneration.[24-26] However, the future potential of these approaches is constrained by multiple factors, such as variable responses, specificity to certain cell types, short duration of action, differences between preclinical and clinical outcomes, regulatory challenges, and issues related to cost-effectiveness.[27-29] Furthermore, amino acid metabolism plays a significant role in regulating and maintaining vascular function, including coagulation, vascular tone, cell growth and differentiation, redox homeostasis, immune and inflammatory responses, and fibrinolysis, etc. Despite the well-defined metabolic pathways for the de novo synthesis of non-essential amino acids, highly proliferative cells often require an external supply of some of these amino acids for their optimal growth.[30, 31] The essential amino acid, L-phenylalanine promotes tetrahydrobiopterin synthesis, increases the nitrite levels by activating the guanosine triphosphate cyclase hydrolase pathway, and leads to improved endothelial functions,[32-34] whereas in some reports it is found that phenylalanine was associated with macrovascular diseases.[35] Similarly, glycine the smallest and simplest non-essential amino acid participate in many physiological pathways and are found to be both angiogenic and antiangiogenic. Amin *et al.* have reported the effect of glycine on angiogenesis during embryonic development via CAM assay showing that exogenous glycine inhibited blood vessel growth by

>50%.[36] The dietary glycine has been reported as a potent anti-angiogenic agent which reduce wound healing and tumor growth by reducing iNOS expression.[37] An ambiguity to the above discussions, Guo *et al.* have reported that glycine shows angiogenic behavior both *in vitro* and *in vivo*.[38] Similarly, in our previous studies, glycine-based polymeric NPs and hydrogels were found to promote angiogenesis, leading to enhanced tissue and neuron regeneration.[7, 10] By taking account of the above studies, we speculated that the combination of glycine and phenylalanine may show pro-angiogenic behavior by complementing each other and motivated us to synthesize a model copolymer i.e., p(NAG-*co*-NAPA) NPs, which consists of *N*-acryloyl glycine (NAG) and *N*-acryloyl-L-phenylalanine methyl ester (NAPA) as two monomers. Their respective homopolymers p(NAG) and p(NAPA) were synthesized and reported elsewhere.[7, 39] Further, the therapeutic applications are optimized by analysing the angiogenic properties through standard *in vitro* and *in ovo* models (Chorioallantoic Membrane (CAM) Assay) across a range of doses and time points.

In this work, the first step was the synthesis of p(NAG-*co*-NAPA) NPs through mini emulsion free radical polymerization followed by their hemocompatibility and biocompatibility studies against RBCs, L929 (mouse fibroblast), Raw 264.7 (macrophages), PC12 (neural crest-derived cell) and HUVEC cells. Based on the observations, the dose and time dependent angiogenic properties of model p(NAG-*co*-NAPA) copolymer NPs were studied through tube formation assay using HUVAC cells and *in ovo* model to predict their regeneration efficiency. The tube formation assay results were cross-verified with the Angiotool method to establish the Grey level co-occurrence matrix (GLCM) based texture feature method as a gold standard for the estimation of the level of angiogenesis. Further, the microscopic images obtained from *in ovo* experiments were also segmented using Image processing based Gaussian adaptive threshold followed by GLCM

code to compute 7 different Grey texture features which include the number of pixels of blood vessels, entropy, energy, mean, contrast, variance, and dissimilarity. Finally, by combining the experimental and computational results, the potential of the new Image processing tool approach for analyzing angiogenesis has been developed, and the future potential of p(NAG-*co*-NAPA) NPs in wound care and tissue regeneration has been established.

3.4.3 Experimental

3.4.3.1 Materials

The chemicals and cell lines used for this work are listed in Chapter 2 (Page No. 52-52, Section 2.2).

3.4.3.2 Synthesis of NAG, NAPA monomers and p(NAG-*co*-NAPA) NPs

3.4.3.2.1 Synthesis of NAG and NAPA monomers

The synthesis procedure of NAG and NAPA monomers are given in Methodologies section of Chapter 2 (Page No. 53-55, Section 2.3.1.1. and 2.3.1.2.).

3.4.3.2.2 Synthesis of p(NAG), p(NAPA) and p(NAG-*co*-NAPA) NPs

The synthesis method of p(NAG), p(NAPA) and p(NAG-*co*-NAPA) NPs is given in Methods section of Chapter 2 (Page No. 55, Section 2.3.1.3.). Here NAG:NAPA ratio is 1:1 (P1).

3.4.3.3 Characterization of NAG, NAPA, p(NAG), p(NAPA), and p(NAG-*co*-NAPA) NPs

The procedures followed for the characterization of monomers and polymer NPs are given in the Methodologies section of Chapter 2 (Page No. 57, Section 2.3.2.).

3.4.3.4 Morphological and colloidal stability Evaluation

The characterization details, colloidal stability and morphology study are given in Methodologies section of Chapter 2 (Page No. 58-59, Section 2.3.3.).

3.4.3.5 CMC determination

The method followed for the Critical Micelle Concentration (CMC) of p(NAG-*co*-NAPA) NPs with varying concentrations ranging from 1000µg/mL to 0.488µg/mL is described in the Methodologies section of Chapter 2 (Page No. 58-59, Section 2.3.3.1.).

3.4.3.6 *In vitro* cell viability

The method followed for the cell viability study of the synthesized p(NAG), p(NAPA) and p(NAG-*co*-NAPA) NPs with four different cell lines such as L929, Raw 264.7, PC12 (400 µg/mL to 3.125 µg/mL) and HUVECs (200 µg/mL to 5 µg/mL) is described briefly in the Methodologies section of Chapter 2 (Page No. 67, Section 2.3.7.1.).

3.4.3.7 Hemolysis Study

The method followed for the hemolysis assay of p(NAG-*co*-NAPA) NPs, at 500µg/mL to 7.8125µg/mL is described in Methods section of the Chapter 2 (Page No. 68, Section 2.3.7.3).

3.4.3.8 Tube formation assay

The complete method followed for the tube formation assay by p(NAG-*co*-NAPA) NPs (1, 10, and 100µg/mL) is described in the Methodologies section of the Chapter 2 (Page No. 73, Section 2.3.7.12).

3.4.3.9 Experimental setup to acquire microscopic images to study the angiogenesis through *in ovo CAM* assay model

The procedures followed for the CAM assay study of p(NAG-*co*-NAPA) NPs at doses 1, 10, and 100µg is described in the Methodologies section of Chapter 2 (Page No. 73-74, Section 2.3.8.1).

3.4.3.10 Processing of microscopic images through GLCM based image processing tool

The steps followed for the processing of microscopic images acquired at predefined time intervals is described briefly in the Methodologies section of Chapter 2 (Page No. 63, Section 2.3.5.4.1.) along with the relevant equations.

3.4.3.11 Quantitative measurement of angiogenesis using GLCM texture based features

The steps followed for the quantitative measurement of angiogenesis using GLCM texture based features is described briefly in the Methodologies section of Chapter 2 (Page No. 63-65, Section 2.3.5.4.2.) along with the relevant equations.

3.4.3.12 Hardware and Software used for angiogenesis analysis

The hardware and software used for this study is given Methodologies section of Chapter 2 (Page No. 65, Section 2.3.5.4.3.).

3.4.3.13 Statistical Significance

Statistics applied on this work is described in Methodologies section of Chapter 2 (Page No. 78, Section 2.4.).

3.4.4 Results and Discussions

3.4.4.1 Synthesis and Characterization of monomers (NAG and NAPA) and copolymer (p(NAG-*co*-NAPA)) NPs.

The p(NAG-*co*-NAPA) copolymer NPs was synthesized in two steps, first monomers were synthesized, and then synthesis of copolymer NPs as mentioned in the experimental section. The synthesis of the monomers NAG and NAPA are based on the Schotten-Baumann reaction. In this reaction, the amine group (-NH_2) of amino acids (NAG and NAPA) reacts with acryloyl chloride in an alkaline medium to form an amide bond (-CONH) via nucleophilic substitution by addition-elimination reaction mechanism. In case of NAG, the aqueous phase was acidified then saturated with NaCl, and then extracted from ethyl acetate layer. The ethyl acetate was used as an organic phase in the final washing or extraction that helps in improving the yield percentage of the product. For NAPA synthesis, the hydrochloride salt formed during the reaction, which was removed by absorption of hydrochloric acid by triethylamine, forming triethylamine hydrochloride as a precipitate. Excess salts and unreacted amino acids were further removed by washing the ethyl acetate layer with various salt solutions. The characteristic ^{1}H NMR (500 Hz) bands for NAG and NAPA are given in (**Figure S3.1.2(a)** and **S3.1.3(a)**); ^{13}C NMR are given in (**Figure S3.1.2(b)** and **S3.1.3(b)**) and FTIR spectroscopic bands are given in (**Figure S3.1.4(a)** and **(b)**), which are matching well with our previously reported results.[7, 10] In the second step, the synthesized monomers were used to prepare p(NAG-*co*-NAPA) NPs.

The p(NAG-*co*-NAPA) NPs was achieved through a modified free radical mini-emulsion polymerization method.[39] In this process, a long-chain hexadecane (HD) molecule was used as a co-stabilizer to enhance the stability of the droplets formed during the emulsion process and to prevent Ostwald ripening. The amino acid-based monomers, NAG and/or NAPA, were dispersed

in the oil phase (toluene), resulting in the formation of monomer droplets. AIBN, a radical initiator, that initiate the polymerization at 65-75°C within the oil/monomer droplets and at the interface between the oil/monomer droplets and the aqueous phase. The core was stabilized by crosslinking the monomer droplets with divinyl benzene (DVB), which helps to generate pores and provides mechanical stability to the NPs. DVB acted as a chemical cross-linker, present both within the polymer chains and in between two polymer backbones. Throughout the reaction process, the NAG to NAPA was maintained constant at 1:1 ratio (w/w). Sodium dodecyl sulfate (SDS) was used to prevent coagulation of the particles. This mechanism of copolymer synthesis is straightforward. AIBN initiates the reaction by attacking the hydrogen attached to the terminal sp^2 hybridized primary carbon of NAG, NAPA, and DVB, forming radical ions of both monomers and the cross-linker. These radicals propagate and crosslink the chains, eventually leading to termination when different growing chains meet head-to-head, forming a π bond. The p(NAG-*co*-NAPA) NPs synthesized here is amphiphilic in nature. The carboxylic acid group (-COOH) in NAG imparts the hydrophilic properties of the entire system while the phenyl rings present in NAPA contribute to the hydrophobic characteristics. This arrangement results in a cross-linked network like structure, with the phenyl rings of NAPA and DVB moving towards the core of the micelle and the carboxylic groups oriented towards the outer side. We speculate that this configuration of p(NAG-*co*-NAPA) may facilitate the formation of a dense core of the NPs, along with the formation of small pores on the shell. It can be noted that the NAG and NAPA and the cross-linker DVB can be randomly arranged in the polymeric particles.

The chemical functionalities of p(NAG-*co*-NAPA) NPs were confirmed through ^{1}H NMR, ^{13}C NMR and FTIR, and MALDI-ToF used to measure the molecular weight of the polymers. The positions and number of protons present in the p(NAG-*co*-NAPA) NPs were identified through ^{1}H

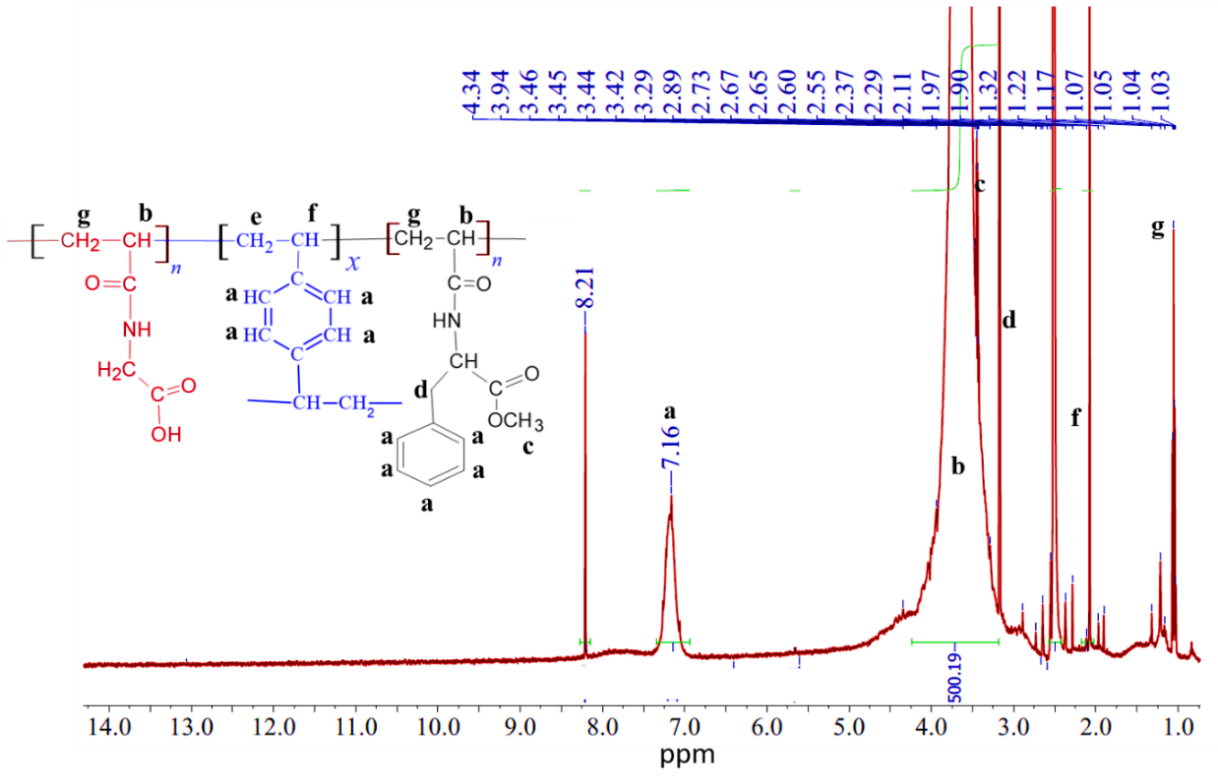

Figure 3.4.1. *^{1}H NMR (500 Hz, $CDCl_3$ and DMSO-d_6) spectra for p(NAG-co-NAPA) NPs performed in (DMSO-d_6 and $CDCl_3$). The inset represents the possible arrangement of NAG, NAPA and DVB in p(NAG-co-NAPA) NPs. The corresponding bands with respect to chemical structure have been mentioned with bold letters in black colour.*

and ^{13}C NMR. The characteristic bands were as follows, ^{1}H-NMR (1:1 ratio of DMSO-d_6 and $CDCl_3$): δ (ppm) = 7.16 (9H, m, aromatic protons), 4.1-3.2 (m, polymer backbone), all other bands in between 4.5- 2.5 showed the presence of aliphatic protons and the absence of bands in between 5 to 6 confirms the successful crosslinking of DVB with alkene by converting all the alkene protons to alkane protons. Further, as the cross linked copolymer is sparingly soluble in NMR solvents, the residual solvent bands were observed at 8.21 and 2.4ppm for $CDCl_3$ and DMSO-d6 respectively (**Figure 3.4.1**); ^{13}C Solid state-NMR (ppm): 175.90 (aromatic), 128.92 (-C=O), and all other bands around 50-30 showed the presence of carbon present in saturated and unsaturated hydrocarbons (polymer backbone) (**Figure S3.4.1**). For a comparison and confirmation of copolymer structure,

we have performed ^{1}H NMR study for copolymer NPs prepared without cross linker in same procedure (**Figure S3.4.2**) which is soluble in DMSO-d_6. **Figure S3.4.2** showed the disappearance of bands in between 5 to 6 ppm which further confirms the conversion all alkene proton to alkane proton. Similar to **Figure 3.4.1**, other than 2.5 band (DMSO-d_6), 2.5 to 4.5 bands represent alkane protons and successful self-crosslinking. FTIR spectra (ATR) revealed the characteristic bands ν (cm^{-1}): 3413 (secondary -NH, s), 3013 (aromatic –CH, s), 2924 and 2846 (alkane –CH, s), 1739 (ester C=O, s), 1659 (-CONH-, s), and 739 (aromatic –CH, b) (**Figure 3.4.2(a)**). For comparison, the FTIR spectra of p(NAG) and p(NAPA) are also presented in **Figure 3.4.2(a)**, demonstrating that distinct bands for both p(NAG) and p(NAPA) coexist in the FTIR spectrum of p(NAG-*co*-NAPA) NPs.

The formation of p(NAG-*co*-NAPA) NPs was confirmed by recording the UV-Vis spectrum, which showed absorption bands at 212nm and 266nm (**Figure 3.4.2(b)**). The band at 212nm corresponds to the π-π* transition, confirming the presence of the carbonyl group in the p(NAG-*co*-NAPA) NPs. The absorption band at 266nm is attributed to the presence of the phenyl rings. MALDI-ToF analysis was performed using dithranol-THF as the matrix to find out the approximate molecular weight of the synthesized copolymer. Since the designed p(NAG-*co*-NAPA) NPs is a complex cross-linked network-like copolymer, the obtained molecular weight ($\bar{M}_w$) represents the chain length between two adjacent crosslinking sites. The heterogeneous fragments in the MALDI-ToF spectrum are indicative of the formation of a random cross-linked block copolymer with a $\bar{M}_w$ ranging from 1251 to 2510Da (**Figure S3.4.3**). The maximum intensity for the p(NAG-*co*-NAPA) NPs is observed at 1357Da, with repeated units varying from 100 to 250Da. The MALDI-ToF analysis revealed two prominent fragments: first at $\bar{M}_w$ = 1419Da, $\bar{M}_n$ = 1357Da, with polydispersity index ($\bar{M}_w$ / $\bar{M}_n$) (PDI) of ~ 1.04, and the second at $\bar{M}_w$= 1655Da, $\bar{M}_n$

= 1595Da with PDI of around 1.03. These chemical functionality-based observations confirm the successful synthesis of p(NAG-*co*-NAPA) NPs.

The results indicated that the formation of the copolymer shifted the thermal degradation temperature to higher values, thereby enhancing the stability of the NPs. The p(NAG-*co*-NAPA) NPs exhibited three distinct weight loss stages, occurring between 102°C and 440°C (**Figure 3.4.2(e)**). Notably, this NPs demonstrates thermal stability at physiological temperature (37°C), The first stage of degradation is attributed to the loss of surface moisture, while the second and

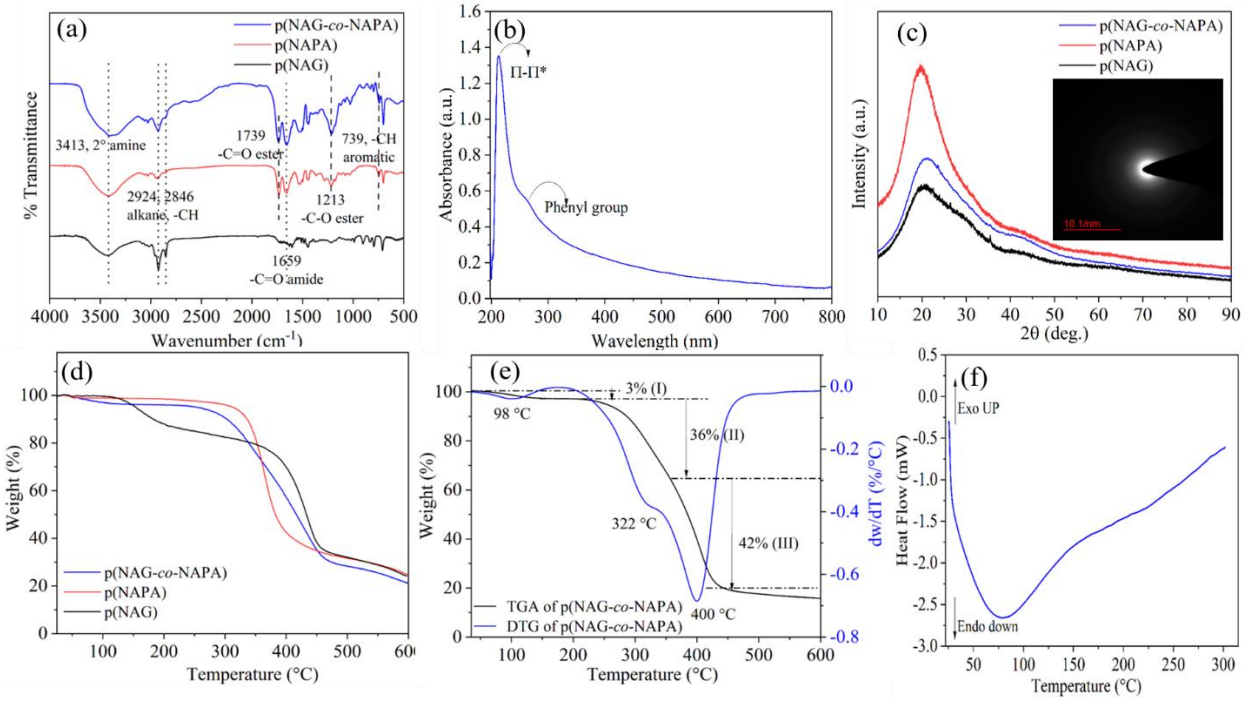

Figure 3.4.2. *Characterizations of p(NAG-co-NAPA) NPs. Fig. (a) FTIR spectra for p(NAG), p(NAPA), and p(NAG-co-NAPA) NPs, (b) UV-Vis spectra for p(NAG-co-NAPA), (c) Powder XRD for p(NAG-co-NAPA), p(NAG), and p(NAPA) and SAED pattern of p(NAG-co-NAPA) (inset image), (d) TGA of p(NAG-co-NAPA), p(NAG), and p(NAPA), (e) TGA and DTG for p(NAG-co-NAPA), and (f) DSC of p(NAG-co-NAPA). The dotted and dash lines drawn in the FTIR spectra represent common bands present in p(NAPA), p(NAG) and p(NAG-co-NAPA) and p(NAPA) and p(NAG-co-NAPA) NPs.*

third stages correspond to the thermal degradation of the polymer chains. Beyond 440°C, the remaining material consists primarily of carbon residues. The DTGA plot for p(NAG-*co*-NAPA) NPs (**Figure 3.4.2(e)**) provides further insights into the degradation temperatures associated with each weight loss stage, with degradation temperatures at 98°C, 322°C, and 400°C. Additionally, to assess thermal phase transitions, DSC of p(NAG-*co*-NAPA) NPs was conducted from RT to 300°C (**Figure 3.4.2(f)**). The analysis revealed a phase transition temperature at 75°C, characterized by an endothermic peak. This phase change is beneficial for drug delivery under physiological conditions. Overall, the thermal stability studies indicate that p(NAG-*co*-NAPA) NPs can be used up to 320°C as a biomaterial for various healthcare applications.

3.4.4.2 Study the morphology and colloidal stability of p(NAG-*co*-NAPA) NPs used as model polymer

According to the synthesis approach, it can be noted that in the p(NAG-*co*-NAPA) NPs, the NAG, NAPA and DVB are randomly arranged. A probable arrangement is shown in the in-set of **Figure 3.4.1**. Further, the shape, particle size, and morphology of p(NAG-*co*-NAPA) NPs were investigated using FESEM, HR-TEM and AFM (**Figure 3.4.3(a-b)** and **S3.4.4**). The FESEM micrographs (**Figure 3.4.3(a)**) confirmed that the p(NAG-*co*-NAPA) NPs are nano-sized and spherical in nature. The dark core and porous shell-like structure observed in **Figure 3.4.3(b)** may be attributed to the presence of hydrophilic carboxylic groups on the outer surface of the particles, forming a corona, while the hydrophobic phenyl rings from the NAPA monomer and DVB are located inside, contributing to the dense core. The diffused ring patterns observed in the selected area electron diffraction (SAED) of p(NAG-*co*-NAPA) NPs (**Figure 3.4.2(c)**) indicated that the particles are amorphous, which aligns with the findings from XRD (**Figure 3.4.2(c)**). The average particle size distribution (**Figure 3.4.3(d)**) calculated from the FESEM image shown in **Figure**

3.4.3(a) indicates a high number of p(NAG-*co*-NAPA) NPs with a diameter ranging from 100nm to 120nm, while the HR-TEM image in **Figure 3.4.3(b)** shows particles with diameter ranging from 120nm to 140nm (**Figure 3.4.3(e)**). Further to assess the roughness of p(NAG-*co*-NAPA) NPs, AFM topography 2d and 3D images were acquired, and revealed that the particles are of the similar size range and the chains are folded with creating some roughness (**Figure S3.4.4(a)** and **(b)**), which may enhance protein binding, cellular internalization, and overall cellular delivery performance.[40] The images from all three microscopic techniques such as FESEM (**Figure 3.4.3(a)**), HR-TEM (**Figure S3.4.4(c)** and **(d)**), and AFM (**Figure S3.4.4(a)**), respectively demonstrated that the p(NAG-*co*-NAPA) NPs are spherical, and porous in nature.

The colloidal stability of p(NAG-*co*-NAPA) NPs was evaluated through measuring the Zeta potential (ζ) and size through Dynamic Light Scattering (DLS) measurements in MilliQ water at room temperature (**Figure 3.4.3(c)** and **(f)**). The ζ of p(NAG-*co*-NAPA) NPs is found to be -44.7mV, indicating good colloidal stability (**Figure 3.4.3(c)**). The hydrodynamic diameter obtained from DLS is ~339.6nm (**Figure 3.4.3(f)**). The increase in the size of p(NAG-*co*-NAPA) NPs can be attributed to the entrapment of water molecules within the porous structure of the NPs and their swelling. To findout the optical and chiral properties of p(NAG-*co*-NAPA) NPs, circular dichroism (CD) spectroscopy was performed in MilliQ water at room temperature. The p(NAPA) exhibited a distinct absorption band at λ_{max} = 233nm, which is characteristic of the optically active NAPA monomer (**Figure 3.4.3(g)**). In contrast, p(NAG) did not show any significant λ_{max}. However, for p(NAG-*co*-NAPA) NPs, a broad band was observed at λ_{max}=222nm (**Figure 3.4.3(g)**).[41, 42] The shift in λ_{max} for p(NAG-*co*-NAPA) NPs towards shorter wavelengths is attributed to the contribution of the DVB molecule present in the NPs. Further analysis of p(NAG-*co*-NAPA) NPs at concentrations ranging from 1000 to 125µg/mL revealed a decrease in the

intensity with decrease in the concentration of NPs, without any change in λ_{max} (**Figure 3.4.3(h)**). This behavior demonstrated the chiral property of the p(NAG-*co*-NAPA) NPs, which can provide insights into NP-drug interactions, design of specific drugs or vaccines, stability, shelf-life, and

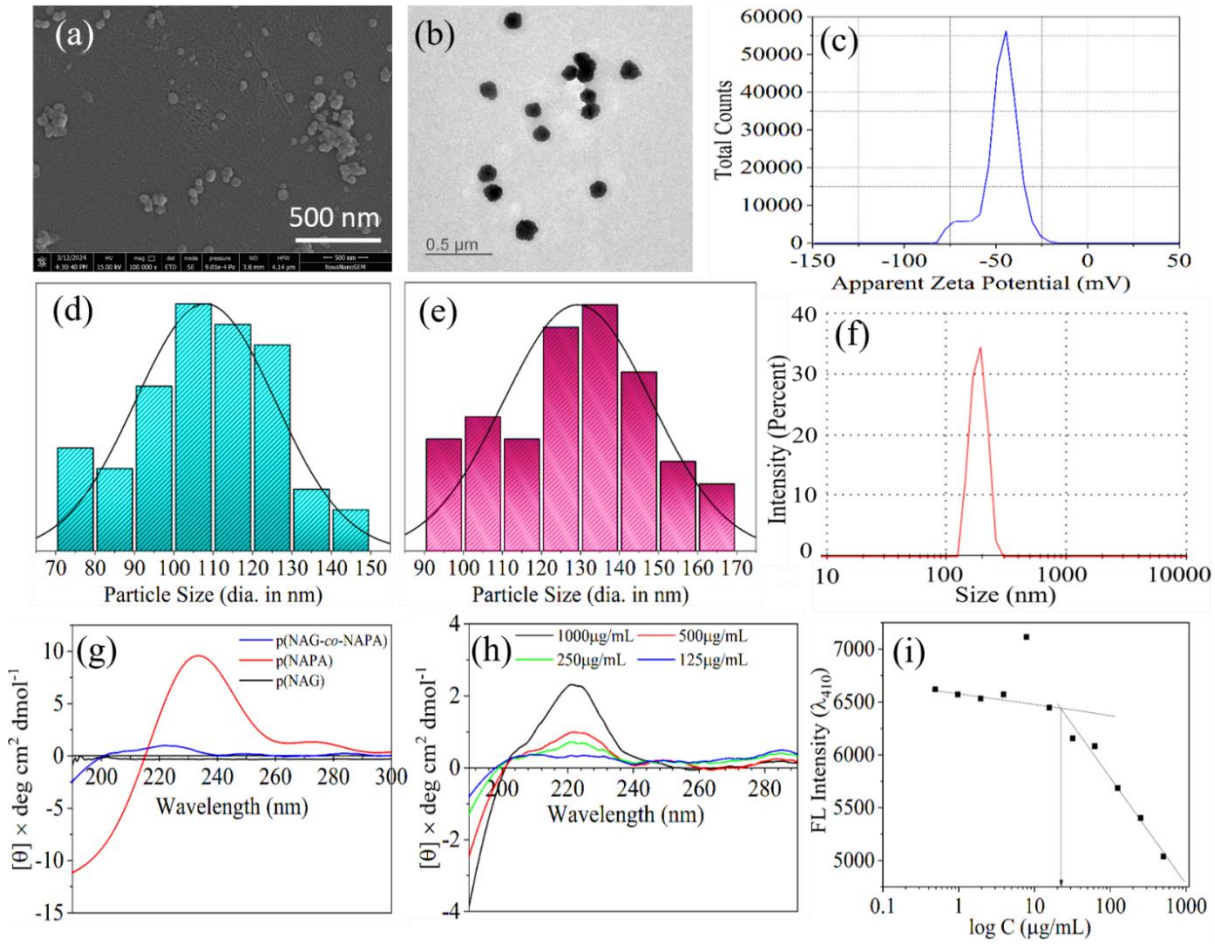

Figure 3.4.3. *Morphology and colloidal stability of p(NAG-co-NAPA) NPs. Fig. (a) and (b) FESEM and HR-TEM image of p(NAG-co-NAPA) NPs at 500nm scale, respectively; (c) zeta potential of p(NAG-co-NAPA), (d) and (e) particle size distribution of Figure 3.4.3(a) and (b), respectively; (f) Hydrodynamic diameter of p(NAG-co-NAPA), (g) and (h) CD spectra of p(NAG-co-NAPA), p(NAG) and p(NAPA) NPs, and serial 2-fold dilutions of p(NAG-co-NAPA) NPs, and (i) CMC of p(NAG-co-NAPA) NPs, where 'C' represents the concentration of NPs.*

The concentration of monomers is crucial during the preparation of polymeric NPs. The critical micelle concentration (CMC) is a colloidal parameter that indicates the minimum concentration required to form a self-assembled structure of NPs in the medium. The CMC is directly related to the size of the NPs and the hydrophobic block present in the system. For a block copolymer to be biocompatible, it is essential to maintain a precise ratio between hydrophobic and hydrophilic weight ratios.[43, 44] In this study, the CMC for p(NAG-*co*-NAPA) NPs is determined to be 8.91μg/mL (**Figure 3.4.3(i)**). This low CMC value indicates that a favorable hydrophobic to hydrophilic ratio is achieved. Consequently, this can lead to the aggregation of p(NAG-*co*-NAPA) NPs in specific media or solvents, as observed in the FESEM, HR-TEM, and AFM images. Furthermore, systems with a low CMC can withstand high degrees of dilution, such as those encountered in the bloodstream, making the NPs biologically more stable.[45]

3.4.4.3 Biocompatibility and hemocompatibilty of p(NAG-*co*-NAPA) NPs.

For biomedical applications, copolymer NPs must demonstrate good biocompatibility and hemocompatibilty. Cellular viability or proliferation in normal cells are crucial parameters. At first, the cell viability for p(NAG) and p(NAPA) have been checked against four normal cell lines, such as L929, Raw 264.7, PC12 and HUVEC cells with PBS as control for concentrations 3.125 to 400μg/mL (**Figure 3.4.4(a)-(d)**). It is observed that p(NAPA) NPs is toxic to the L929 cells at higher concentration whereas at lower concentration it is not toxic (viability is ~100%). For p(NAG) NPs, at higher concentration its' viability is ~100%, whereas at lower concentration (50 to 3.125μg/mL) it is proliferative in nature (~120% viability at 12.5μg/mL) (**Figure 3.4.4(a)**). In case of Raw 264.7 other than 400μg/mL of p(NAG) NPs, for all other concentrations for both the homopolymers showed cell viability is upto ~80% (**Figure 3.4.4(b)**). Further, the cell viability study is performed against PC12 cell and it is observed that, for p(NAPA) and p(NAG) NPs, the

cell viability (%) varied from 57% to 73% and 66% to 55%, respectively (**Figure 3.4.4(c)**). Furthermore, it is observed that p(NAPA) NPs are cytotoxic against HUVEC cells (70% at 5μg/mL), whereas p(NAG) NPs are proliferative in nature (126% at 200μg/mL) (**Figure 3.4.4(d)**). Based on the MTT results, cell viability has been further checked for p(NAG-*co*-NAPA) NPs with same four cell lines (**Figure 3.4.4(e)** and **(f)**). In all four cases, cell viability (%) is observed to be ~100% or above 100%. Interestingly, p(NAPA-*co*-NAG) NPs are showing proliferation for L929 and Raw 264.7 cells at 100 and 50μg/mL (**Figure 3.4.4 (e)** and below 100 μg/mL for HUVEC cells (**Figure 3.4.4(f)**). The decrease in cell viability (%) below 50μg/mL (**Figure 3.4.4(e)**) is due to the contact inhibition experienced by cells in the confined space over 24h. The exact cell viability (%) for p(NAG-*co*-NAPA) NPs against L929 and Raw 264.7 are found to be 78.87±2.96, 89.13±1.49, 114.26±1.33, 105.14±2.07, 102.14±0.97, 96.20±3.43, 97.05±3.63, and 95.55±1.41; and 96.77±1.17, 99.91±3.31, 112.40±2.63, 114.76±0.44, 101.08±1.09, 101.83±1.40, 99.96±2.36, and 101.88±3.38 for 400, 200, 100, 50, 25, 12.5, 6.25, and 3.125μg/mL, respectively, relative to the control group. The cell viability (%) for p(NAG-*co*-NAPA) NPs against HUVEC cells are found to be 84.89±0.74, 86.09±1.70, 104.33±0.92, 105.10±2.46, 111.79±0.58 and 114.36±1.03 for 200, 100, 50, 25,10 and 5μg/mL, respectively, relative to the control group. Interestingly, it can be noted that, for PC12 the cell viability (%) of p(NAG-*co*-NAPA) NPs are highly increased comparing to homopolymer NPs (**Figure 3.4.4(e)**), which is due the presence of both the monomers in copolymer NPs. The cell viability (%) for p(NAG-*co*-NAPA) NPs against PC12 are found to be 97.76±1.61, 99.88±0.47, 98.36±3.41, 97.61±2.11, 96.87±4.01, 98.28±4.27, 96.76±3.42, and 100±2.20 for 400, 200, 100, 50, 25, 12.5, 6.25, and 3.125μg/mL, respectively. These studies clearly indicate that p(NAG-*co*-NAPA) NPs are biocompatible with L929, Raw 264.7, PC12 and HUVEC cells which

demonstrate proliferative nature of NPs at lower concentrations and warranting possible use in *in vivo*.

Hemocompatibilty evaluation is essential for biomaterials designed for therapeutic purposes. For a copolymer to be considered as an effective biomaterial, the hemolysis (%) must remain below 5%. The hemolytic activity of p(NAG-*co*-NAPA) NPs was assessed in a dose- and time-dependent manner for concentrations of 500 to 7.8125µg/mL (**Figure S3.4.5.**). Distilled water used as the positive control, while a pure RBC suspension acted as the negative control. A varied degree of

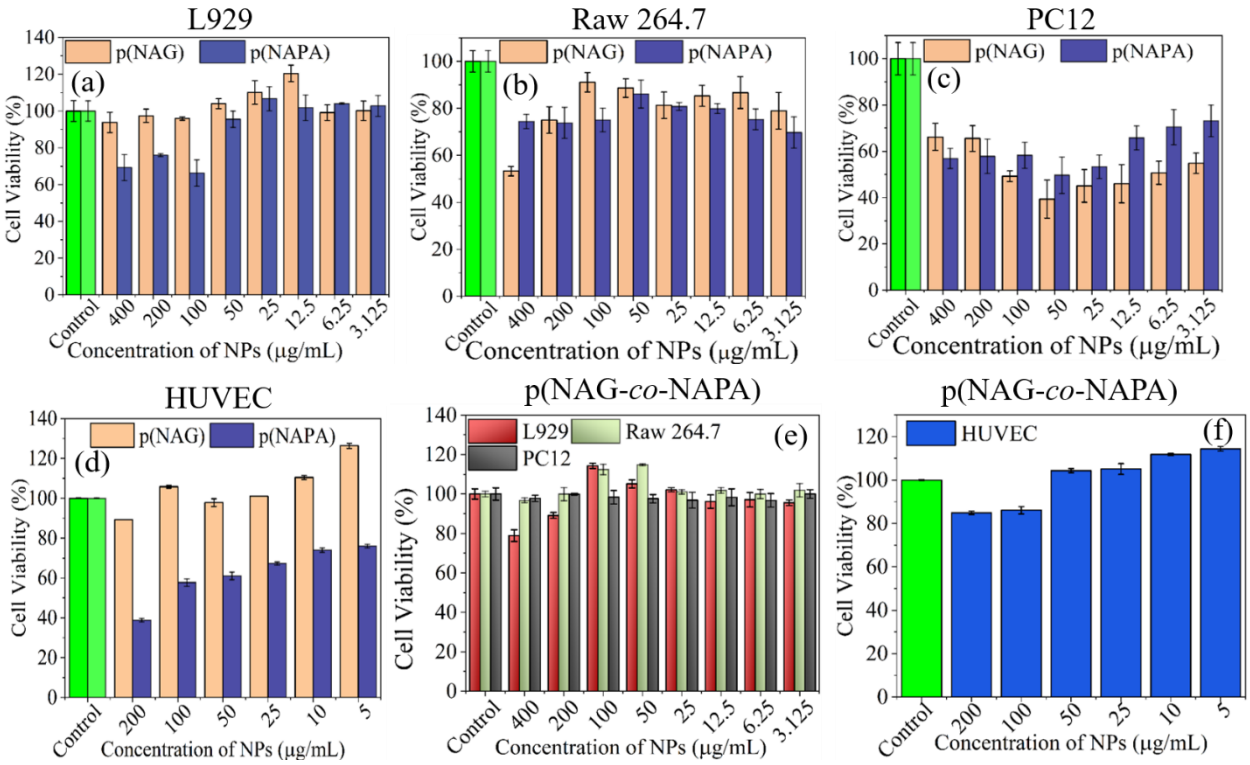

Figure 3.4.4. *Biocompatibility of p(NAG-co-NAPA) NPs. Fig. (a), (b), (c) and (d) Cell viability (%) of p(NAPA) and p(NAG) NPs against L929, Raw 264.7, PC12 and HUVEC cells, respectively; (e) and (f) Cell viability (%) of p(NAG-co-NAPA) NPs in L929, Raw 264.7 and PC12 cell lines and HUVEC cells, respectively. In cell viability case, for p(NAPA) and p(NAG) NPs, calculated p values are provided in supplementary file (see* ***Table S1*** *and* ***Table S2****). For p(NAG-co-NAPA) NPs in all concentrations, against three different cells lines non-significant difference are observed with respect to control whereas for HUVEC cells with respect to control 5 and 200 µg/mL are significant with '*'.*

hemolysis was observed at two different time points (2h and 8h). At 2h, the hemolysis (%) are as follows: 0.97±1.18, 1.06±1.93, 0.47±1.85, 0.53±1.61, 0.71±1.44, 2.01±0.75, and 1.18±1.61 for concentrations of 500, 250, 125, 62.5, 31.25, 15.625, and 7.8125μg/mL, respectively. At 8 h, the hemolysis (%) are 1.77±1.18, 2.95±1.93, 0.35±1.85, 0.77±1.61, 1.07±1.44, 2.56±0.75, and 1.16±1.61 for 500, 250, 125, 62.5, 31.25, 15.625, and 7.8125μg/mL, respectively. The corresponding images of tubes at both time points are provided in the inset of **Figure S3.4.5**. In conclusion, the results indicate that p(NAG-*co*-NAPA) NPs can be regarded as a safe biomaterial concerning hemocompatibilty, demonstrating suitability for therapeutic applications up to 500μg/mL.

3.4.4.4 Angiogenic effect of p(NAG-*co*-NAPA) NPs: studied trough *in ovo* CAM assay

Angiogenic effect of p(NAG), p(NAPA) and p(NAG-*co*-NAPA) NPs are assessed through Image processing tool in both dose and time dependent manner. The selected doses and times were 1, 10 and 100μg and 0, 2, 4, 8 and 24h, respectively by considering PBS as control. The selection of doses is based upon the results obtained from MTT assay (**Figure 3.4.4**). **Figure 3.4.5 (a)-(c)** show the raw images acquired using optical microscope. It is visible that the images consist of blood vessels. The respective segmented images are shown in **Figure 3.4.5 (d)-(e)**. It can be observed that the vascularization and sprouting are found to be more in the segmented images. It is clearly evident that the number of blood vessels are varying with varying the doses and time.

3.4.4.5 Quantitative assessment of angiogenesis through GLCM texture features based image processing tool

At first, three different GLCM textural features such as number of pixels in blood vessels, entropy, and energy of the p(NAG), p(NAPA) and p(NAG-*co*-NAPA) NPs were computed from

the segmented images (**Figure 3.4.6**). It can be noted that the number of pixels in blood vessels and entropy, are directly proportional, while energy is inversely proportional to the growth of blood vessels. Here, the black pixels are representing the blood vessels and white pixels are representing the background. Thus, the increase in black pixel intensity, demonstrates the increase in blood vessels at different conditions. For both the homopolymers, it is observed that due to positive change in slope at all three concentrations over the concerned time periods, they are angiogenic in nature. For p(NAG), 1µg dose is showing better blood vessel growth over a 10µg

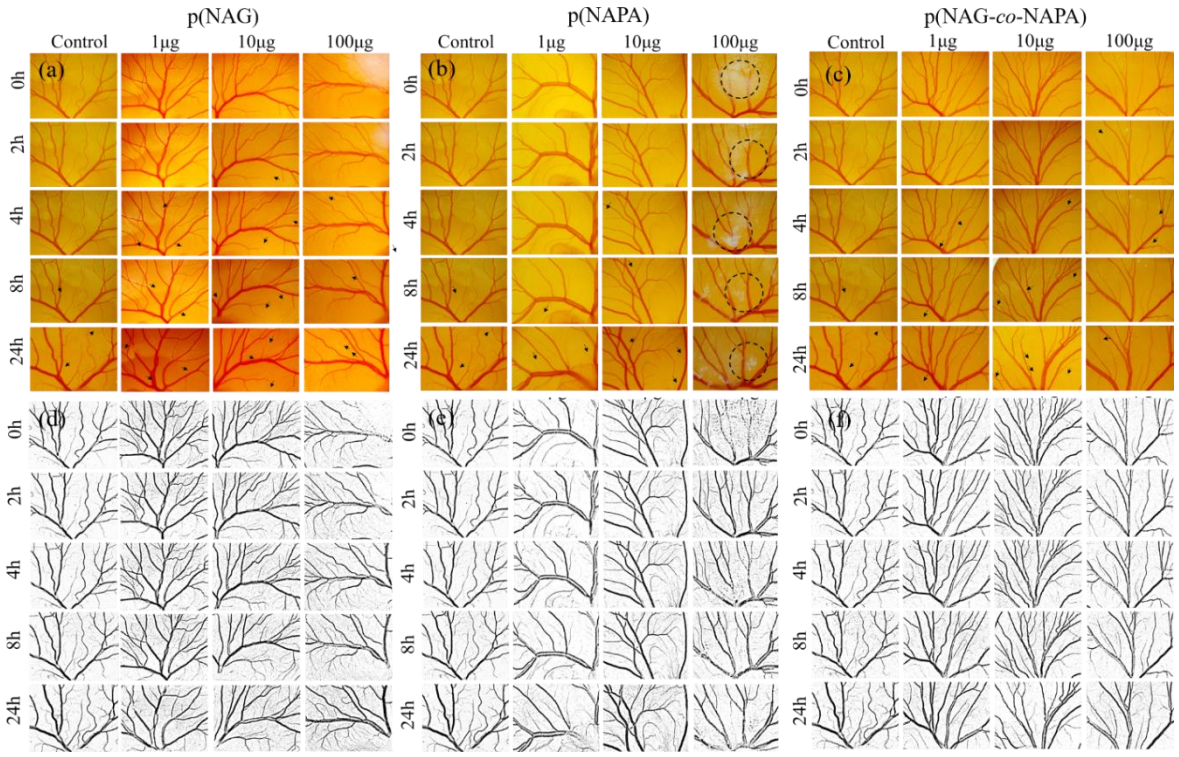

Figure 3.4.5. *Represents the microscopic images and binary images obtained after segmentation of blood vessels for p(NAG), p(NAPA) and p(NAG-co-NAPA) NPs with three different doses (1, 10 and 100µg) with control sample at five different time intervals (0, 2, 4, 8 and 24h). Fig. (a), (b) and (c) represents the raw images and (d), (e) and (f) represent the binary images after segmentation corresponding to (a), (b) and (c). The black arrows inside the microscopic images (a, b and c) represent the visual changes in images over dose and time. The black dashed circle drawn in p(NAPA) in 100µg dose represents the position where sample was added during the experiment.*

dose (**Figure 3.4.6(a)**). Whereas for p(NAPA) homopolymer (**Figure 3.4.6(b)**), 10µg dose is showing better angiogenic nature compared to the 1µg dose. For 100µg dose, p(NAG) is more angiogenic as compared to the p(NAPA) NPs. Similarly, in the case of p(NAG-*co*-NAPA) NPs, a positive change in slope is observed for all three concentrations over the time period. Although for

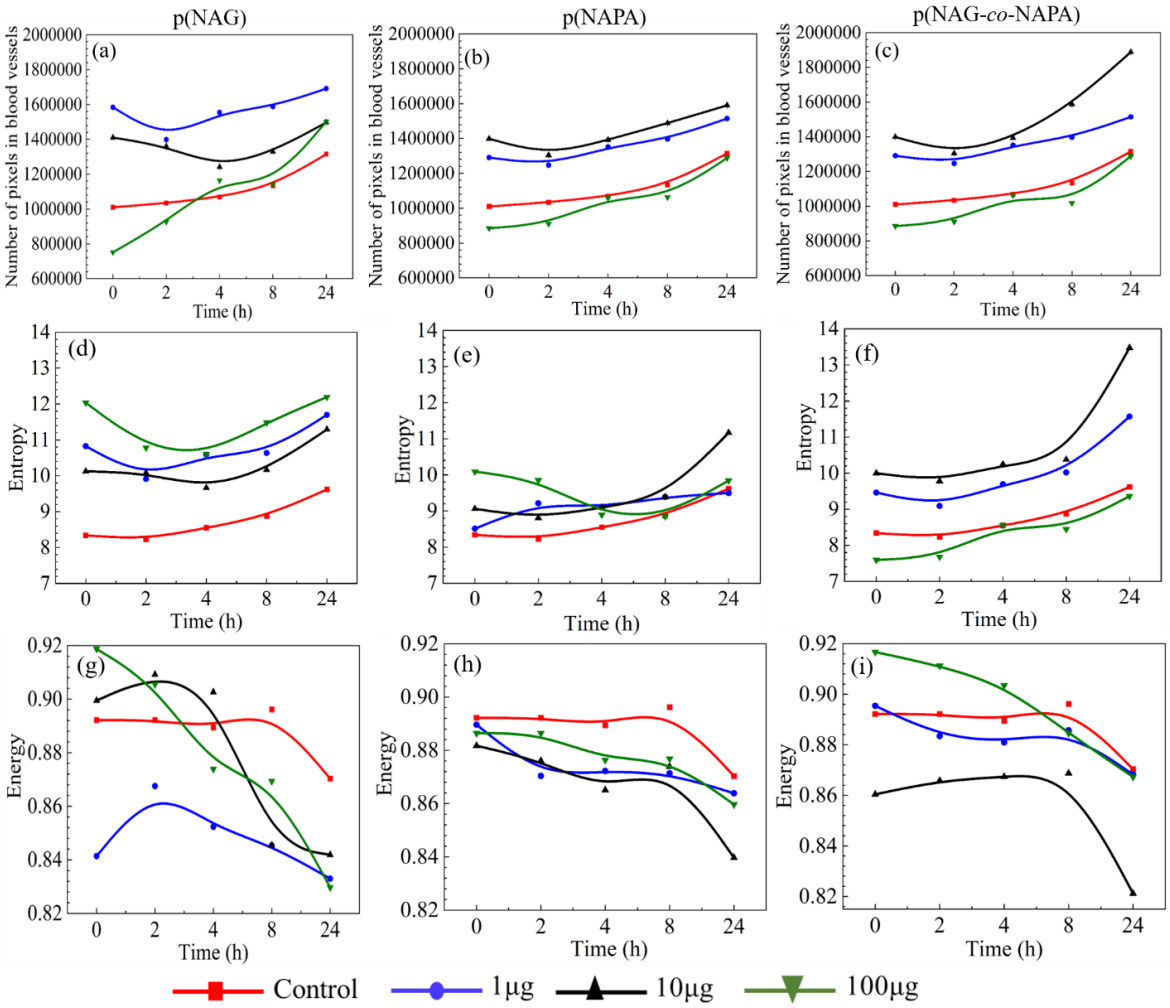

Figure 3.4.6. *Represents the three textural features extracted from GLCM based matrix. Fig. (a), (b) and (c) demonstrate the number of pixels in blood vessels; (d), (e) and (f) demonstrate the entropy; and (g), (h) and (i) demonstrate the energy for p(NAG), p(NAPA) and p(NAG-co-NAPA) NPs with three different doses (1, 10 and 100µg) with control sample at five different time intervals (0, 2, 4, 8 and 24h), respectively. The error % values are lying in between 10% and a corresponding Tables are provided in the supplementary file (see* ***Table S3****,* ***Table S4*** *and* ***Table S5****).*

1 and 10µg doses, no such huge change is observed upto 8h. Interestingly, for 10µg dose at 24h a sudden change in black pixel count from ~1600000 to ~1888000 is observed (**Figure 3.4.6(c)**). This change in black pixel count demonstrates the pro-angiogenic behavior of p(NAG-*co*-NAPA) NPs.

In case of entropy, an increasing trend is observed for the time period of 0 to 24h in three different conditions (**Figure 3.4.6(d)-(f)**). Entropy means the change in randomness of the system, which means, increase in randomness employs that more vessels are formed. It is evident that the entropy is high at 1,10 and 100µg doses compared to the control for homopolymer NPs. Therefore, the angiogenesis is promoted by the considered doses of homopolymers. However, the entropy is varying for homopolymers and copolymer NPs. In case of p(NAG), the entropy is lying above the control group, whereas for p(NAPA), the entropy for all three doses are closed to the control sample (**Figure 3.4.6(d)** and **(e)**). Whereas, in case of p(NAG-*co*-NAPA) NPs, for 100µg the entropy is lying below the control sample, however, for 1 and 10µg doses, the entropy present over the control value. At 10µg dose, at 24h, a sudden rise in entropy value is observed from ~10.5 to ~13.5 (**Figure 3.4.6(f)**). These results further depict the proangiogenic nature of the copolymer NPs. Similarly, for energy, a decreasing trend is observed for all doses of homopolymer NPs over the entire time period (**Figure 3.4.6(g)** and **(h)**). It can also be noted that, for p(NAG) NPs at 10 and 100µg doses, a sudden change in slope is observed (**Figure 3.4.6(g)**), which demonstrates the prominent angiogenic nature of the p(NAG) NPs compared to the p(NAPA) homopolymer. However, for copolymer NPs, a quick fall in energy value from 0.86 (8h) to 0.82 (24h) is observed at 10µg dose. (**Figure 3.4.6(i)**).

Figure 3.4.7 shows two more texture features such as mean and contrast, which are computed for deeper understanding of the angiogenic behavior of homopolymer and copolymer NPs. According

to the definition, mean is inversely proportional and contrast is directly proportional to the blood vessels development. In case of mean, for p(NAG) NPs, at 10 and 100µg doses a negative change in slope is observed, whereas for p(NAPA), with change in the change in slope are noticed, however, not a prominent change in mean is observed. For p(NAG-*co*-NAPA) NPs, mean value is decreased from 223 to 219 for 10µg dose at 24h (**Figure 3.4.7(a)-(c)**). Further, for contrast, all three considered NPs at concerned doses are showing an increasing trend upto 24h, however the values obtained are lower compared to the control sample (**Figure 3.4.7(d)-(f)**). For p(NAG-*co*-NAPA) at 10µg dose, a sharp rise in contrast value is observed from 8h to 24h i.e.; 2859.2 to

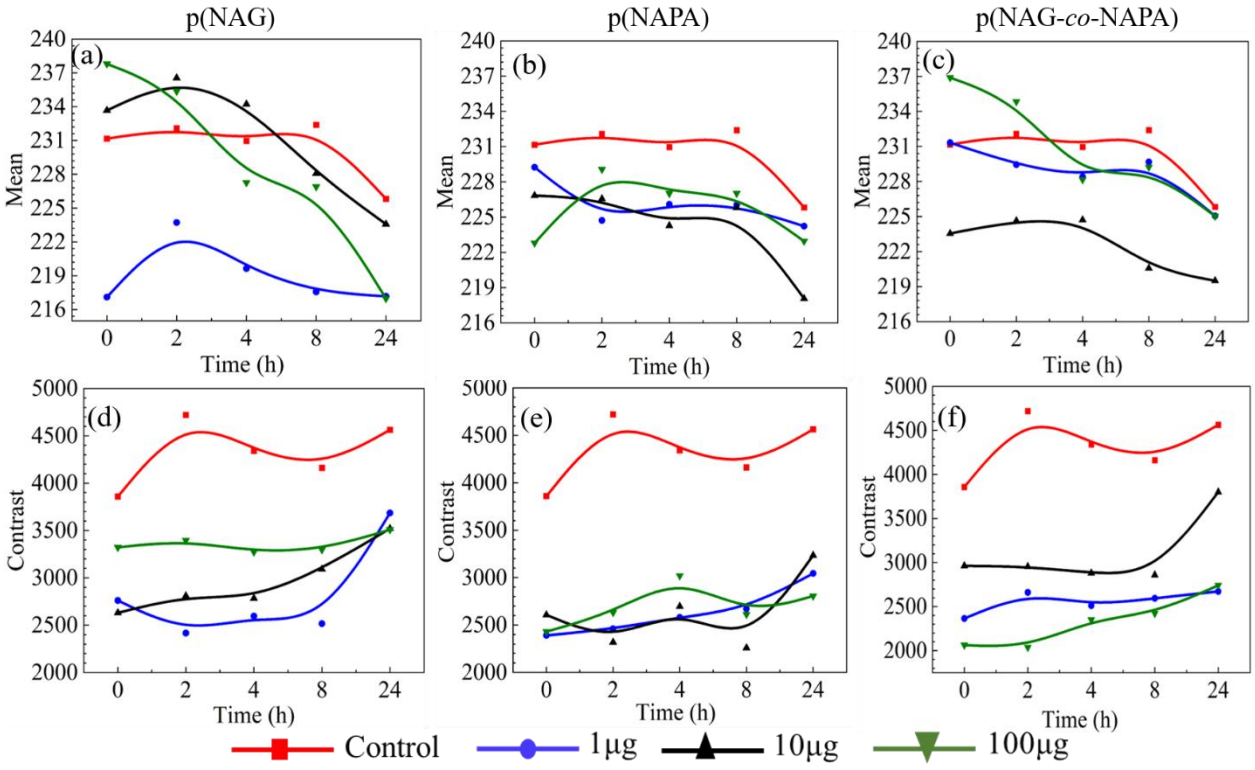

Figure 3.4.7. *Represents the two textural features extracted from GLCM. Fig. (a), (b) and (c) demonstrate Mean and (d), (e) and (f) demonstrate Contrast for p(NAG), p(NAPA) and p(NAG-co-NAPA) NPs with three different doses (1, 10 and 100µg) with control sample at five different time intervals (0, 2, 4, 8 and 24h), respectively. The error % are calculated and varying upto 10% (see* ***Table S6*** *and* ***Table S7****).*

3800.6 (**Figure 3.4.7(f)**), which further confirms that, 10µg dose of copolymer NPs can be an optimum dose for promoting angiogenesis. Furthermore, it can be stated that, Mean and contrast are corroborating well with the results obtained for number of pixels in blood vessels, entropy, and energy in the earlier section (**Figure 3.4.6**).

Along with above mentioned five texture parameters, two more parameters such as dissimilarity and variance are computed and represented in **Figure 3.4.8 ((a)-(c)** and **(d)-(f))**, respectively. The

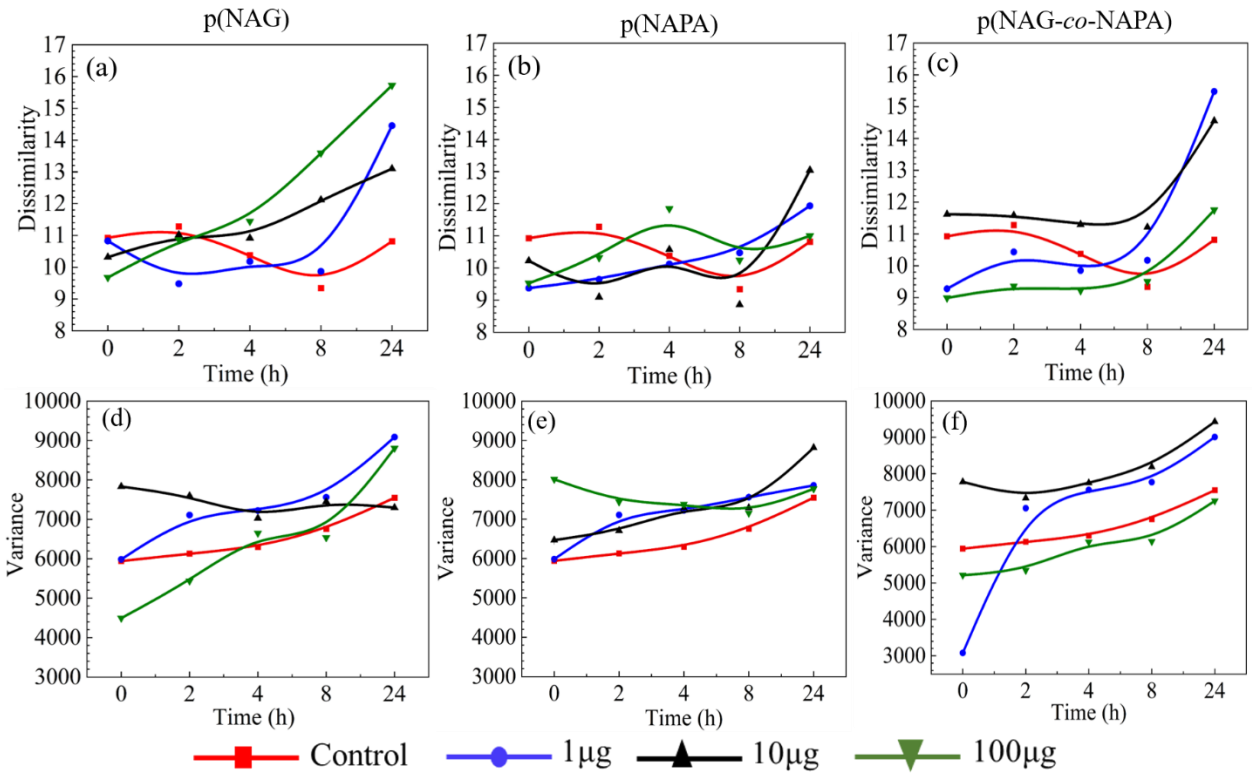

Figure 3.4.8. *Represents the two textural features extracted from GLCM based matrix. Fig. (a), (b) and (c) demonstrate dissimilarity and (d), (e) and (f) demonstrate variance for p(NAG), p(NAPA) and p(NAG-co-NAPA) NPs with three different doses (1, 10 and 100µg) with control sample at five different time intervals (0, 2, 4, 8 and 24h), respectively. The error% values are obtained upto 10% (see* ***Table S8*** *and* ***Table S9****).*

positive change in slope for both the parameters represent angiogenic nature of the NPs. In case of dissimilarity, for p(NAG) at all three concentrations, increase in dissimilarity values are observed, whereas for p(NAPA) all doses are showing negligible variation among them with respect to control (**Figure 3.4.8(a)** and **(b)**). However, for p(NAG-*co*-NAPA) NPs both 1μg and 10μg doses are showing sharp increase in the dissimilarity index (**Figure 3.4.8(c)**). Similarly, with varying time and doses an increase in the variance values are observed for all three NPs (**Figure 3.4.8 (d**)-(f)). The variance of an image refers to a statistical measure that quantifies the dispersion or spread of pixel intensity values within an image. Particularly, for p(NAG-*co*-NAPA) NPs for 10μg dose variance is increased from ~8000 to ~9400, while for p(NAPA) and p(NAG) the values are obtained to be 8816.9 and 7295.4 at 24h, respectively. It can be concluded that, both dissimilarity and variance results for p(NAG-*co*-NAPA) NPs are matching well with the above five texture parameters and demonstrating the proangiogenic nature of copolymer NPs at 10μg dose. Furthermore, it can be highlighted that, the textural features obtained from *in ovo* models are fitting well with the *in vitro* cell based results of the copolymer NPs.

3.4.4.6 Validation of GLCM texture feature-based image processing results with Angiotool through Tube formation assay.

Further, to check the accuracy of the GLCM texture feature-based image processing tool for angiogenesis study, tube formation assay is conducted in HUVEC cells by considering p(NAG-*co*-NAPA) NPs as a model polymer. Three different concentrations (1, 10, and 100μg) of NPs, are treated with HUVEC cells for 6h, and subsequently, microscopic images were acquired (**Figure 3.4.9(a-h)**). No any treatment with NPs is considered as a control group. It is clearly evident that, compared to the control for 1μg dose, a fewer tube is formed (**Figure 3.4.9(e)** and **(f)**), whereas for 10μg dose defined and thick network or mesh like structures are formed (**Figure 3.4.9(e**) and **(g)**).

For 100µg dose, the p(NAG-*co*-NAPA) NPs is showing less angiogenic or toxic to the cells where disconnected patchy dead cell structures or thin tubes are observed (**Figure 3.4.9(d)** and **(h)**). Additionally, the quantitative analysis is performed using two methods: (1) Angiotool with ImageJ (conventional) and (2) GLCM texture feature-based Image processing tool. From angiotool data, it is found that for 10µg dose, explant area, total vessel length, and total number of junctions

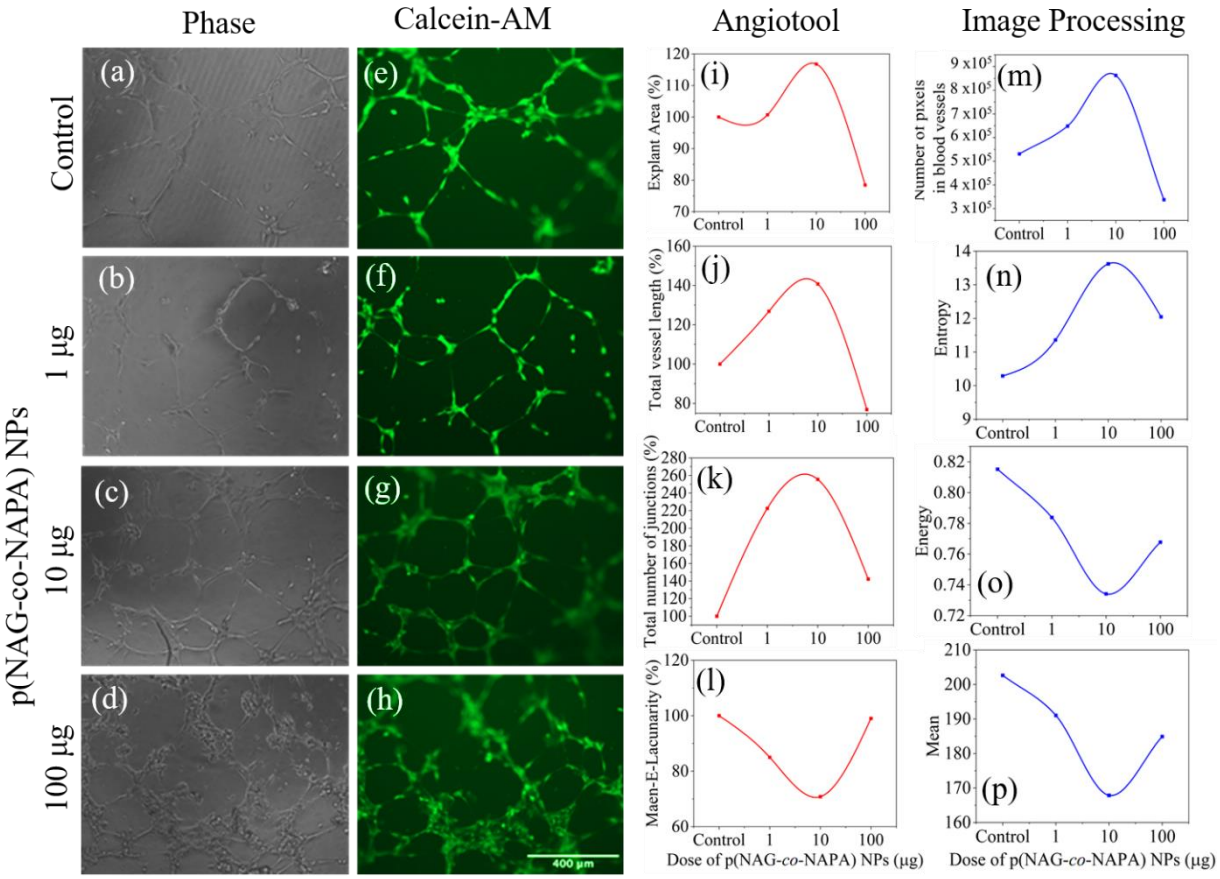

Figure 3.4.9. *Dose dependent tube formation properties of p(NAG-co-NAPA) NPs. Fig. (a-d) and (e-h) represent bright field and calcein-am stained microscopic images of HUVEC cells treated with three different concentration of p(NAG-co-NAPA) NPs at 6h (scale bar: 400 µm); (i) explant area (%), (j) total vessel length (%), (k) total number of junctions (%), (l) mean-e-lacunarity (%) calculated by Angiotool and (m) number of pixels in blood vessels, (n) entropy, (o) energy and (p) mean calculated by GLCM texture features based Image processing tool respectively for obtained microscopic images (e-h) from tube formation assay. The corresponding error% values are provided in supplementary (**Table S10** and **Table S11**).*

are increasing with respect to 1 and 100µg doses, whereas mean-e-lacunarity or empty space is less for 10µg dose as compared to 1 and 100µg doses (**Figure 3.4.9(i)-(l)**). Similarly, the quantitative data obtained from the Image processing tool demonstrate that the number of pixels in blood vessels and entropy are highest for the 10µg dose, whereas energy and mean are lowest as compared to 1 and 100µg dose. From these results it can be conclude that 10µg dose of p(NAG-*co*-NAPA) NPs is optimum for promoting angiogenesis, which is corroborated well with results obtained from the previous experiments. Thus, Image processing tool with GLCM texture feature is an alternative solution for the angiogenesis analysis of microscopic images, which can eliminate the shortcomings associated with Angiotool and/or other reported approaches.

In this work, successfully p(NAG-*co*-NAPA) NPs has been synthesized through mini emulsion polymerization as a modelled polymer to develop a standard tool for assessing angiogenesis. Angiogenesis, the process of new blood vessel formation is associated with the treatment of various diseases which can be controlled by the addition of biopolymers such as p(NAG), p(NAPA) and p(NAG-*co*-NAPA) NPs.[4] Anti-angiogenic molecules are used for treating cancer and eye diseases, while polymers for neovascularization promotes the wound healing efficiency. Additionally, the stimulation of angiogenesis is beneficial for stroke recovery. As a result, the need for analysing angiogenesis has gained significant momentum in the biomedical and health care technology.[46, 47] Accurate assessment of angiogenesis with doses and time could solve the issues related to the drug discovery and regenerative medicine. However, the manual quantification of 3D morphology of reconstituted vasculature using imaging software such as ImageJ, CellProfiler or Angiotool have their own limitations such as manual analysis process, uneven illumination, noise robustness and loss in fine structures during segmentation etc.[12, 16, 48] Furthermore, the

subjective opinions of analysts may introduce bias into the results.[49] Therefore, the present study possesses important direction for the dose and time dependent treatment by using polymeric materials for analysing the angiogenesis properties through GLCM based texture analysis approach.[50, 51]

Thus through this work, after confirmation of particle size, shape, colloidal stability and structure, their biocompatibility and hemocompatibility were studied (**Figure 3.4.1** to **Figure 3.4.3**). It's biocompatibility (~120%) against four normal cells including HUVEC (**Figure 3.4.4(e)** and **(f)**) and hemocompatibilty (<5%) (**Figure 3.4.4(f)**) results of the copolymer revealed that the synthesized p(NAG-*co*-NAPA) NPs could have the potential use in therapeutic applications. The cell viability results against L929, Raw 264.7 and HUVEC cells have revealed the proliferative nature of p(NAG-*co*-NAPA) NPs. Further to achieve the main aim of this work, angiogenesis or CAM assay and tube formation assay have been performed in *in ovo* and *in vitro* models followed by data analysis with image processing tools (Adoptive threshold algorithm with GLCM features) and conventional Angiotool (**Figure 3.4.6** to **Figure 3.4.9**).

By using GLCM texture based analysis, seven different features have been extracted for p(NAG), p(NAPA) and p(NAG-*co*-NAPA) NPs in dose and time dependent manner. The features studied here are listed as number of pixels in blood vessels, entropy, energy, mean, contrast, dissimilarity and variance. All the features clearly demonstrate the angiogenic behavior of all three polymer NPs synthesized at the concerned doses (**Figure 3.4.6** to **Figure 3.4.8**). However, angiogenesis depends on the concentrations of p(NAG), p(NAPA) and p(NAG-*co*-NAPA) NPs used during the treatment and period of treatment (**Figure 3.4.6** to **Figure 3.4.8**). To compare and validate the results obtained from Image processing tools, tube formation assay is also conducted in HUVEC

cells by considering p(NAG-*co*-NAPA) NPs as a modelled polymer (**Figure 3.4.9**). Interestingly, it is found that both analysis method, i.e., Angiotool and Image processing tool demonstrated similar results that 10µg dose of modelled polymer as an optimum dose for promoting angiogenesis. This is further matching well with the texture feature based analysis of angiogenesis images obtained from *in ovo* studies. Additionally, a box chart has been represented for better comparison and understanding of the optimal dose for treatment and biomedical applications of the synthesized polymer NPs (**Figure 3.4.10**). Thus, it can be stated that the Image processing tool can be considered as a gold standard for quantitative assessment of angiogenesis and can be concluded that compared to homopolymers, copolymer NPs possess better angiogenic properties and hold potential for various regenerative applications, including wound management.

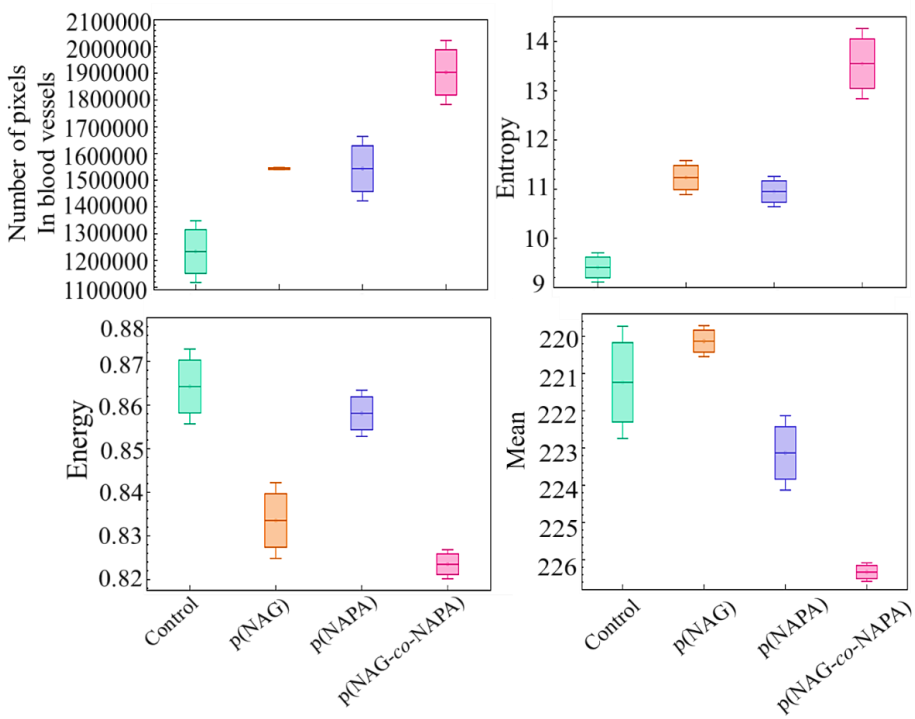

Figure 3.4.10. *Represents the significant change in textural features obtained from segmented images during the in ovo based angiogenesis study. Fig. (a) number of pixels in blood vessels, (b) entropy, (c) energy, and (d) mean for p(NAG), p(NAPA) and p(NAG-co-NAPA) NPs with the treatment of 10µg dose at 24h.*

3.4.5 Summary and Conclusions for this part

Despite significant advancements in the development of angiogenesis assessment tools, a fully reliable and automated quantifying method remains elusive. In this light, the present work has developed an angiogenesis evaluation tool based on GLCM features that is straight forward and physiologically relevant. To establish this method, an amino acid based copolymer p(NAG-*co*-NAPA) NPs has been synthesized as a modelled polymer. As anticipated, hemolysis and *in vitro* viability assays with various cells including HUVEC, revealed the biocompatible and proliferative nature of the NPs. The dose and time-dependent angiogenic properties of p(NAG-*co*-NAPA) NPs have been computed from microscopic images obtained from *in ovo* model and tube formation assay using GLCM texture features based Image processing tool. As a comparison, further tube formation results are cross-verified with Angiotool analysis. Both tools depict that a 10μg dose of p(NAG-co-NAPA) NPs can be an optimum dose for promoting angiogenesis. This finding resembles that the application of Image processing tool in wet-lab provides an un-biased and high throughput analysis of various texture based features from 2D microscopic images over existing conventional tools. However, to comprehend the efficacies of p(NAG-*co*-NAPA) NPs and to make GLCM texture features based Image processing tool as a gold standard for the analysis of angiogenesis, *in vivo* studies have been taken under consideration as a future scope of this work.

3.4.6. References

1. Jain, R.K., *Molecular regulation of vessel maturation.* Nature Medicine, 2003. **9**(6): p. 685-693.
2. Wimmer, R.A., et al., *Generation of blood vessel organoids from human pluripotent stem cells.* Nature Protocols, 2019. **14**(11): p. 3082-3100.
3. Lee, J.-H., et al., *Materials roles for promoting angiogenesis in tissue regeneration.* Progress in Materials Science, 2021. **117**: p. 100732.

4. Nsiah, B.A., et al., *8 - Angiogenesis in hydrogel biomaterials*, in *Biosynthetic Polymers for Medical Applications*, L. Poole-Warren, P. Martens, and R. Green, Editors. 2016, Woodhead Publishing. p. 189-203.
5. Carmeliet, P., *Angiogenesis in life, disease and medicine.* Nature, 2005. **438**(7070): p. 932-936.
6. Smith, S.K., *Angiogenesis and reproduction.* British Journal of Obstetrics and Gynaecology, 2001. **108**(8): p. 777-783.
7. Gupta, P.S., et al., *In vivo potential of polymeric N-acryloyl-glycine nanoparticles with anti-inflammatory activities for wound healing.* Materials Advances, 2023. **4**(20): p. 4718-4731.
8. Wasnik, K., et al., *Neurogenic and angiogenic poly(N-acryloylglycine)-co-(acrylamide)-co-(N-acryloyl-glutamate) hydrogel: preconditioning effect under oxidative stress and use in neuroregeneration.* Journal of Materials Chemistry B, 2024. **12**(25): p. 6221-6241.
9. Gupta, P.S., et al., *Nitric oxide releasing novel amino acid-derived polymeric nanotherapeutic with anti-inflammatory properties for rapid wound tissue regeneration.* Nanoscale, 2024. **16**(4): p. 1770-1791.
10. Wasnik, K., et al., *Poly(N-acryloylglycine-acrylamide) Hydrogel Mimics the Cellular Microenvironment and Promotes Neurite Growth with Protection from Oxidative Stress.* ACS Applied Bio Materials, 2023. **6**(12): p. 5644-5661.
11. Adair TH, M.J.A.S.R.C., *Overview of Angiogenesis*. 2010.
12. Rahman, H.S., et al., *An Overview of In Vitro, In Vivo, and Computational Techniques for Cancer-Associated Angiogenesis Studies.* BioMed Research International, 2020. **2020**(1): p. 8857428.
13. Carpentier, G., et al., *Angiogenesis Analyzer for ImageJ — A comparative morphometric analysis of "Endothelial Tube Formation Assay" and "Fibrin Bead Assay".* Scientific Reports, 2020. **10**(1): p. 11568.
14. Aschauer, J., et al., *Non-invasive quantification of corneal vascularization using anterior segment optical coherence tomography angiography.* Scientific Reports, 2024. **14**(1): p. 2124.
15. Yanagisawa, H., M. Sugimoto, and T. Miyashita, *Mathematical simulation of tumour angiogenesis: angiopoietin balance is a key factor in vessel growth and regression.* Scientific Reports, 2021. **11**(1): p. 419.
16. Pereira, M., et al. *A Comprehensive Look at In Vitro Angiogenesis Image Analysis Software*. International Journal of Molecular Sciences, 2023. **24**, DOI: 10.3390/ijms242417625.
17. Gutknecht, M.F., et al., *Identification of the S100 fused-type protein hornerin as a regulator of tumor vascularity.* Nature communications, 2017. **8**(1): p. 552.
18. Corliss, B.A., et al., *Reaver: a program for improved analysis of high-resolution vascular network images.* Microcirculation, 2020. **27**(5): p. e12618.
19. Cervantes, J., et al., *A comprehensive survey on segmentation techniques for retinal vessel segmentation.* Neurocomputing, 2023. **556**: p. 126626.
20. Tian, Y., et al., *A Vessel Active Contour Model for Vascular Segmentation.* BioMed Research International, 2014. **2014**(1): p. 106490.
21. Wiharto, W. and E. Suryani, *The comparison of clustering algorithms K-means and fuzzy C-means for segmentation retinal blood vessels.* Acta Informatica Medica, 2020. **28**(1): p. 42.

22. Armi, L. and S. Fekri-Ershad, *Texture image analysis and texture classification methods-A review.* arXiv preprint arXiv:1904.06554, 2019.
23. Peirce, S.M., *Computational and Mathematical Modeling of Angiogenesis.* Microcirculation, 2008. **15**(8): p. 739-751.
24. Hao, X., et al., *Peptide functionalized biomimetic gene complexes enhance specificity for vascular endothelial regeneration.* Colloids and Surfaces B: Biointerfaces, 2024. **241**: p. 114020.
25. Hao, X., et al., *Bovine serum albumin-based biomimetic gene complexes with specificity facilitate rapid re-endothelialization for anti-restenosis.* Acta Biomaterialia, 2022. **142**: p. 221-241.
26. Xu, Q., et al., *Polyethylenimine-modified graphene quantum dots promote endothelial cell proliferation.* Regenerative Biomaterials, 2024. **11**.
27. Rai, V., R. Moellmer, and D.K. Agrawal, *Stem Cells and Angiogenesis: Implications and Limitations in Enhancing Chronic Diabetic Foot Ulcer Healing.* Cells, 2022. **11**(15): p. 2287.
28. Mastrullo, V., et al., *Angiogenesis in Tissue Engineering: As Nature Intended?* Frontiers in Bioengineering and Biotechnology, 2020. **8**.
29. Li, J., et al., *A Dual Peptide Sustained-Release System Based on Nanohydroxyapatite/Polyamide 66 Scaffold for Synergistic-Enhancing Diabetic Rats' Fracture Healing in Osteogenesis and Angiogenesis.* Frontiers in Bioengineering and Biotechnology, 2021. **9**.
30. Li, M., Y. Wu, and L. Ye *The Role of Amino Acids in Endothelial Biology and Function*. Cells, 2022. **11**, DOI: 10.3390/cells11081372.
31. Oberkersch, R.E. and M.M. Santoro, *Role of amino acid metabolism in angiogenesis.* Vascular Pharmacology, 2019. **112**: p. 17-23.
32. Wang, Z., et al., *L-phenylalanine attenuates high salt-induced hypertension in Dahl SS rats through activation of GCH1-BH4.* PLOS ONE, 2021. **16**(4): p. e0250126.
33. Heikal, L., et al., *l-Phenylalanine Restores Vascular Function in Spontaneously Hypertensive Rats Through Activation of the GCH1-GFRP Complex.* JACC: Basic to Translational Science, 2018. **3**(3): p. 366-377.
34. Tan, R., et al., *Phenylalanine induces pulmonary hypertension through calcium-sensing receptor activation.* American Journal of Physiology-Lung Cellular and Molecular Physiology, 2020. **319**(6): p. L1010-L1020.
35. Welsh, P., et al., *Circulating amino acids and the risk of macrovascular, microvascular and mortality outcomes in individuals with type 2 diabetes: results from the ADVANCE trial.* Diabetologia, 2018. **61**(7): p. 1581-1591.
36. Amin, K., et al., *Dietary glycine inhibits angiogenesis during wound healing and tumor growth.* Cancer biology & therapy, 2003. **2**(2): p. 173-178.
37. Rose, M.L., et al., *Dietary glycine inhibits the growth of B16 melanoma tumors in mice.* Carcinogenesis, 1999. **20**(5): p. 793-798.
38. Guo, D., et al., *Vascular endothelial growth factor signaling requires glycine to promote angiogenesis.* Scientific Reports, 2017. **7**(1): p. 14749.
39. Yamala, A.K., et al., *Poly-N-acryloyl-(l-phenylalanine methyl ester) hollow core nanocapsules facilitate sustained delivery of immunomodulatory drugs and exhibit adjuvant properties.* Nanoscale, 2017. **9**(37): p. 14006-14014.

40. Wang, X., et al., *Spike nanoparticles: From design to biomedical applications.* Next Materials, 2024. **2**: p. 100080.
41. Werber, L., et al., *Isothermal titration calorimetry of chiral polymeric nanoparticles.* Chirality, 2015. **27**(9): p. 613-618.
42. Amdursky, N. and M.M. Stevens, *Circular Dichroism of Amino Acids: Following the Structural Formation of Phenylalanine.* ChemPhysChem, 2015. **16**(13): p. 2768-2774.
43. Lu, Y., et al., *Strategies to improve micelle stability for drug delivery.* Nano Research, 2018. **11**(10): p. 4985-4998.
44. Kim, S., et al., *Overcoming the barriers in micellar drug delivery: loading efficiency, in vivo stability, and micelle–cell interaction.* Expert Opinion on Drug Delivery, 2010. **7**(1): p. 49-62.
45. Rideau, E., et al., *Liposomes and polymersomes: a comparative review towards cell mimicking.* Chemical Society Reviews, 2018. **47**(23): p. 8572-8610.
46. Carmeliet, P. and R.K. Jain, *Molecular mechanisms and clinical applications of angiogenesis.* Nature, 2011. **473**(7347): p. 298-307.
47. Ergul, A., A. Alhusban, and S.C. Fagan, *Angiogenesis.* Stroke, 2012. **43**(8): p. 2270-2274.
48. AlMalki, W.H., et al., *Assessment methods for angiogenesis and current approaches for its quantification.* Indian Journal of Pharmacology, 2014. **46**(3).
49. Webb, S., *Deep learning for biology.* Nature, 2018. **554**(7693): p. 555-557.
50. Nanni, L., et al., *Different approaches for extracting information from the co-occurrence matrix.* PloS one, 2013. **8**(12): p. e83554.
51. Mohanaiah, P., P. Sathyanarayana, and L. GuruKumar, *Image texture feature extraction using GLCM approach.* International journal of scientific and research publications, 2013. **3**(5): p. 1-5.